AN ABSTRACT OF THE THESIS OF

Matthew W. Loewen for the degree of Master of Science in Geology presented on June 3, 2011.
Title: Analysis of Semi-Volatile Trace Metals in Basaltic Glass by LA-ICP-MS.

Abstract approved:

Adam J.R. Kent

Semi-volatile trace metals (e.g., Cd, Sn, Pb, Zn, Cu, Mo) have been analyzed by using laser ablation ICP-MS in a number of silicate glasses (GSE-1G, GSD-1G, NIST 610, NIST 612, BCR-2G, BHVO-2G). Our work investigates and highlights sources of uncertainty in the analysis of semi-volatile metals using LA-ICP-MS. We identify within-cell transport fractionation as a primary source of uncertainty in these analyses. We found no evidence for significant fractionation of elements on the basis of volatility over typical 45 second ablation intervals. However, systematic fractionation of up to 20% was found for a number of siderophile and chalcophile trace elements as well as volatile lithophile elements when comparing analyses from different locations with a simple single-volume ablation chamber. Some fractionation was also observed for analyses in GSE-1G that intersected fractures or cracks in the glass, although overall GSE-1G appears to be homogeneous with respect to semi-volatile element distributions at the ~10 % level. Calibration using GSE-1G produces more accurate results on basaltic glass compositions than NIST 610. This work thus confirms the suitability of GSE-1G as a calibration standard for analysis of semi-volatile metals in mafic composition glasses.

This thesis also reports major and trace element data for glass, olivine, and olivine-hosted melt inclusions from the 1959 eruption of Kilauea Iki, Hawaii. Major element compositions of glasses match the results of earlier studies and suggest that dominant fractionation of olivine + Cr-spinel and secondary mixing between two magma batches control compositional variations. Melt inclusions trap melts with high sulfur concentrations (~0.1-0.15 wt.%) suggestive of a melt at or near sulfide saturation, while matrix glass is highly degassed. Lithophile trace element variations more clearly illustrate

the effects of mixing at a late stage of magmatic development, and require magmas with two distinct mantle source regions and/or different degrees of partial melt. A number of non-traditional volatile trace elements were also analyzed including those with a range of volatility and geochemical affinity. Of these, most (e.g., Sn, Mo, Pb) display typical incompatible behavior while others appear to be compatible in known phases (primarily olivine: Zn, Co). Copper concentrations cannot be explained by removal of major phenocryst phases. Scatter in Cu concentrations could be achieved by either variable volatile mobility at depth or removal with a Cu-sulfide phase (either fractionated or residual). Previous studies of rare sulfides present in the 1959 eruption and more abundant sulfides crystallized in the lava lake suggest high Cu (>40 wt.%) in the sulfides. In this case even removal of a small amount of sulfide (<<1% by volume) could strongly deplete the melt of Cu while having little affect on other metals since their presence was not observed in the sulfides. There is no evidence for loss of volatile or semi-volatile trace metals during subaerial degassing.

Analysis of Semi-Volatile Trace Metals in Basaltic Glass by LA-ICP-MS

by
Matthew W. Loewen

A THESIS

submitted to

Oregon State University

in partial fulfillment of
the requirements for the
degree of

Master of Science

Presented June 3, 2011
Commencement June 2012

Master of Science thesis of Matthew W. Loewen presented on June 3, 2011.

APPROVED:

Major Professor, representing Geology

Chair of the Department of Geosciences

Dean of the Graduate School

I understand that my thesis will become part of the permanent collection of Oregon State University libraries. My signature below authorizes release of my thesis to any reader upon request.

Matthew W. Loewen, Author

ACKNOWLEDGEMENTS

I would like to thank my advisor, Adam Kent, for giving me the opportunity to pursue these projects and providing continuously insightful feedback. I also want to thank my thesis committee members John Dilles and Robert Duncan for valuable conversation and feedback throughout my work on this thesis.

Analyses performed for this project were aided with assistance from several individuals. Alison Koleszar and Andy Ungerer helped me with both instrument setup and operation in the Laser Ablation-ICP-MS lab at OSU. Allison Weinsteiger, Frank Tepley, and Dale Burns helped with calibration of the EMPA at OSU. In addition, numerous individuals including Mark Ford, Alison Koleszar, and Allison Weinsteiger helped orient me to the sample preparation facilities at OSU.

Several individuals outside of Oregon State University have generously supported this project with samples and conversation. Leslie Hale at the Smithsonian National Museum of Natural History helped me obtain an extensive sample suite of glasses from the 1959 eruption of Kilauea Iki. Rosalind Helz of the USGS generously made available a thin section with rare exposed sulfides also from this eruption. Although not presented in this thesis, samples from Loihi seamount were provided by Ken Rubin and David Clague and will be part of a future synthesis with Chapter 3 of this thesis.

Financial support of both my graduate education and analytical research in this project has been provided by National Science Foundation grants to both Adam Kent and Robert Duncan. Stipends from a Graduate Teaching Assistantship through the Department of Geosciences supported my first two years of study at OSU and provided some of my greatest learning opportunities while teaching classes including Mineralogy and Introductory Geology.

Last, my good friends in the Volcanology, Igneous Petrology, and Economic Research group (VIPER) and in the Coalition of Graduate Employees (CGE) have been involved in numerous conversations about the content of this thesis and made study at OSU truly enjoyable. My family, including Caitlin Deede, has been essential in supporting me through graduate school and I am sincerely grateful to each of them.

TABLE OF CONTENTS

LIST OF FIGURES

LIST OF FIGURES (Continued)

LIST OF TABLES

LIST OF APPENDICES

LIST OF APPENDIX FIGURES

LIST OF APPENDIX TABLES

ANALYSIS OF SEMI-VOLATILE TRACE METALS IN BASALTIC GLASS BY LA-ICP-MS

1. Introduction

Most geochemical studies in igneous petrology focus on major element oxides and common lithophile trace elements (e.g., Ba, Sr, Ce). However, many important questions in the field, require, or at least benefit from, a focus on semi-volatile elements or those with chalcophile or siderophile geochemical affinity. The behavior of these elements has implications ranging from deep mantle processes, ore deposit generation and volcanic processes in the upper crust, to environmental interactions on the surface (e.g., Sinton and Duncan, 1997; Bennett *et al*., 2000; Zajacz and Halter, 2009).

The latter of these processes spurred the original motivation of this project. Sinton and Duncan (1997) proposed that the ~90 Ma Caribbean Large Igneous Province (CLIP) could have triggered Ocean Anoxic Event 2 (OAE 2) and its associated benthic mass extinction via release of metals into the oceans. Many metals (e.g., Fe, Cu) are essential micro-nutrients in modern oceans, but also can be toxic at high concentrations. If these metals were released during the massive CLIP volcanism they could trigger a sudden increase of primary productivity if the metals are bio-limiting, resulting in ocean anoxia. This hypothesis was further supported by observations of the 1996 eruption of Loihi seamount where high concentrations of metals such as Po, Pb, Mo, W, and Sb were observed in particulate material within the water column and believed to be directly related to volcanic degassing (Rubin, 1997).

In order to investigate this and other similar hypotheses, a procedure was needed not only to analyze these metals, but also analyze them in undegassed samples from the original CLIP lavas and other basaltic eruptions. Laser Ablation-Inductively Coupled Plasma-Mass Spectrometry is an obvious candidate for these measurements. The technique allows for high spatial resolution (down to 30 μm) rapid analysis of multiple isotopes (typically 20-30). Olivine crystals, ubiquitous in basalt flows and dominant in picritic compositions occasionally found in CLIP lavas, commonly trap and enclose small bits of melt during growth in melt inclusions. Since these inclusions are trapped from the

melt during crystal growth and before eruption, they also trap melt in higher pressure conditions before significant degassing, and may preserve melt compositions in older lavas that otherwise are highly altered (e.g., Kent, 2008). Coupling LA-ICP-MS analysis with study of olivine-hosted melt inclusions could therefore be a powerful tool to investigate potential magmatic volatile behavior of many trace metals.

Analysis of trace metals by LA-ICP-MS, however, is complicated by fractionation of volatile elements during the ablation, transport, and ionization within the induction furnace of particles produced during laser ablation. These complications can lead to poor accuracy and precision for many trace metals. In addition, commonly used reference standards for LA-ICP-MS calibration (NIST-610, -612) are poor compositional matches to the basaltic compositions found in CLIP lavas and suffer from moderate heterogeneity of many trace elements of interest (Eggins and Shelley, 2002). Addressing these two issues is the primary purpose of the second chapter of this thesis. In this chapter fractionation effects (both during ablation and during particulate transport) specific to a 193 nm Ar-F Excimer laser are constrained and the primary source of analytical uncertainty identified. In addition GSE-1G and GSD-1G, synthetic glasses with a basaltic composition and doped concentrations of many trace elements, were successfully evaluated as alternative standards to the NIST series. The end result was a successful protocol to measure semi-volatile metal abundances using LA-ICP-MS, and a deeper understanding of the accuracy and sources of uncertainty in this analysis.

Melt inclusions are also challenging to both analyze and interpret. Processes such as post entrapment crystallization (PEC) and diffusive reequilibration can significantly modify their measured composition (e.g., Danyushevsky *et al*., 2000; Gaetani *et al*., 2002). In addition, degassing processes are not necessarily straightforward and may require a through understanding of all compositional controls on a system. In the third chapter of this thesis olivine-hosted melt inclusions along with matrix glasses are analyzed from the 1959 eruption of Kilauea Iki utilizing the analytical techniques developed in the Chapter 2. The system was chosen due to abundance of olivine in largely picritic rocks, evidence for substantial eruptive degassing evident in exceptionally high fire fountains, and apparently simple and well-constrained chemical evolution

dominated by olivine-control liquid lines of decent (Murata and Richter, 1966a). Correction and evaluation of PEC was completed using a novel adaptation of an olivine-melt geothermometer (Putirka *et al*., 2007) to correct inclusion glass compositions to equilibrium with host olivine. While this chapter demonstrated both effective application of LA-ICP-MS of trace metals and effectiveness of PEC corrections, it also highlighted complexities in the compositional evolution of the 1959 eruption. Mixing signatures recognized by Wright (1973) exert a much stronger influence on trace element compositions than previously thought from studies of major elements. Despite this, results show that semi-volatile metals (Cu, Zn, Pb) analyzed at concentrations > 1 ppm (analytical uncertainty is much greater at lower concentrations) are not degassed in the same manner as traditional volatile elements (e.g., sulfur) and compositional variations appear to be controlled by fractionation of mineral phases (olivine, sulfide) or crustal contamination.

2. Analysis of semi-volatile metals in silicate glass by LA-ICP-MS

Introduction

Laser ablation-inductively coupled plasma-mass spectrometry (LA-ICP-MS) has revolutionized the microanalysis of solid geologic materials over the last two decades (e.g., Fryer *et al*., 1995; Durrant, 2009; Longerich, 2008) providing the means for rapid and inexpensive quantification of trace elements with high spatial resolution (typically 30-100 μm). Although many geologic studies focus on analysis of refractory and lithophile trace elements, analysis of semi-volatile and/or chalcophile or siderophile metals has also provided important information in many areas, including contributions to the understanding of a number of important petrological processes such as core-mantle interactions in plumes (e.g., Norman *et al*., 2004; Witt-Eickschen *et al*., 2009), volcanic degassing (e.g., Rowe *et al*., 2008; Collins *et al*., 2009), magmatic differentiation (e.g., Jenner *et al*., 2010), and the transport of ore metals in magmatic systems (e.g., Zajacz and Halter, 2009).

Nonetheless, there are also limitations for LA-ICP-MS analysis of geologic materials, many of which may be more critical for study of elements of relatively high volatility. These include the level of characterization and homogeneity in the materials used for standardization together with fractionation of elements of different volatility during ablation, transport, and within the plasma furnace (e.g., Sylvester, 2008). Even though the NIST-61X series glasses (NIST-610 and NIST-612) are used widely for standardization in LA-ICP-MS studies, they are also not ideal. Eggins and Shelley (2002) demonstrated that NIST-610 and -612 are compositionally heterogeneous with respect to many chalcophile, volatile, and semi-volatile elements (depletions of Ag, As, Au, B, Bi, Cd, Cr, Cs, Mo, Pb, Re, Rh, Sb, Se, Te, Tl, and W; enrichments of Cu and Pt). The volatility of many of these elements, a property that contributes to their geologic interest, is implicated in formation of enriched and depleted zones that form during manufacture of synthetic glasses, especially near the exterior of the plugs. Other synthetic glasses may show similar features (e.g., Borisova *et al*., 2010). In addition, NIST glasses have broadly felsic (haplogranite) bulk compositions and are less suitable for analysis of basaltic

glasses and other compositions due to differing matrix effects (Outridge *et al*., 1997; Yu *et al*., 2003; Sylvester, 2008).

There is also the potential for elemental fractionation during the ablation, transport and analysis process. Although there are some differences in mass response depending on the laser wavelengths employed, UV radiation is generally absorbed more efficiently in basaltic glass compared to felsic glasses (Günther and Heinrich, 1999; Russo *et al*., 2000; Yu *et al*., 2003). This effect appears to more significantly affect analysis of elements with lower melting and boiling points (Outridge *et al*., 1997). In addition, there is the longstanding recognition that semi-volatile and chalcophile trace elements may exhibit different behavior during ablation (Eggins *et al*., 1998) and during particulate breakdown within the plasma (Günther *et al*., 1999) relative to the standard lithophile trace element suites used for many petrological investigations, and to the lithophile elements that are typically used as internal standards (Hirata and Nesbitt, 1995; Günther *et al*., 1999).

Natural composition matrix-matched standards are also of limited use for volatile metal analysis in many cases as the concentrations of trace metals in natural glasses are often too low to use for calibration, as a significant contribution in uncertainty derives from counting statistics associated with relatively low count rates. For example, both BCR-2G and BHVO-2G, which are widely used for calibration and quality control in analysis of basaltic silicate glasses and some minerals, have <1 ppm Ag, Cd, In, Sb, W, and Bi (GeoReM database[1]: Jochum *et al*., 2005). To this end, the synthetic glasses GSA-1G, GSC-1G, GSD-1G, and GSE-1G (collectively referred to here as the GS series glasses) were developed by the USGS to fulfill the need for a basaltic (~ 50 wt.% SiO_2) composition matrix-matched standard (Guillong *et al*., 2005). These glasses have sufficient levels of most trace metals (GSE-1G 120-400 ppm, GSD-1G 18-50 ppm, GeoReM database) to provide adequate calibrations for a wide range of trace metal compositions, but also may potentially suffer from the problems of heterogeneity or volatile element depletion discussed above for other synthetic glasses.

[1] http://georem.mpch-mainz.gwdg.de/start.asp

Initial studies of the GSE-1G and GSD-1G glasses suggest that they are promising materials for use as calibration standards. Although Guillong *et al*. (2005) observed large (up to 60%) variations in measured versus actual concentration when using a 266 nm Nd:YAG laser to characterize the GSA-GSE glasses, they attribute the variation to the large particle sizes produced with the longer wavelength laser radiation and the use of non matrix-matched calibration standards (NIST glasses). This effect can be mitigated with the use of shorter wavelength laser radiation, and Guillong *et al*. (2003) showed that a 193 nm laser wavelength effectively reduces the effects from preferential fractionation. The shorter wavelength produces a smaller average and fewer maximum sized (>150 nm diameter) particles resulting in more consistent ionization and less sample loss during transport.

Another key aspect of standard performance is homogeneity. Guillong *et al*. (2005) did not directly characterize homogeneity and only concluded from relative standard deviations of single analyses that the glasses were generally homogeneous (RSD<15%) except for Cd, Tl, and Se. Given the problems highlighted in maintaining homogeneous distributions of semi-volatile and other metals during glass production (Eggins and Shelley, 2002; Borisova *et al*., 2010), we believe that this should be directly evaluated.

In this contribution we explore the homogeneity of GSE-1G and GSD-1G glasses, focusing on semi-volatile metals (see Fig. 1.1). We also highlight the role of ablation chamber performance on precision and accuracy during analysis of semi-volatile metals and explore the effectiveness of NIST-610 and GSE-1G as calibration standards for the analysis of semi-volatile metals in basaltic silicate glasses.

Analytical Methods

Laser Protocol

We made analyses using a NewWave DUV 193 nm ArF Excimer laser system (see Table 1.1 for details). Both 80 and 50 μm spot sizes were used for transects of samples of GSD-1G and GSE-1G and for analyses of BHVO-2G, BCR-2G, NIST-612, and GSD-1G using both NIST-610 and GSE-1G as calibration standards. Between 30 and

43 masses were measured in each test including elements with a wide range of geochemical affinities (lithophile, chalcophile, and siderophile) along with volatile and semi-volatile elements (based on condensation temperatures from Lodders, 2003; Fig. 1.1).

We processed data using in-house LaserTRAM software using Visual Basic running within Microsoft Excel. This software was used to select a 20-30 second background interval and a ~30 second ablation interval for each analysis. The software corrects for background and normalizes the count rates for each element over the ablation interval to the selected internal standard (^{43}Ca or ^{29}Si in this case). The software subdivides the selected ablation interval into a preselected number (typically 3-5) of subintervals of equal duration and background-corrected counts recorded in each of these were binned before calculating normalized ratios for each subinterval. In materials that are homogenous at the scale of an individual analysis crater this approach reduces error magnification related to low count rates and short dwell times. Final normalized ratios for each sample are the median value of the normalized ratios calculated for each subinterval (we use the median as it is more robust with respect to outliers than the mean). Uncertainties in each normalized ratio are determined as 2 standard error (2 se) of the combined results for each subinterval. Normalized ratios were used to calculate concentrations using the CaO or SiO_2 value for each material and literature values for the calibration standard (Jochum *et al*., 2005).

Analyses we report herein include a number of spot analyses of different glass materials as well as multi-point transects across individual mm-sized chips of GSE-1G and GSD-1G glass (Fig. 1.2). These consist of lines of spots rather than continuous rastered traverses. In some cases transects were repeated in multiple analysis sessions to look at long-term accuracy and precision. Transects were also analyzed with sample mounts in different locations within the ablation chamber to study cell transport effects. To simplify comparisons, our data are primarily presented as normalized values for each isotope instead of calibrated concentrations. Although this approach does not automatically correct for short-term instrumental drift, comparison of secondary standard glass analyses before and after the analysis of GSE-1G and GSD-1G were used to

monitor significant changes and none were observed. Transect experiments were conducted over a number of instrument days in which slight variations in instrument tuning resulted in differing mass sensitivities, and therefore [X]/[^{43}Ca] ratios on different days. In order to compare overlapping transects directly, ratios are reported as percent deviance from the median over each individual transect. This normalization to the median of each transect also served to correct transects for any additional variations related to position within the chamber.

With a few exceptions, we found little evidence for significant isobaric interferences for the elements and matrices analyzed in this study. Almost all elements that have multiple isotopes available for measurement show similar accuracies for each isotope and no consistent variations in concentrations calculated from different isotopes (Mg, Cr, Cu, Zn, Mo, Ag, Cd, Sn, Sb, W, Re). Exceptions may exist for Se where ^{76}Se and ^{82}Se both consistently returned values significantly greater than reported values for standards and had unusually large uncertainties calculated for each individual spot analysis (>10%). These isotopes both suffer from significant Ar- and Kr-based interferences, although these potentially can be largely controlled by the gas blank subtraction. In addition Se may also suffer for relatively poor levels of characterization in many materials. Concentrations calculated with ^{115}In are typically 20% lower than with ^{113}In and are consistently closer to preferred values, suggesting interference may affect the latter isotope.

To assess the role of laser-induced fractionation, fractionation factors (e.g., Freyer *et al*., 1995; Mank and Mason, 1999; Sylvester, 2008) were measured with 80 μm spot sizes over longer ablation intervals (120 seconds with a pulse rate of 4 Hz) for GSE-1G, GSD-1G, NIST-610, and NIST-612 glasses. For these calculations the median counts from the first and last 30 seconds of stable ablation were selected. The fractionation index was then calculated from the ratio of counts in the second to counts in the first half of the ablation period (after Fryer *et al*., 1995; Mank and Mason, 1999). As with transect analyses, all fractionation values were calculated from raw data normalized to ^{43}Ca counts and result in fractionation values relative to Ca = 1.

A schematic of the ablation chamber used for this study is shown in Fig. 1.3. For routine analyses samples set in 25 mm diameter epoxy mounts are located in a central position with smaller (~12 mm) mounts used for standards located on either side. Helium enters and is extracted from the chamber at points located along the axis of the three sample/standard mount locations.

Electron Microprobe Analysis (EMPA)

Major elements (Si, Al, P, K, Ca, Mn, Fe, Na, Mg, Ti) in GSE-1G and GSD-1G were measured using a Cameca SX-100 Electron Microprobe Analyzer at Oregon State University. A focused 5 μm beam with a 15 keV accelerating voltage and 30 nA beam current was used with variable peak count times: 10 s for Si, Al, and Fe; 20 s for Na and Ti; 30 s for K, Ca, and Mn; and 60 s for P and Mg. Makaopuhi Lava Lake basaltic glass (USNM 113498/1 VG-A99) was analyzed after calibration to monitor for accuracy and stability. Elements used as internal standards (Si and Ca) are accurate to 3% in analyses of secondary standards and are reproducible at <2% 2 sd.

Results and Discussion

Element Fractionation during LA-ICP-MS analysis

Elemental fractionation is a common occurrence during laser ablation ICP-MS analysis, particularly when comparing elements with markedly different volatilities (Hirata and Nesbitt, 1995; Sylvester, 2008). Studies that have investigated this phenomenon have emphasized the role of fractionation induced during progressive ablation due to changes in local condensation regime and laser-induced plasma extraction as the ablated crater becomes deeper (e.g., Eggins et al., 1998; Mank and Mason, 1999). This phenomenon is typically referred to as laser-induced fractionation. Other workers have focused on the role of transport of the particulate material produced by ablation and the elemental fractionation produced by incomplete breakdown of larger particles within the ICP-MS plasma furnace (Outridge *et al*., 1997; Guillong *et al*., 2003). Finally there is also the potential effect of differential sweep gas flow and the corresponding efficiency of condensation and particulate transport within the ablation cell. Modern two-volume

cell designs minimize differential particulate transport (e.g. Eggins and Shelley, 2002; Müller *et al*., 2009) but many ablation systems currently in use, including that on the instrument used in this study, have a single-volume design that may have significant variations in sweep gas velocity and flow mode within the cell (Bleiner and Bogaerts, 2007). As we describe below, these variations may translate to significant fractionation of volatile and other trace elements during ablation.

In the following sections we discuss the possible origins of elemental fractionation during laser ablation analysis, focusing on analysis of volatile and semi-volatile metals. After that we discuss the homogeneity of GSE-1G and GSD-1G glasses and their usefulness as standards for volatile and semi-volatile metal analysis. Finally we discuss the overall controls on precision and accuracy in analysis of these elements using LA-ICP-MS.

Laser-induced Fractionation

In order to gauge the level of laser-induced fractionation, fractionation factors for progressive deepening of the ablation pit were measured using the protocol described above (Fig. 1.4). Previous studies (Fryer *et al*., 1995; Eggins et al., 1998; Mank and Mason, 1999; Jackson, 2001; Jackson, 2008; Hu *et al*., 2011) have shown that in some instances significant fractionation of elements of different volatility may occur during extended ablation and production of deep ablation craters. For this study we determined fractionation factors for GSD-1G, GSE-1G, NIST-612, and NIST-610 glasses. To minimize the effects of sample chamber location we report only fractionation factors from the center mount position (see below and Fig 1.3). Estimates of crater depth using transmitted light microscopy show that transparent glasses ablated to greater depths than opaque glasses over the 120 second ablation interval: NIST-610 glass ablated at 4 Hz to 86 ± 2 μm, NIST-612 ablated to 79 ± 2 μm (~ 170 nm per pulse) whereas the relatively opaque GSE-1G and GSD-1G glasses both ablated to 60 ± 2 μm (~125 nm per pulse).

Overall we see little evidence for significant fractionation of elements based on volatility or other properties during progressive ablation of a single crater (Fig. 1.4). Fractionation factors in all cases are typically low (0.9-1.1) compared to values reported

elsewhere (up to three using 266 and 248 nm wavelength ablation systems and longer ablation times: Fryer *et al*., 1995; Mank and Mason, 1999). In addition our data show no consistent relation between volatility or geochemical affinity and fractionation factor. Our low fractionation factors are broadly consistent with previous work that suggests that laser-induced elemental fractionation is less important when using the shorter wavelength ArF lasers and in shorter (up to 40 second) ablation intervals and larger spot sizes (>44 μm; Günther and Heinrich, 1999; Kent and Ungerer, 2005; Hu *et al*., 2011). In addition, ablation craters produced by the 120 second ablation intervals reported have aspect ratios close to one, much less than the six or greater aspect ratio found by Mank and Mason (1999) needed to produce significant volatile fractionation.

Our data suggest that fractionation of elements on the basis of volatility, related to either differences in condensation and laser-induced plasma extraction from a deepening crater (e.g. Eggins et al. 1998; Mank and Mason, 1999) is negligible with the instrumental setup and analysis protocol detailed herein. For this reason, and because our typical analysis protocol for unknown materials uses only 45 seconds of ablation (producing 20-30 μm deep craters), we believe that laser-induced elemental fractionation during ablation is likely insignificant (<10%) for the purposes of measurements of elemental composition, even where large differences are apparent in the volatility of the analyte and internal standard element. Comparison of the signal intensity from the first half of this shorter ablation period to the second confirms that again little apparent (< 10%) fractionation occurs during these shorter ablations.

Fractionation Induced within the Ablation Chamber

Although we see little evidence that laser-induced elemental fractionation is significant for analysis of volatile and semi-volatile metals using our analysis protocol, our initial results did show evidence for variations in degree of volatile/refractory fractionation depending on position within the ablation cell. We conducted a series of experiments designed to study this further by systematically varying the analysis location of GSE-1G glass by rotating a mount containing three different chips of glass by 90° between analyses.

Three distinct sets of behavior were observed between the three chips dependent on their position in the sample chamber (Fig. 1.5). When all three chips were aligned in a direction parallel to the He flow direction (Positions 2 and 4 in Fig. 1.5), the ratios of elements to ^{43}Ca determined from multiple analyses of each chip were broadly similar and largely within uncertainty of each other. However, when the sample mount is aligned so that only a single glass chip is positioned along the axis of the sample cell (Positions 1, 3) then a number of volatile and/or chalcophile elements (in order of increasing depletion: Pb, Cd, Sb, Cr, Ag, Bi, Li, Co, Zn, Te, Rb, Si, W, In, As, Sn, Mo, V, B, Re, Cu, Ir, Au) have distinctly lower X/^{43}Ca ratios (10-15% on average) in the two glass chips that sit at the top and bottom locations relative to the chip located in the center (Fig. 1.5 and 1.6). Conversely, in these positions some refractory elements (e.g., Sc, Zr, Y) show enrichments (10-22%) relative to those measured in the two adjoining glass chips, although other refractory elements (e.g., Ti, Ba, Sr) show no consistent offset. The magnitude of these variations varies from as little as -35% to +15% and is most depleted for highly volatile and/or non-lithophile elements (Fig. 1.6). This effect is also highly reproducible (e.g., Fig 1.5).

By comparing the relative position of chips and their Ca normalized ratios, it is clear that a zone of relative depletion of more volatile or sidero/chalcophile elements and relative enrichment in some refractory elements exists across the center of the sample chamber (Fig. 1.5 and 1.6). This zone is aligned with the He input and output orifices. While the sample chamber moves in relation to the laser for different analyses, the sample does not change its position relative to the He carrier gas intake and outtake from the ablation chamber (Fig. 1.3). The pattern of enrichment is moderately systematic with volatility (based on condensation temperature) for most lithophile elements. The most volatile lithophile elements (Rb, B) along with chalcophile (e.g., Cu, Pb) and siderophile (e.g., Mo, W) elements all have depletions within a restricted range between 10-15%.

Although the detailed mechanism by which the elemental fractionation that we observe is beyond the scope of this paper, we can make some important observations. Given the clear relation of element enrichment/depletion relative to Ca and location within the sample chamber, we believe that the variations observed in the elemental

response are likely related to differential He carrier gas flow rates through the ablation chamber. The location of the He intake and outtake orifices along the axis of the sample chamber suggests that there is a region of distinctly faster He flow along the center of the ablation cell (Fig. 1.3). Computational modeling (Bleiner and Günther, 2001; Bleiner and Bogaerts, 2007; Bleiner and Chen, 2008) of gas flow within drum-shaped ablation chambers that are similar in geometry to that which we have used in our experiments confirms that this geometry produces a narrow zone of high velocity flow along the center of the chamber. This zone closely corresponds to the region in which we observe the significant elemental enrichment and depletion (Fig. 1.3 and 1.5). In contrast, along the top and bottom of the sample chamber, He velocities are slower and locally may even flow back towards the He intake (Bleiner and Bogaerts, 2007).

The exact mechanism by which elemental fractionation occurs in this instance is unclear, but unlikely to relate solely to fractionation during ablation or within the plasma furnace. Our results shown above (e.g., Fig 1.4) demonstrate that laser-induced fractionation appears to be minimal with the analytical protocol used herein. Likewise, the fractionation we observe is unlikely to be related to increased transport of larger ablated particulates to the plasma furnace at high He flow rates as: (1) incomplete ionization of larger particulate in the plasma furnace will preferentially increase the response of more volatile elements (Jackson, 2008), the reverse of what we observe when ablation occurs in the high He velocity portion of the ablation cell (Fig. 1.5), and (2) particles produced by ablation at the 193 nm wavelength we utilize are dominated by small sizes (< 150 nm; Guillong *et al*., 2003) and contain relatively minor contributions from the problematic larger particles that may experience incomplete breakdown.

We suggest that the fractionation we observe instead relates to variations in condensation and transport when a portion of the laser-induced plasma above the sample collapses back onto the sample surface. During this process more refractory elements may condense first, forming refractory particulates that enter the He stream preferentially due their higher intrinsic momentum (Eggins et al., 1998). In contrast more volatile species will remain within the vapor plume that is driven back to the surface in the high pressure expansion front of the plasma. Volatile elements will then be preferentially

concentrated in the material deposited back onto the sample surface around the ablation crater (Eggins et al., 1998). In theory differential condensation and transport at this point thus provides a mechanism to fractionate refractory from volatile elements. Our results suggest that this process occurs preferentially at locations with higher He velocities within the ablation chamber, where high momentum (and refractory-enriched) particulates preferentially escape the surface after ablation. Alternatively, refractory elements may be preferentially incorporated into small particulates produced by ablation while volatile elements are present more in the plasma (Outridge *et al*, 1997). In the low He velocity zones, these particulates are more easily deposited back onto the sample surface resulting in a relative depletion of refractory elements and enrichment of volatile elements.

The fractionation we observe here emphasizes the importance of sample cell geometry and He flow regime in controlling precision and accuracy of volatile and/or siderophile-chalcophile elemental analysis during LA-ICP-MS analysis. As it may be difficult and inefficient to control the analysis location within the sample cell (particularly for natural samples where analysis locations are typically distributed throughout a specific matrix) differential fractionation within the ablation chamber represents a key limit on the accuracy of any element that behaves unlike the internal standard (typically Ca) and may introduce a systematic bias from samples located away from the calibration standard. For more volatile elements, there is potential to use Si as an alternate internal standard, however in most geologic glasses, no viable alternative internal standard exists for more refractory elements. Also, for analysis of some mineral and glass matrices that are low in Ca, no viable alternative to Si can be used for internal standardization resulting in increased uncertainties for typical lithophile elements. Modern two-volume cell designs (Müller *et al*., 2009) may effectively minimize the within-cell fractionations we observe by maintaining consistent He flow regimes in all portions of the sample chamber. Nonetheless, many existing systems have similar ablation cell geometries to the cell used herein. This work highlights the need to be aware of this effect as a limitation to any volatile element analysis, and our approach provides a simple methodology for investigating this effect for different ablation systems.

Homogeneity of GSE and GSD glasses

Our data also provide the means to assess the homogeneity of GSE-1G and GSD-1G glasses and test their utility as standards for analysis of volatile and semi-volatile metals in silicate glasses. We have analyzed a total of eight transects (consisting of between 9 and 30 individual spots per transect, 164 total, placed 150-200 μm apart) on four different chips of GSE-1G glass and two transects on one chip (consisting of 15 individual spots per transect, 30 in total, placed ~300 μm apart) of GSD-1G glass (Fig. 1.2). Of these results all transects in GSD-1G and all but two in GSE-1G show no indication of spatially correlated variations in composition. For these transects the normalized ratios for each isotope measured typically varied by < ±10% at 2 standard deviations (sd; Table 1.2). One chip of GSE-1G does show some apparent variation (Fig. 1.7) and we discuss this further in detail below. Major element results by EMPA on all three chips of GSE-1G and the single chip of GSD-1G were also within uncertainty of literature values (Table 1.3) and showed no systematic compositional variation between each chip or along transects.

As noted, one piece of GSE-1G glass appeared to be heterogeneous with some systematic apparent deviations of normalized element ratios. The locations and results of the 30 spot transect on GSE-1G are reported in Fig. 1.2 and 1.7. These two traverses either end adjacent to a fracture (horizontal traverse) or follow a small hairline fracture for several millimeters (vertical traverse). Examination of the data reveal four distinct trends in the normalized ratios measured: (1) elements that appear to be homogeneous in both transects with respect to Ca (only Ti), (2), elements depleted at the beginning of the vertical transect (Sc), elements with strong (>10% higher than the median value of both transects: Si, V, Co, Cu, Zn, Se, Sn, Sb, W, Pb, Bi) to minor (Mg, Mn, Fe) enrichments compared to Ca at the start of the vertical transect, and (3) elements with a notable depletion at the end of the horizontal transect as well as enrichment at the start of the vertical transect (B, Cr, As, Mo, Ag, Cd, Te, Re, Tl). These results are not a product of instrumental drift or differential He flow within the ablation cell as they have been

duplicated on multiple analysis sessions with the analyzed mount in different orientations within the sample holder.

Instead, these observed heterogeneities in the GSE-1G glass appear to be related to ablation near defects in the glass (e.g., cracks, thin edges) and are directly related to element volatility and/or geochemical affinity. This is evident when values are examined normalized to a more volatile internal standard, Si (Fig. 1.7). Si and Ca have nearly opposite ablation patterns in these anomalous zones. Use of Si as an internal standard accentuates deviations in highly refractory lithophile elements (Sc) while nearly eliminating anomalies for moderately volatile elements (Fe, Cu, Mo). Anomalies for elements with higher volatility (e.g., Cd) are only slightly moderated with Si normalization. Since independent analysis along the transects by EMPA shows no real variations in Si or Ca, we conclude that all variations are due to fractionation during laser ablation and do not reflect heterogeneity in the glasses themselves.

Although the origin of this elemental fractionation is not completely clear we note that Mank and Mason (1999) proposed that cracks observed near the surface of long ablations increased surface area and subsequently increased the loss of more highly volatile elements from the sample. This or similar process could potentially also explain increases we observe in volatile elements (with respect to Ca) at the start of the vertical transect due to interaction of the laser with the hairline fracture, as shown in Fig. 1.2, and might also explain the extreme depletion seen in some volatile elements along the end of the horizontal transect where ablation intersected a large open crack. In detail, the mechanism of fractionation remains unclear in this case, but the results do suggest care should be taken to select analysis spots clear of any large fractures or openings in the sample surface, especially for elements with relatively high volatilities.

With the exception of these anomalous results, when we combine results from all transects, we conclude that both GSE-1G and GSD-1G are generally homogenous within the analytical uncertainty of our instrumental setup (<~10% variation at 2 sd). In addition to the lack of observed spatially-correlated variations in these glasses, both the internal error (2 se for each individual spot analysis) and overall variation (2 sd of all transect points, normalized to the median of the transect) form clear linear trends on log-log plots

of relative error vs. concentration, as would be expected where uncertainty is controlled by counting statistics rather than heterogeneity (Fig. 1.8). Only when the anomalous analyses located near fractures in the glasses are included does the overall variation trend contain more scatter. Interestingly, internal error is not different in analyses near cracks or fractures. This observation is important to note as the errors associated with ablation on or near defects in the glass will not be readily apparent while processing data.

Controls on Precision and Accuracy

In this section we consider the overall controls on precision and accuracy during LA-ICP-MS analysis of silicate glasses, focusing on analysis of semi-volatile and volatile metals. On average, the uncertainty of elemental concentrations calculated over the course of an ablation from each spot analyses in GSE-1G and GSD-1G were low (<~5% at 2 se). Only Se, Au, Tl, and Ir have uncertainties >10% at 2 se, and first three of these elements have relatively low concentrations in both of the standard glasses (20, 7, and 2 ppm respectively in GSE-1G; 2, 4, and 0.9 ppm in GSD-1G; GeoReM database). Both the average internal errors (calculated for each spot analysis) and the overall variation calculated from repeated analyses correlate linearly with concentration (Fig. 1.8).

In general, it appears that the largest contribution to uncertainty in these analyses, in addition to uncertainties related to counting statistics, is that from the variations in elemental fractionation within the ablation cell discussed above (Fig. 1.5 and 1.6, Table 2). In order to estimate the overall uncertainty due to this effect we have grouped our normalized ratios measured in GSE-1G. Our results show 10-20% (Table 1.2) variations at 2 sd for most elements by comparing analyses made on three GSE-1G chips located across the chamber without normalizing to the median of each transect. This uncertainty is consistent with the magnitude of fractionation observed between the center and top or bottom of the sample chamber (Fig. 1.5, 1.6). During the routine analysis of unknowns location with the ablation chamber is rarely well controlled we consider that these uncertainties provide the best estimate of the long-term accuracy and precision of volatile and semi-volatile metal analyses.

Finally we have also investigated the accuracy of our analysis protocol using GSE-1G and NIST-610 as calibration standards for analysis of synthetic and natural composition basaltic glasses (GSD-1G, BCR-2G, BHVO-2G) at two different spot sizes (Table 1.4, Fig. 1.9). Results show excellent accuracy (better than or equal to ±10%) for analysis of GSD-1G in both the 50 and 80 μm spot using GSE-1G as a calibration standard (Fig. 1.9A). Only Cr, Cd, and In had accuracies greater than ±10%. Accuracies of natural glasses (for BHVO-2G and BCR-2G) were generally worse, though this can be attributed to natural concentrations being lower (<10 ppm: B, Mn, As, Se, Ag, Cd, In, Sn, Sb, W, Re, Au, and Bi in BHVO-2G; B, Ni, Cu, As, Se, Ag, Cd, In, Sn, Sb, Sb Bi, and Tl in BCR-2G). Some elements (Mn and Zn), however, had higher concentrations (100-400 ppm) and still returned relatively poor accuracy (worse than ±20% deviation from accepted values). Most elements that are well characterized and/or present at reasonable concentrations, however, returned excellent accuracies (less than ±10%). In all this suggests that GSE-1G is a suitable calibration standard for semi-volatile and volatile metals in natural basaltic compositions.

Accuracies determined for GSD-1G using NIST-610 as a calibration standard were considerably worse (Fig. 1.9A), typically ranging between 15 and 30% away from accepted concentrations. In general, accuracies improved by ~10% when using GSE-1G as a standard. It is interesting to note that even accuracy of NIST-612 analysis were on average better using GSE-1G as a calibration standard than NIST-610, although the difference is not as dramatic as for basaltic composition glasses (Fig. 1.9B). As with the GSE-1G calibration, natural basaltic glasses returned poorer accuracies, but this mostly is attributed to low concentrations of many elements. Accuracy was also worse for both BCR-2G and BHVO-2G when using NIST-610 as the calibration standard.

Conclusions

1) GSE-1G and GSD-1G glass appear to be compositionally homogeneous within instrumental precision for both major and volatile trace elements.

2) Matrix-matched calibration standards result in better accuracies for calibration of basaltic glass. GSE-1G is a superior calibration standard for basaltic composition glasses than the commonly used NIST series.
3) Uncertainties in each spot analysis are generally low (<5-10%) while using a 193 nm Ar-F laser. Fractionation is minimal, especially over typical 45 second ablation intervals.
4) The majority of uncertainties result from fractionation of elements within the ablation chamber. High He carrier gas velocities in the center of the chamber preferentially samples more refractory elements while low velocity zones in the top and bottom of the chamber preferentially sample volatile elements. Almost all error associated with volatile elements in our single-volume sample chamber can likely be attributed to this affect.
5) Anomalous fractionation may be associated with fractures or cracks in glass.

While we did not find the heterogeneities observed by Eggins and Shelley (2002) in NIST glasses in the GS glass series, it is important to note that in their analysis of NIST only limited heterogeneities were observed with spot transects, and considerably more variation was observed with detailed rastering and optical analysis. Zones of volatile element depletions and enrichments may be more obvious with small-scale observations. Many studies, however, have still reported low uncertainties while using NIST as a calibration standard (e.g. Collins *et al*., 2009; Witt-Eickschen *et al*., 2009) suggesting that the small-scale heterogeneities in NIST glasses are not likely to severely offset calibrations and precision. It may be that, despite heterogeneities, the odds of hitting such zones are low and by making multiple calibration analyses, any anomalous measurements can be excluded, though accuracies may be offset due to differences from bulk analysis of the standard glass. Our results suggest that as long as defects within the standard glass are avoided, the GSD and GSE standard glasses are at least as homogeneous as NIST glasses.

Substantial variations of volatile elements in different locations within our sample chamber, however, present more of a challenge. Normalizing to Si may offset this

fractionation for highly volatile elements, but increased uncertainty in Si reported both by EMP and by ICP-MS will create greater uncertainty. Si normalization will also not correct for more refractory elements. Newer model two-volume sample cells may provide a means to reduce or eliminate this uncertainty.

References

Bleiner, D., and Bogaerts, A., 2007, Computer simulations of sample chambers for laser ablation-inductively coupled plasma spectrometry, Spectrochimica Acta Part B: Atomic Spectroscopy, v. 62, p. 155-168.

Bleiner, D., and Chen, Z., 2008, Computer Modeling of Laser Ablation Elemental Microanalysis, Mineralogical Association of Canada Short Course, v. 40, p. 35-52.

Bleiner, D., and Gunther, D., 2001, Theoretical description and experimental observation of aerosol transport processes in laser ablation inductively coupled plasma mass spectrometry, Journal of Analytical Atomic Spectrometry, v. 16, p. 449-456

Borisova, A.Y., Freydier, R., Polve, M., Jochum, K.P., Candaudap, F., 2010, Multi-Elemental Analysis of ATHO-G Rhyolitic Glass (MPI-DING Reference Material) by Femtosecond and Nanosecond LA-ICP-MS: Evidence for Signifcant Heterogeneity of B, V, Zn, Mo, Sn, Sb, Cs, W, Pt and Pb at the Millimetre Scale, Geostandards and Geoanalytical Research, v. 34, p. 245-255.

Collins, S. J., Pyle, D. M., and Maclennan, J., 2009, Melt inclusions track pre-eruption storage and dehydration of magmas at Etna, Geology, v. 37, p. 571-574.

Durrant, S.F., 1999, Laser ablation inductively coupled plasma mass spectrometry: achievements, problems, prospects, Journal of Analytical Atomic Spectrometry, v.,14, p. 1385-1403.

Eggins, S., and Shelley, J.M.G., 2002, Compositional heterogeneity in NIST SRM 610-617 glasses, Geostandards Newsletter: The Journal of Geostandards and Geoanalytical Research, v. 26, p. 269-286.

Eggins, S., Kinsley, L., and Shelley, J., 1998, Deposition and element fractionation processes during atmospheric pressure laser sampling for analysis by ICP-MS, Applied Surface Science, v. 127, p. 278-286.

Fryer, B., Jackson, S.E., and Longerich, H., 1995, The design, operation and role of the laser-ablation microprobe coupled with an inductively coupled plasma; mass spectrometer (LAM-ICP-MS) in the earth sciences, Canadian Mineralogist, v. 33, p. 303-312.

Guillong, M., Hametner, K., Reusser, E., Wilson, S.A., and Gunther, D., 2005, Preliminary Characterization of New Glass Reference Materials (GSA-1G, GSC-1G, GSD-1G, GSE-1G) by Laser Ablation-Inductively Coupled Plasma-Mass

Spectrometry Using 193 nm, 213 nm and 266 nm Wavelengths, Geostandards and Geoanalytical Research, v. 26, p. 315-331.

Guillong, M., Horn, I., and Gunther, D., 2003, A comparison of 266 nm, 213 nm and 193 nm produced from a single solid state Nd:YAG laser for laser ablation ICP-MS, Journal of Analytical Atomic Spectrometry, v. 18, no. 10, p. 1224-1230.

Günther, D., and Heinrich, C.A., 1999, Comparison of the ablation behaviour of 266 nm Nd: YAG and 193 nm ArF excimer lasers for LA-ICP-MS analysis, Journal of Analytical Atomic Spectrometry, v. 14, p. 1369-1374.

Günther, D., Jackson, S.E., and Longerich, H., 1999, Laser ablation and arc/spark solid sample introduction into inductively coupled plasma mass spectrometers, Spectrochimica Acta Part B: Atomic Spectroscopy, v. 54, p. 381-409.

Hirata, T., and Nesbitt, R., 1995, U-Pb isotope geochronology of zircon: evaluation of the laser probe-inductively coupled plasma mass spectrometry technique, Geochimica et Cosmochimica Acta, v. 59, p. 2491-2500.

Hu, Z., Liu, Y., Chen, L., Zhou, L., Li, M., Zong, K., Zhu, L., and Gao, S., 2011, Contrasting matrix induced elemental fractionation in NIST SRM and rock glasses during laser ablation ICP-MS analysis at high spatial resolution, Journal of Analytical Atomic Spectrometry, v. 26, p. 425-430.

Jackson, S.E., 2001, The Application of Nd:YAG Lasers in LA-ICP-MS, in Laser-ablation-ICPMS in the earth sciences: Principles and applications, p. 29-45.

Jackson, S.E., 2008, Calibration Strategies for Elemental Analysis by LA-ICP-MS, Mineralogical Association of Canada Short Course, v. 40, p. 169-188.

Jenner, F.E., O'neill, H.S.C., Arculus, R.J., and Mavrogenes, J.A., 2010, The Magnetite Crisis in the Evolution of Arc-related Magmas and the Initial Concentration of Au, Ag and Cu, Journal of Petrology, v. 51, p. 2445-2464.

Jochum, K., Nohl, U., Herwig, K., Lammel, E., Stoll, B., and Hofmann, A., 2005, GeoReM: A new geochemical database for reference materials and isotopic standards, Geostandards and Geoanalytical Research, v. 29, p. 333-338.

Kent, A.J.R., and Ungerer, C., 2006, Analysis of light lithophile elements (Li, Be, B) by laser ablation ICP-MS: Comparison between magnetic sector and quadrupole ICP-MS, American Mineralogist, v. 91, p. 1401-1411.

Kent, A.J.R., and Ungerer, C.A.A., 2005, Production of barium and light rare earth element oxides during LA-ICP-MS microanalysis, Journal of Analytical Atomic Spectrometry, v. 20, p. 1256-1262.

Lodders, K., 2003, Solar system abundances and condensation temperatures of the elements, The Astrophysical Journal, v. 591, p. 1220-1247.

Longerich, H., 2008, Laser Ablation-Inductively Coupled Plasma- Mass Spectrometry (LA-ICP-MS): An Introduction, Mineralogical Association of Canada Short Course, v. 40, p. 1-18.

Longerich, H., Jackson, S.E., and Günther, D., 1996, Laser ablation inductively coupled plasma mass spectrometric transient signal data acquisition and analyte concentration calculation, Journal of Analytical Atomic Spectrometry, v. 11, p. 899-904.

Mank, A., and Mason, P., 1999, A critical assessment of laser ablation ICP-MS as an analytical tool for depth analysis in silica-based glass samples, Journal of Analytical Atomic Spectrometry, v. 14, p. 1143-1153.

Müller, W., Shelley, M., Miller, P., and Broude, S., 2009, Initial performance metrics of a new custom-designed ArF excimer LA-ICPMS system coupled to a two-volume laser-ablation cell, Journal of Analytical Atomic Spectrometry, v. 24, p. 209-214.

Norman, M.D., Garcia, M.O., and Bennett, V.C., 2004, Rhenium and chalcophile elements in basaltic glasses from Ko'olau and Moloka'i volcanoes: Magmatic outgassing and composition of the Hawaiian plume, Geochimica et Cosmochimica Acta, v. 68, p. 3761-3777.

Outridge, P., Doherty, W., and Gregoire, D., 1997, Ablative and transport fractionation of trace elements during laser sampling of glass and copper, Spectrochimica Acta Part B: Atomic Spectroscopy, v. 52, p. 2093-2102.

Rowe, M.C., Kent, A.J.R, and Thornber, C.R., 2008, Using amphibole phenocrysts to track vapor transfer during magma crystallization and transport: An example from Mount St. Helens, Washington, Journal of Volcanology and Geothermal Research, v. 178, p. 593-607.

Russo, R., Mao, X., Borisov, O., and Liu, H., 2000, Influence of wavelength on fractionation in laser ablation ICP-MS, Journal of Analytical Atomic Spectrometry, v. 15, p. 1115-1120.

Sylvester, P. J., 2008, Matrix Effects in Laser Ablation-ICP-MS, Mineralogical Association of Canada Short Course, v. 40, p. 67-78.

Witt-Eickschen, G., Palme, H., O'Neill, H.S.C., and Allen, C.M., 2009, The geochemistry of the volatile trace elements As, Cd, Ga, In and Sn in the Earth's mantle: New evidence from in situ analyses of mantle xenoliths, Geochimica et Cosmochimica Acta, v. 73, p. 1755-1778.

Yu, Z., Norman, M.D., and Robinson, P., 2003, Major and trace element analysis of silicate rocks by XRF and laser ablation ICP-MS using lithium borate fused glasses: Matrix effects, instrument response and results for international reference materials, Geostandards Newsletter: The Journal of Geostandards and Geoanalytical Research, v. 27, p. 67-89.

Zajacz, Z., and Halter, W., 2009, Copper transport by high temperature, sulfur-rich magmatic vapor: Evidence from silicate melt and vapor inclusions in a basaltic andesite from the Villarrica volcano (Chile), Earth and Planetary Science Letters, v. 282, p. 115-121.

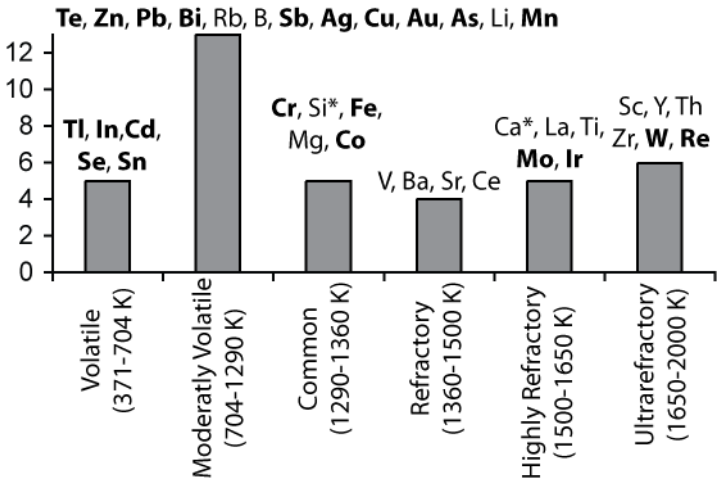

Figure 1.1. Elements analyzed in LA-ICP-MS experiments. These include a wide range of volatility (50% condensation temperature from a solar nebula composition, after Lodders, 2003) and geochemical affinities (bold elements are siderophile or chalcophile). Moderately volatile elements were emphasized in order to characterize their potential for fractionation behavior in LA-ICP-MS. *denotes elements used as internal standards.

Table 1.1. LA-ICP-MS instrument setup.

Parameter	Description
Instrumentation	
Laser Ablation System	VG ExCell NewWave DUV 193 ArF Excimer Laser
ICP-MS System	VG PQ ExCell Quadrupole
Laser Conditions	
Wavelength	193 nm
Frequency	4-5 Hz*
Pulse Duration	15 ns
Spot Diameter	50, 80, 100, and 160 μm
Ablation Duration	45 seconds (up to 120 seconds for fractionation tests)
Output Energy	180-210 mJ at 193 nm (~15 J/cm^2)
Analyzer Conditions	
Aerosol carrier gas flow	0.8 l/min (He)
Nebulizer gas flow	0.80-0.95 l/min (Ar)
Outer (cool) gas flow	13.00 l/min (Ar)
Detector mode	Dual (pulse counting and analogue)
RF power	1300 W
Vacuum Pressure	8-10 x 10-7 mbar (analyzer), 1.5-1.9 mbar (expansion chamber)
Mass Table	variable, see Table 2.
Dwell time/mass/scan	10 ms
Total scan time	~300 ms
Standardization	
Internal Standard	^{43}Ca, ^{29}Si
Calibration Standards	GSE-1G, GSD-1G, NIST-610, NIST-612

* 5 Hz used in homogeneity transects, 4 Hz used in accuracy and fractionation tests

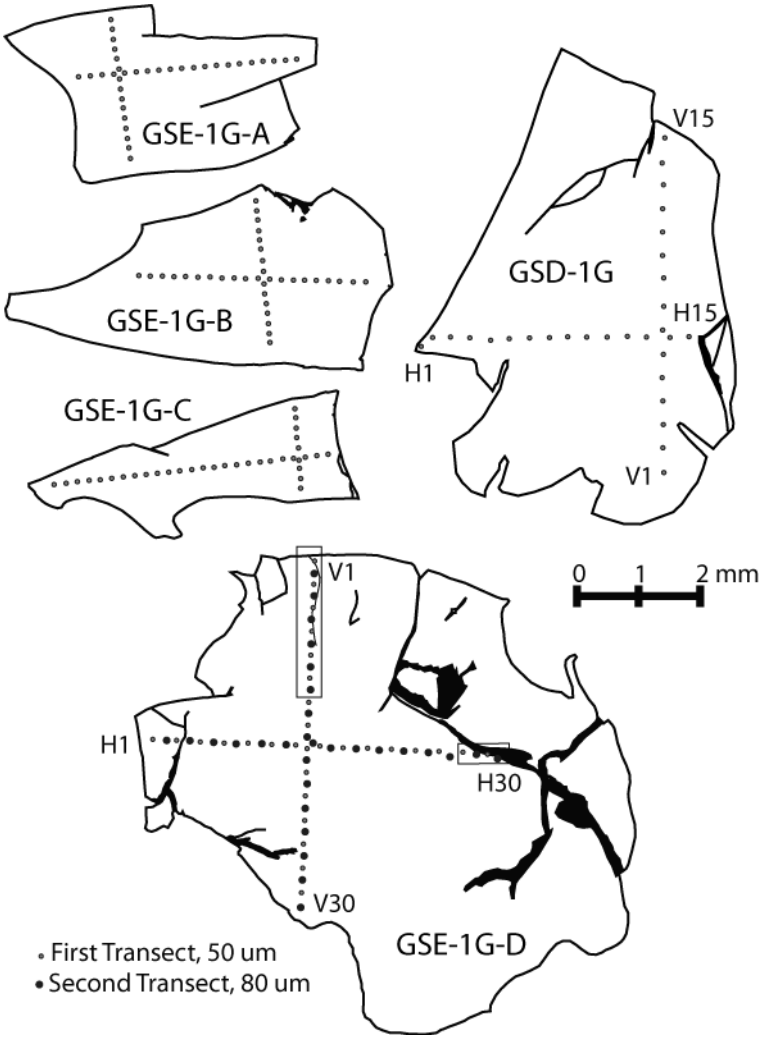

Figure 1.2. Traces of all chips of standard glass used in transect analyses. Also shown are locations of spot analyses in transects. Note that GSE-1G A, B, and C also used in the chamber fractionation test (Fig. 3). GSE-1G-E shows the location defects in the glass. Boxes at the start of the vertical and end of the horizontal transect on this chip highlight regions where anomalous LA-ICP-MS measurements are reported (see Fig. 7). Enrichments of volatile elements and depletion of refractory lithophile elements was most pronounced for the first 10 vertical spots corresponding to a hairline fracture in the glass. Similarly, strong depletions of some very volatile elements was observed in the last two horizontal transect points where ablation overlapped a large crack, but the trend may also be seen for the next two spots near the crack. Outside of these regions (highlighted by rectangular boxes) no variations were observed.

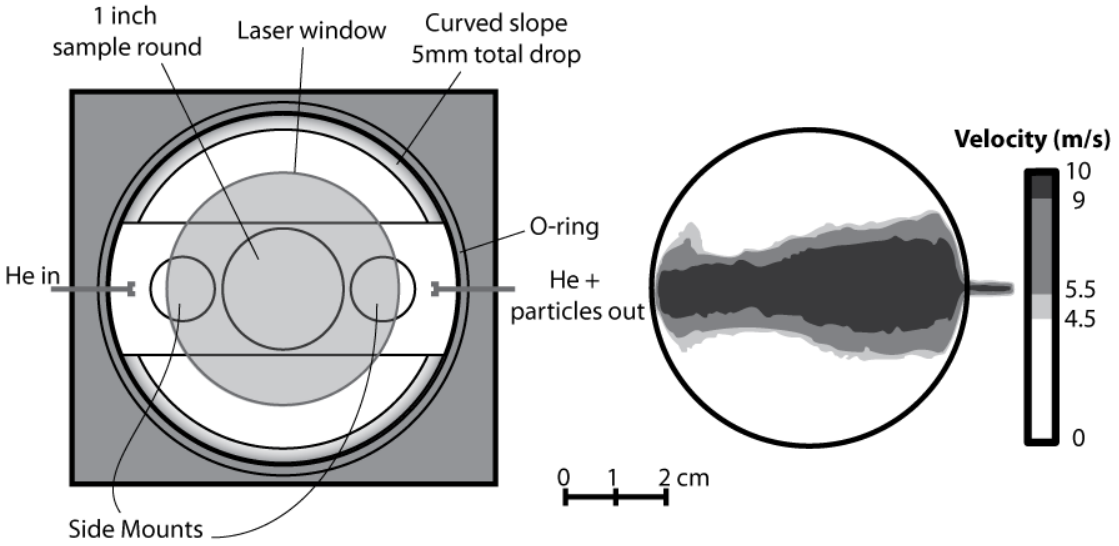

Figure 1.3. Setup of ablation chamber used in all experiments. The chamber is a shallow cylindrical drum ~20 cm^3 volume. During experiments He carrier gas flow was 0.8 L/min from left to right. On the right are the calculated flow velocities modified from Bleiner and Bogaerts (2007, Fig. 6a) for a similar geometry sample chamber (drum-shape, 33 cm^3, He gas flow of 0.5 L/min, scaled to match our sample chamber) illustrating the formation of a distinct high velocity zone across the center of the chamber.

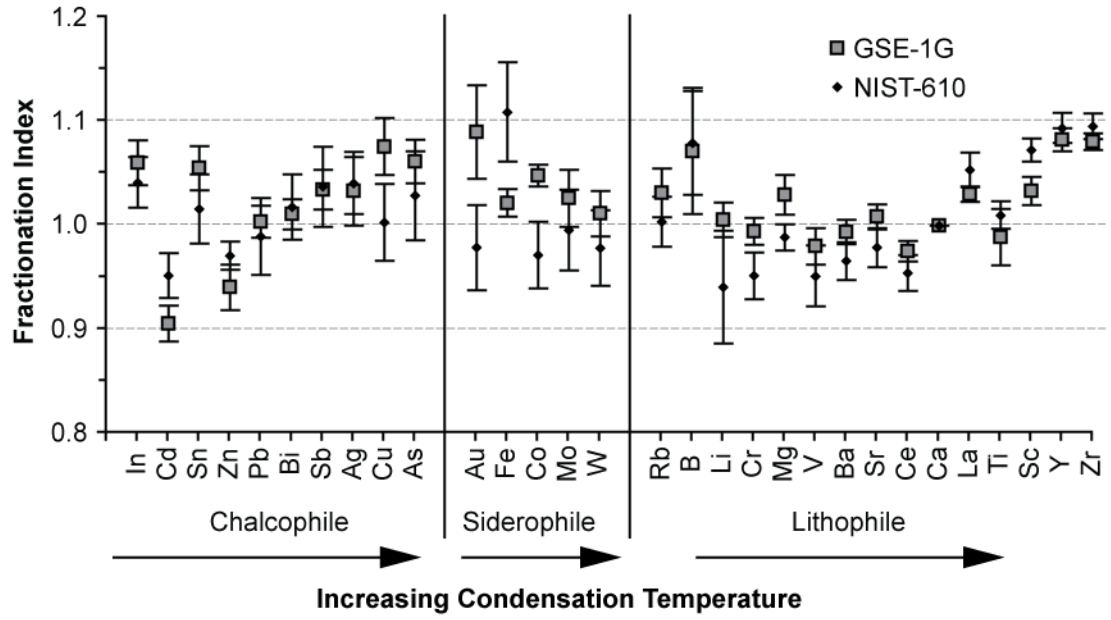

Figure 1.4. Fractionation index for a 120 second ablation of standard glasses. Data are the mean of 5-6 spot analyses (± 2 SE) calculated as the median ratio of [X]/[^{43}Ca] over the last 30 seconds of ablation divided by the first 30 seconds (after Freyer *et al*., 1995; Sylvester, 2002). Within each geochemical affinity group, elements are ordered by increasing condensation temperatures from Lodders (2003). Dashed lines bracket ±10% fractionation. No consistent difference was found for fractionation at different element volatilities or in different matrices despite greater ablation depths in NIST glasses.

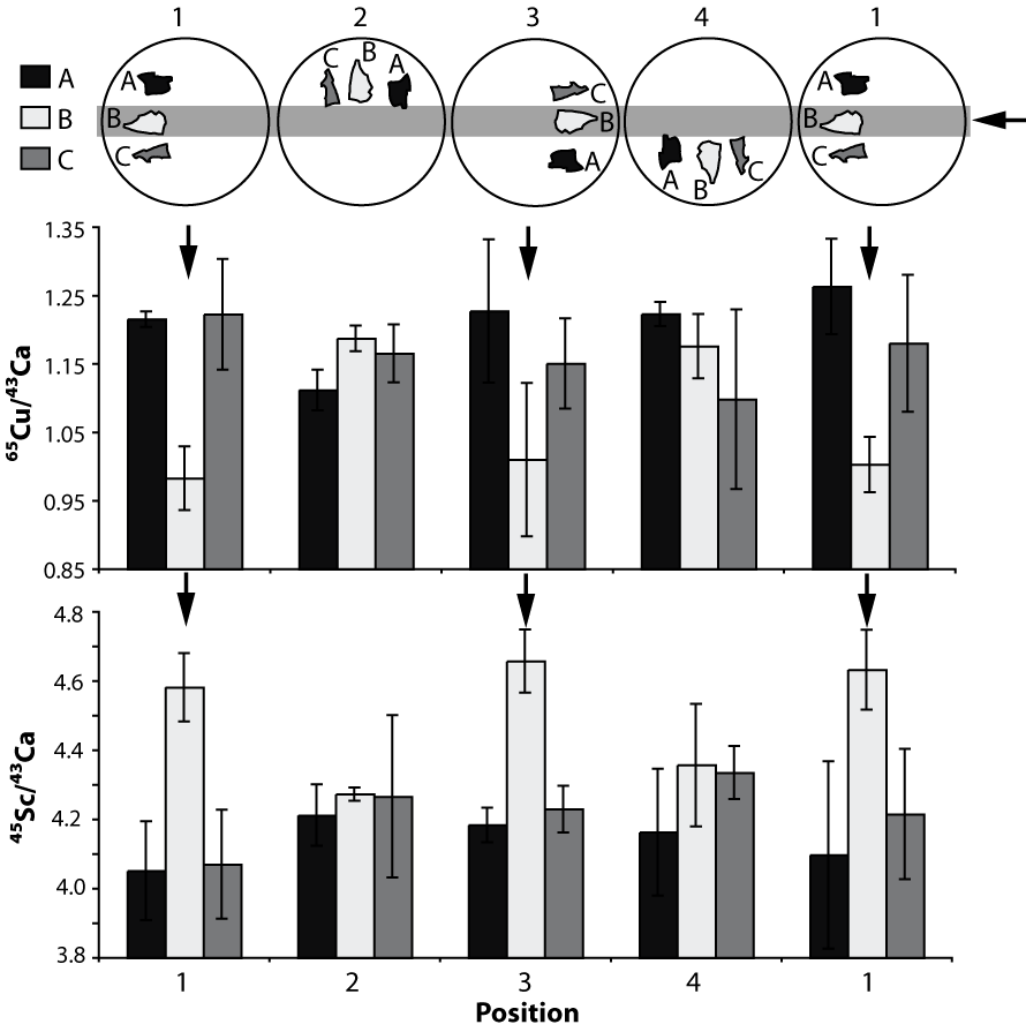

Figure 1.5. Three chips of GSE-1G glass analyzed in different positions within the sample ablation chamber. The shaded region is the center position in the sample chamber in each rotation of the sample mount. Arrows highlight significant enrichment of refractory elements (Sc) and depletion of volatile elements (Cu) while chip B was located in this central region. Bars are mean values for each chip (±2sd, n=3).

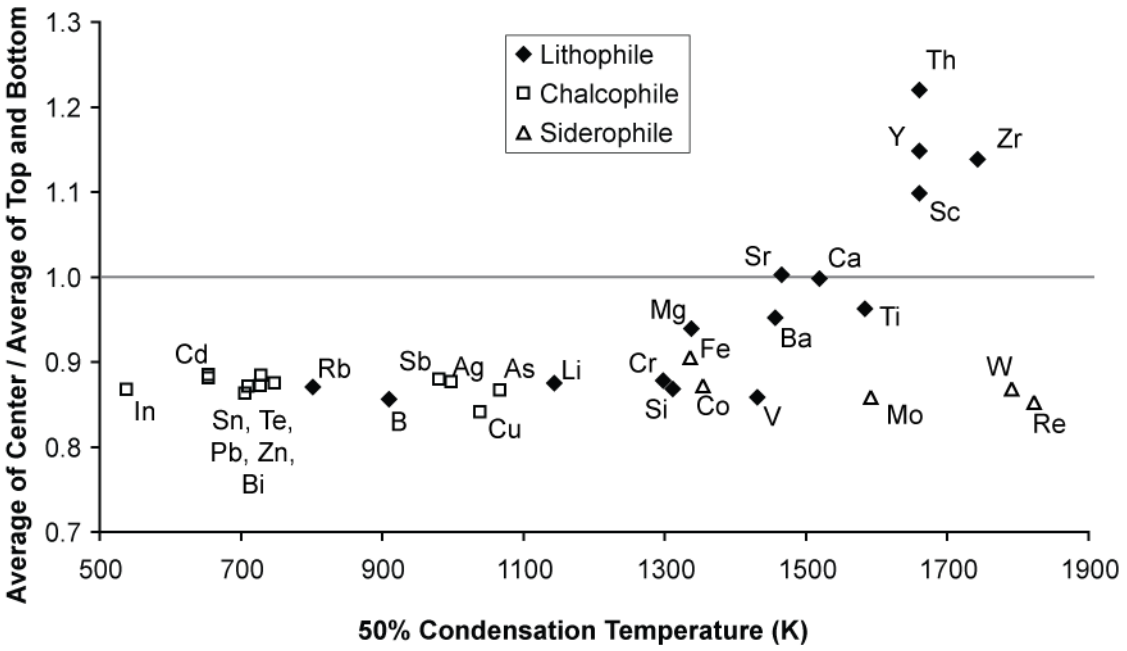

Figure 1.6. Summary of fractionation induced within the chamber. This is quantified by dividing the values of chip A and C in positions 1 and 3 and chip A, B, and C in positions 2 and 4 by the values of chip B in positions 1 and 3 for each normalized ratio measured. Values below one represent elements that are enriched in the top and bottom of the sample chamber relative to Ca, while values above one are enriched in the center of the chamber. Lithophile elements show some indication of a positive correlation with volatility (expressed as condensation temperature; Lodders, 2003) while highly volatile lithophile elements (Rb, B, ± Li) and all chalcophile and siderophile elements are consistently enriched in the top and bottom of the chamber by 10-15% with no relation to condensation temperature.

Table 1.2. Summary of uncertainty sources during LA-ICP-MS analysis of GSE-1G.

Isotope	GSD-1G			GSE-1G			
	Standard Conc. (ppm)[1]	Average Spot[2] 2 se %	2 sd % for Transects[3]	Standard Conc. (ppm)[1]	Average Spot[2] 2 se %	2 sd % for Transects[3]	2 sd % Sample Chamber[4]
11B	50	3.3	8.2	330	6.3	10.1	19.1
25Mg	21710	1.3	3.5	21107	2.4	4.1	7.3
29Si	248691	1.5	4.4	251028	4.4	8.6	15.4
43Ca	51458	0.0	0.0	52887	0.0	0.0	0.0
45Sc	52	1.5	4.7	530	2.5	4.9	9.2
47Ti	7434	1.1	2.9	450	3.2	5.6	5.9
51V	44	2.1	4.9	440	2.6	5.4	11.3
52Cr	42	1.9	5.9	400	3.2	5.9	12.3
55Mn	220	1.4	4.2	590	2.7	5.0	10.1
57Fe	103381	1.7	4.1	98717	3.0	5.7	11.1
59Co	40	1.8	5.4	380	3.3	6.0	13.7
63Cu	42	2.3	6.3	380	4.6	7.9	19.1
65Cu	42	2.9	6.0	380	5.2	7.0	18.0
64Zn	54	2.7	7.4	460	3.1	6.0	16.2
66Zn	54	2.7	6.5	460	3.4	6.2	16.1
75As	27	2.5	7.9	260	4.1	9.0	17.5
76Se	2	5.7	20.5	20	8.8	13.6	22.1
82Se	2	32.9	64.9	20	17.0		
90Zr				410	2.7	5.7	12.7
95Mo	39	2.9	9.5	390	4.8	7.1	14.7
98Mo	39	2.6	5.6	390	4.0	6.4	14.4
107Ag	23	2.3	8.9	200	4.6	7.9	17.4
109Ag	23	2.5	7.0	200	3.5		
111Cd	18	3.9	12.6	160	4.0		
112Cd	18	2.9	12.6	160	3.0	8.7	17.4
113In	38	2.9	10.7	370	3.8		
115In	38	2.2	7.0	370	3.5	7.1	16.0
118Sn	29	2.6	7.7	280	4.5	6.8	15.1
120Sn	29	2.5	6.3	280	3.8		
121Sb	43	2.3	6.6	450	4.3	6.8	15.0
123Sb	43	2.3	6.9	450	3.8		
125Te		5.4	15.0		5.3	12.1	17.4
140Ce				414	2.2	4.1	6.6
182W	43	2.9	7.5	430	3.7	6.8	12.4
183W	43	3.3	9.6	430	4.1		
185Re		4.3	14.7	120	4.2		
187Re		3.7	14.6	120	4.7	11.9	17.1
193Ir				120	36.6	105.7	110.0
197Au	4	4.4	25.9	7	19.1	69.1	74.3
203Tl	0.9	11.9	32.1	2	16.4		
208Pb				378	3.5	6.5	14.5
209Bi				320	3.1	6.6	14.8

[1]From GeoReM database. [2]Median calculated for individual spots (100+ for GSE-1G, 30 for GSD-1G). [3]Calculated from transects across multiple chips of GSE-1G and GSD-1G after normalization of each transect to its median value correcting for relative fractionation related to position within the ablation chamber. [4]Same as (3), but without normalization to the median value, reflecting overall uncertainty due to differential elemental fractionation within the chamber.

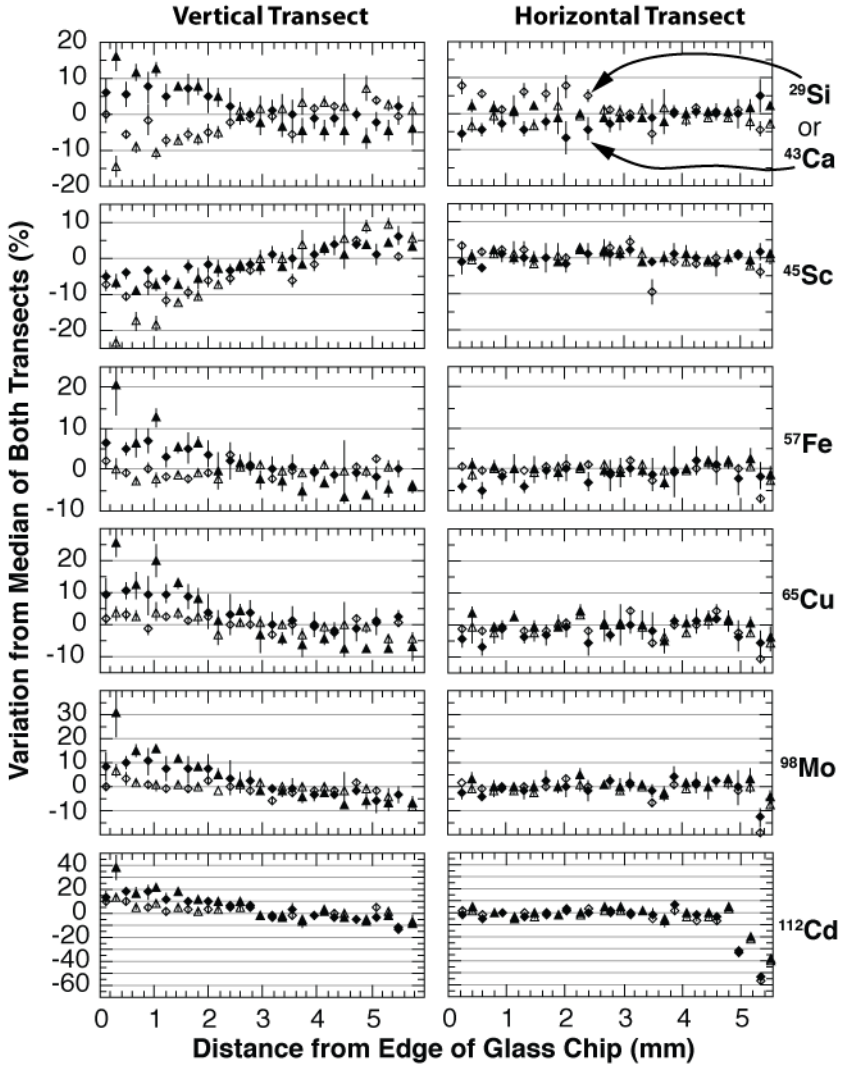

Figure 1.7. Representative elements measured in transects of GSE-1G chip-D. These show a range of fractionation behavior during ablation near or on defects in glass. The start of the vertical transect is marked by enrichment of volatile elements and depletion of refractory elements relative to Ca corresponding to ablations near a small fracture in the glass. The very end of the horizontal transect is marked by depletion of some volatile elements corresponding to an open crack in the surface. Diamonds are from the first experiment with 50 μm spot sizes and triangles from the second experiment with 80 μm spot sizes. Open symbols are normalized to ^{29}Si and filled symbols normalized to ^{43}Ca. Error bars are ± 2 se for each spot analysis. The top two graphs show both Si and Ca (omitting where an internal standard is normalized to itself) showing nearly mirrored behavior along the transect. Normalizing to Si, a more volatile element, reduces the deviations of moderately volatile elements, increases the deviation of refractory elements, and has little effect on volatile elements (e.g., Cd).

Table 1.3. Comparison of average measured EMP values to GeoReM reported values.

	GSE-1G				GSD-1G			
Oxide (wt. %)	EMPA Average	2 sd	GeoREM Value	2 sd	EMPA Average	2 sd	GeoREM Value	2 sd
SiO2	53.24	0.48	53.7	3	53.25	0.62	53.2	1.6
Al2O3	13.78	0.22	13.0	0.8	14.15	0.15	13.4	0.6
P2O5	0.02	0.01			0.22	0.03		
K2O	2.65	0.09	2.6	0.2	3.02	0.17	3	0.2
CaO	7.42	0.11	7.4	0.6	7.27	0.07	7.2	0.2
MnO	0.07	0.04			0.03	0.03		
FeO	12.68	0.35	12.7	0.6	13.71	0.17	13.3	0.2
Na2O	3.84	0.14	3.9	0.4	3.30	0.10	3.6	0.4
MgO	3.57	0.07	3.5	0.06	3.55	0.02	3.6	0.08
TiO2	0.08	0.04	0.075	0.014	1.35	0.04	1.24	0.12
Total	97.35	0.66			99.86	0.45		

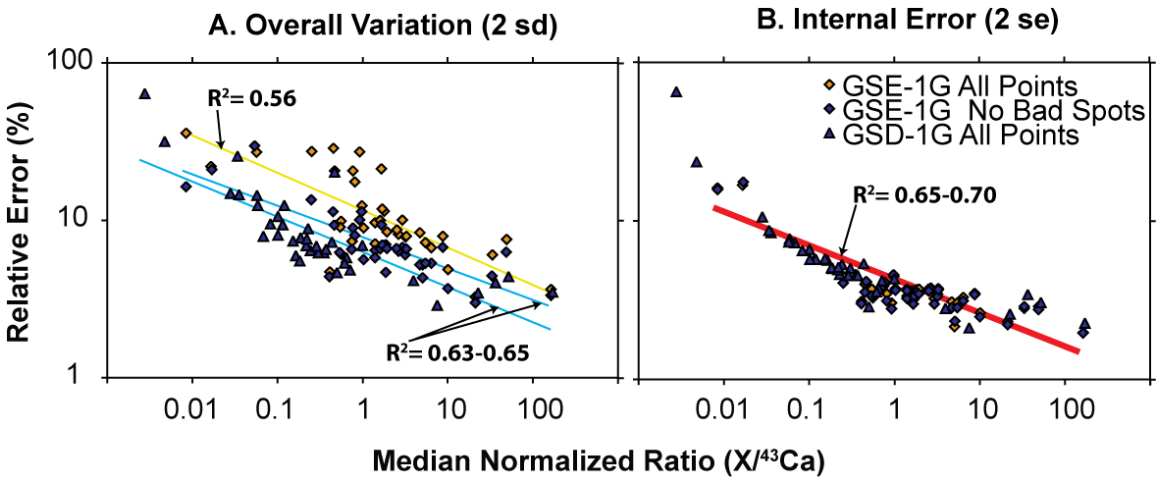

Figure 1.8. Summary of overall variation and internal errors. **A.** Log-log plot showing the relationship between concentration and overall variation (calculated as two relative standard deviations from the median value of 15 spot transects). Counting statistics should produce a linear relationship, as generally seen in GSD-1G. GSE-1G, however, has notable scatter. This could be partially due to heterogeneities induced by ablation near defects in the standard glass. By removing seven spot analyses that were made on or close to defects in the standard glass, GSE-1G has a more linear trend (blue "corrected" points). **B.** Log-log plot comparing the concentration to the mean internal precision for all spot analyses. As expected, almost all error is accounted for by concentration.

Table 1.4. Summary of accuracies[1] and concentrations[2] for analysis with calibration by GSE-1G.

Element	GSD-1G		BHVO-2G		BCR-2G	
	Conc.	Accuracy	Conc.	Accuracy	Conc.	Accuracy
11B	50	1	5.4	50	6	13
24Mg	21710	2	42998	4	21469	1
43Ca	50743	1	81475	0	50457	0
45Sc	52	3	33	2	33	0
47Ti	7434	6	16300	2	14100	0
52Cr	42	10	293	8	17	32
53Cr	42	0	293	7	17	9
55Mn	220	1	1317	19	1550	22
57Fe	103381	1	87835	0	96386	10
59Co	40	0	44	9	38	9
63Cu	42	1	127	11	21	2
65Cu	42	1	127	9	21	2
66Zn	54	0	102	30	125	41
75As	27	7	Conc. Unkn.		Conc. Unkn.	
85Rb	37.3	2	9.2	6	47	8
95Mo	39	2	3.8	30	270	7
98Mo	39	2	3.8	16	270	9
107Ag	23	4	Conc. Unkn.		0.5	191
111Cd	18	12	0.1	23	0.2	1
112Cd	18	8	0.1	76	0.2	10
113In	38	10	0.1	69	0.11	98
115In	38	4	0.1	1	0.11	1
118Sn	29	5	2.6	40	2.6	29
120Sn	29	6	2.6	36	2.6	25
121Sb	43	1	0.3	36	0.35	31
137Ba	67	7	131	2	683	2
139La	39.1	0	15.2	7	24.7	8
140Ce	41.4	5	37.6	3	53.3	7
182W	43	3	0.23	13	0.5	16
197Au	4	4	Conc. Unkn.		Conc. Unkn.	
208Pb	50	2	1.7	18	11	13
209Bi	35	6	0.01	93	0.05	28
205Tl	0.9	8	Conc. Unkn.		0.3	8

[1] Accuracy calculated as 100%*Measured Value / Reported Value. 2 Concentrations from GeoReM database, except B for BHVO-2G from Kent and Ungerer (2006).

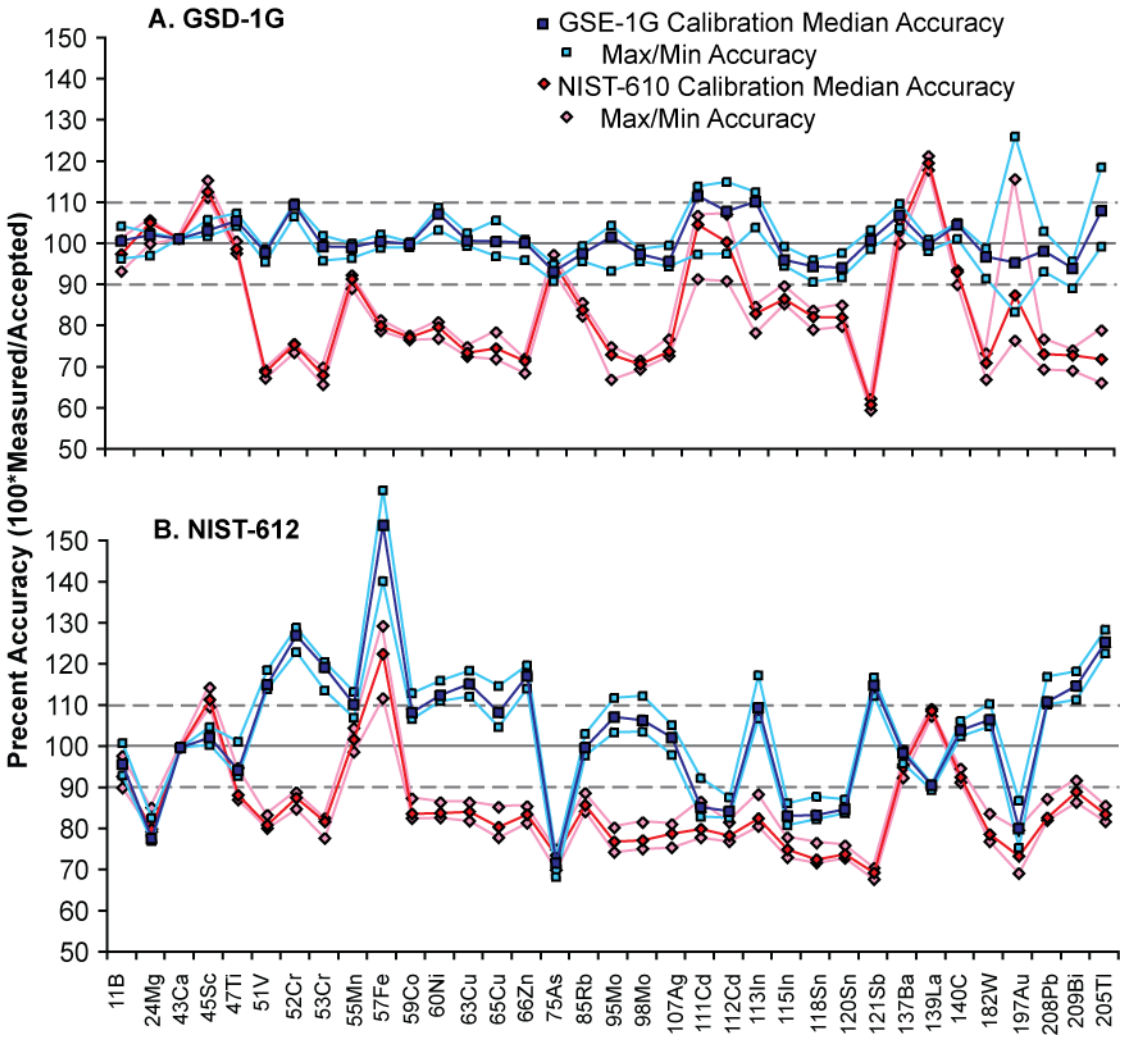

Figure 1.9. Summary of accuracy with different calibration standards. **A.** Comparison of accuracies for GSD-1G glass using GSE-1G and NIST-610 glass as the calibration standards (based on the median of 5 analyses). More accurate results are consistently found using GSE-1G as a calibration standard, possibly due to better matrix matching between the materials (both are basaltic compositions). **B.** Comparison of accuracies for NIST-612 glass using different calibration standards (based on average of 5 analyses). Calibration with GSE-1G appears to be slightly more accurate overall.

3. Controls of Trace Metal Behavior in the 1959 Kilauea Iki Eruption

Introduction

The trace element contents of basalt are an essential tool in understanding petrogenesis in all tectonic environments. Traditionally, studies utilize the common lithophile elements such as large ion lithophile and low field strength elements (Cs, Rb, Ba, Sr), high field strength elements (Sc, Y, Th, U, Zr, Hf, Nb, Ta, U), and rare earth elements (La thru Lu). Many other chalcophile and siderophile elements (e.g., Cu, Zn, As, Se, Mo, Ag, Cd, In, Sn, Sb, W, Pb) along with some semi-volatile lithophile elements (e.g., Li, B) can be analyzed but may not be considered in typical igneous petrology studies, although they are commonly considered in economic studies. These trace elements, however, have the potential to contribute essential clues to the petrogenesis of basalts. Their affinity to complex or bond with volatile species (e.g., S, Cl) results in their concentrations being controlled by partitioning into brine or vapor phases, or crystallizing into sulfide phases (e.g., Holland, 1972; Candela and Holland, 1986; Sun *et al.*, 2003; Simon *et al.*, 2006; Collins *et al.*, 2009; Pitcher *et al.*, 2009; Witt-Eickschen *et al.*, 2009; Zajacz and Halter, 2009). In addition, an understanding of the movement of these elements, and the processes that control these movements, is fundamental for understanding how metals in magmatic-hydrothermal ore deposits are concentrated and the implications for the volcanic contribution of metals into the ocean and atmosphere (Rubin, 1997; Sinton and Duncan, 1997; Hinkley *et al.*, 1999).

The 1959 eruption of Kilauea Iki, Hawaii, provides an ideal system to investigate the fundamental behavior of many chalcophile and siderophile trace elements and to compare the behavior of refractory and semi-volatile elements in a shallow basaltic volcanic system. On a broad level, the Kilauea Iki compositional evolution is literally a textbook example of magma diversification by olivine control (Winter, 2001), and thus potentially represents a well-behaved system where more subtle variations due to degassing or other processes may be identified. The samples are also ideally suited for olivine-hosted melt inclusion studies as many are picritic with large olivine phenocrysts. In addition, the sequence of the eruption was extensively documented and sampled by

staff at the USGS Hawaiian Volcano observatory (Murata and Richter, 1966a; 1966b; Richter and Murata, 1966; Richter *et al*., 1970). Previous work has refined our understanding of mixing and fractionation controls on major element chemistry (Wright, 1973), olivine chemistry and petrography (Helz, 1987), and volatile abundances and character of trapped melt inclusions (Anderson and Brown, 1993; Wallace and Anderson, 1998).

The goal of this study is to examine the trace element composition of both classic lithophile trace element suites and semi-volatile trace elements of glass and melt inclusions from the 1959 Kilauea Iki eruption with the goal of constraining the effect of mixing, fractionation, and potential volatility on trace element evolution.

Background to the 1959 Eruption of Kilauea Iki

Kilauea Iki crater is located on the east side of the Kilauea Caldera on the Big Island of Hawaii (Fig. 2.1). The summit eruption of Kilauea Iki eruption began on November 14th and continued through December 20th, 1959, consisting of 17 phases of fire fountaining each of which partially filled the Kilauea Iki crater with a substantial lava lake that partially drained back into the vent following each phase (detailed chronology by Richter, 1970). The first phase followed a 3-month period of precursory seismicity and inflation that began with a deep (55 km) earthquake swarm August 14-19 followed by intermittent and progressively shallower earthquakes and rapid inflation in November (Eaton and Murata, 1960). The eruption began on November 14 as a 750 m long fissure with 30 m high fire fountains, but quickly coalesced into a single vent. Over the course of the eruption, the fire fountains reached up to 500 m high with incandescent scoria observed to over 650 m (3rd phase, November 28) spreading a wide tephra deposit outside of the Kilauea Iki crater (Fig. 2.1). Lava temperatures at the vent were variable with the highest recorded (1192 °C) midway through the eruption on December 4. Over this time the lava lake filled to a maximum depth of 125 m on December 10 covering an area of 61 hectares. The majority of the volume was erupted during the first phase of the eruption (30 million m^3) while later phases added smaller amounts (2-10 million m^3), most of which drained back into the vent at the end of each cycle (Murata and Richter, 1966a).

On January 13th, nearly a month after the end of the summit eruption, a flank eruption began and continued through mid-February 1960. The compositions of this eruption were more similar to material from an earlier eruption of Kilauea in 1955 (Murata and Richter, 1966a; Wright and Fiske, 1971).

Initial chemical and petrological investigations highlighted the primary role of olivine in compositional trends during the eruption. Whole rock concentrations of MgO ranged from 7-19 wt. % and could be explained solely with addition or removal of Fo87 olivine (Murata and Richter, 1966a). Measured temperatures during the eruption ranged from 1060-1190 °C (Ault *et al*., 1961), with higher temperatures and discharge rates both correlating closely with more Mg-rich lavas (Murata and Richter, 1966a,b). In addition, Murata and Richter (1966a,b) recognized two distinct compositional endmembers in samples from the beginning of the eruption in samples S-1 and S-2. S-1 lies off olivine control lines and is richer in CaO while S-2 marks the least magnesian endmember of the olivine-control line. Murata and Richter (1966b) concluded that the more picritic compositions from later phases in the eruption were the result of eroding accumulated olivine in a shallow magma chamber during periods of rapid eruption rates.

Subsequent studies have carefully documented mixing endmember's affect on the composition, origin and character of olivine, as well as melt inclusion volatile contents which provided control on the pressure and temperature conditions of olivine crystallization (Wright, 1973; Helz, 1987; Anderson and Brown, 1993; Wallace and Anderson, 1998). Wright (1973) performed detailed modeling and concluded that the proportion of the S-1 and S-2 endmembers varied throughout the eruption, although the least magnesian and most distinct endmembers erupted only during the first phase from each end of the initial fissure. This study concluded that the two components were either separate magmas emplaced beneath the summit and internally stratified, or that the two components are both derived from a common parent with the S-1 endmember subsequently enriched in clinopyroxene either by gravitational settling or flow segregation.

A detailed study of olivine phenocrysts and a few glass compositions by Helz (1987) significantly refined the mixing model. Based on observations of deformed "kink-

banded" olivines, thermally annealed aggregates of olivine, megacrysts of olivine, and olivine with sulfide inclusions, this study concluded that the more magneisan and higher temperature S-1 endmember originated from ~45-60 km depth during an August earthquake swarm with these focal depths. This study rejected the earlier models that relate the differences between the two endmembers solely to clinopyroxene control, noting that the model requires both S-1 and S-2 to be stored for a prolonged period in summit magma chambers, a process inconsistent with seismic signals and the presence of deformed olivines that require residence at high pressure. In addition, there are no observed clinopyroxene phenocrysts in thin sections from erupted scoria or in any drill core samples from the lava lake. Helz (1987) instead argues that the S-1 endmember is probably the newer component based on the observation that S-2 compositions are occasionally seen as an almost pure endmembers throughout the eruption while the arbitrarily defined S-1 composition rarely occurs as an uncontaminated endmember, consistent with new S-1 magma traveling through a shallow magma chamber of S-2 composition. The S-1 component is also associated with higher MgO content, and therefore higher temperature, glass.

Detailed analysis and characterization of melt inclusions from the 1959 eruption by Anderson and Brown (1993) and Wallace and Anderson (1998) provide an estimate of the pre-eruptive volatile contents of the magma, although these could not be directly related to the two compositional endmembers. Anderson and Brown (1993) calculate that most (41/50 measured) of the melt inclusions were trapped at very shallow pressures (<1 kb) while only two measured inclusions appear to be trapped from greater depths (>2 kb). High CO_2 contents (0.2 wt.%) are suggested as the primary driver for the observed fire fountaining. They note that while inclusions have variable CaO contents, they are generally more like the S-1 component suggesting that they grew in the shallow chamber as a direct result of mixing between a cooler chamber with the new hot magma from depth. Wallace and Anderson (1998) reexamined the data of Anderson and Brown (1993), adjusting many of the water contents for previously measured melt inclusions and concluding that the highest water contents were trapped in early melt inclusions. Repeated draining of degassed lava from the lava lake was interpreted to have

subsequently reduced water contents of melts trapped in inclusions that were erupted later in the eruption.

The model presented by the previous studies has several common characteristics: (1) the majority of major element compositions in whole rock samples can be explained with addition or removal of olivine + Cr-spinel (e.g., Murata and Richter, 1966a); (2) at least two distinct magma compositions are present, as defined by different CaO compositions and these are variably mixed throughout the eruption, probably representing a deep magma released from below 50 km and a shallow reservoir (Wright, 1973; Helz, 1987); and (3) the eruption was driven by high volatile contents, which were modified over the course of the eruption with drainback of the lava lake (Anderson and Brown, 1993; Wallace and Anderson, 1998). Synthesis of the physical and petrologic model presented in these studies is conceptualized in Figure 2.2. Even with this model, however, several outstanding questions remain regarding the genesis of the 1959 eruption: (1) what was the origin of the two compositional endmembers, and (2) how did semi-volatile trace elements respond to degassing of volatile species, both in response to syneruptive degassing and also due to repeated draining of degassed lava back into shallow lava reservoirs?

This paper investigates both of these questions, first by evaluating the major and trace element compositions of matrix glass and olivine-hosted melt inclusions. Ratios of trace elements incompatible in olivine provide clear evidence that the eruption coincided with mixing between two distinct magma batches, although it remains unclear if these batches are from two distinct mantle source regions or are primarily different degrees of partial melt. Since sulfur in matrix glasses clearly records a degassed composition relative to melt inclusions, we can hypothesize that trace elements with semi-volatile behavior might also be depleted and use sulfur as a measure of the extent of shallow degassing.

Methods

Glass samples collected and by the USGS during the 1959 eruption were provided by the Division of Petrology and Volcanology, Department of Mineral Sciences,

Smithsonian Institution. These samples spanned the entire range of the summit eruption. Glass samples were picked by binocular microscope to include only glassy material with minimal vesiciles. Samples were subsequently mounted in 1-inch epoxy rounds and polished with diamond and alumina polishing compounds down to a 1 μm grit. Over 100 olivine grains separated from picritic scoria collected by Adam Kent were also mounted in epoxy and arbitrarily polished midway through grains until 3-7 melt inclusions were exposed in each mount (4 total mounts were made). Although this preparation does not allow for careful examination of each melt inclusion for cracks and secondary inclusion phases, it provides a large and somewhat random population of inclusions for analysis (Fig. 2.3). Previous detailed studies of melt inclusions (Anderson and Brown, 1993; Wallace and Anderson, 1998) from this eruption serve as a guide to the compositional variation and textures, and monitoring sulfur content by EMPA provides a robust means to identify any inclusions that degassed at shallow pressures through fractures in the host or glass isolated within olivine as a relic of the polishing process that can resemble melt inclusions in reflected light (Nielsen *et al*., 1998).

Matrix glass, olivine, and melt inclusion compositions were analyzed by electron microprobe (EMPA) at Oregon State University using a Cameca SX100 Electron Microprobe Analyzer. For glass analyses, a focused 5 μm beam with a 15 keV accelerating voltage and 30 nA beam current was used with variable peak count times: 20 seconds (s) for Si, Al, Na, and Ti; 30 s for K, Ca, Mn, and Fe; 40 s for Cr; and 60 s for P, S, Cl, Ni, Mg, and F. Olivine was analyzed with a focused 1 μm beam and the same accelerating voltage and beam current but different peak count times: 10 s for Si and Al; 20 s for Mn, Na, and Mg; 30 s for Fe, Ni, Ca, Ti, and Cr; and 60 s for K. Makaopuhi Lava Lake basaltic glass (USNM 113498/1 VG-A99, "BASL") was analyzed during calibration and unknown analyses to monitor for accuracy and stability. Long-term stability of this standard as well as accuracy of secondary standards (BHVO-2G, BCR-2G, GSD-1G) are shown in Table 2.1. Concentrations reported here are generally the averages of 2 analyses unless one of the measurements was obviously in error.

Trace element analysis was carried out by laser ablation-inductively coupled plasma-mass spectrometry (LA-ICP-MS) at Oregon State University using a NewWave

DUV 193 nm Ar-F laser attached to a VG PQ Excell quadrapole mass spectrometer. GSE-1G was used as a calibration standard (Chapter 2) while GSD-1G and natural glasses were used as secondary standards. Sources of error and more detailed analytical procedure are available in Chapter 2. Data were processed using in-house LaserTRAM and LaserCalc software, which use a Visual Basic script operated in Microsoft Excel. These programs allow for manual selection of a 20-30 second background interval and a 15-30 second ablation interval. The software normalizes each analyte mass to the ^{43}Ca internal standard and calculates a concentration of the analyte using the Ca concentrations determined by EMPA. Standardization is provided by multiple measurements of GSE-1G that was analyzed once every 5-10 unknowns over the course of an experiment. Reported errors are 2 standard error (se) of 5 sub-intervals for each ablation propagated with both the uncertainty in repeated measurements of the calibration standard (GSE-1G) and uncertainty in Ca concentration measured by EMPA. Reported concentrations are again the average of 2-3 analyses for each sample. A list of all measured isotopes and average concentrations for glass, melt-inclusion, and olivine is reported in Table 2.2.

Melt inclusion data were monitored for Mg, Si, Ti, Mn, and Cr providing a means to reject analyses where host olivine or other included phases may have been ablated (Fig. 2.4). Samples with Mg, Si, and Ti values exceeding that of EMP analyses were removed from the data set. In addition, Zn and Mn both have similar partitioning behaviors in olivine, yet Mn was analyzed only by EMPA and Zn only by LA-ICP-MS. Samples with high Zn and low Mn likely result from accidental ablation of host olivine (Zn in olivine ~100 ppm) and also were also removed. In addition, a few matrix glass Fe concentrations were well outside the range of whole rock and the majority of glass analyses. The origin of these is unclear but they may reflect analyses with other minerals in the analytical volume or adjacent to an Fe-rich phase.

Melt Inclusion Corrections

Melt inclusions, small portions of melt trapped inside phenocrysts during crystal growth, have the potential to shed light on parental magma compositions not expressed at the surfaces, such as undegassed volatile concentrations, since inclusions are typically

trapped at higher pressures than erupted glass (Schiano, 2003; Kent, 2008). A primary concern about the trapped compositions that melt inclusions provide centers on the possibility of preferential incorporation of anomalous boundary layer compositions (Roedder, 1984; Kent, 2008). Boundary layer development results when crystal growth outpaces elemental diffusion in a melt resulting in a region enriched in elements incompatible with the growing phenocryst and depleted in compatible elements (e.g., Lu *et al*., 1995). Growth mechanisms of host crystals are key in understanding the potential to trap a boundary layer.

There are two major classifications of melt inclusions related to growth mechanisms: (1) primary inclusions formed simultaneously with crystal growth, and (2) secondary inclusions forming after the crystal in cracks and embayments (Roedder, 1979; Roedder, 1984; Schiano, 2003). During slow rates of crystal growth and minimal undercooling, simple defects in growth structure, such as spiral growth dislocations, can result in primary inclusions within a polyhedral structure, whereas rapid diffusion-controlled growth can result in primary inclusion entrapment as dendritic arms merge together sealing off a region from the melt (Faure and Schiano, 2005). Most commonly referenced, however, is a two-stage cooling model where rapid growth leads to dendritic or hopper forms, followed by slow polyhedral and tabular overgrowths (Kohut and Nielsen, 2005; Blundy and Cashman, 2005; Baker, 2008). These overgrowths then trap melt inclusions. Experimental work by Kohut and Nielsen (2005) reported that melt inclusions did not form during the cooling stages of the experiment, but only during isothermal conditions (greater than 6 hours) as rapid growth textures (dendritic or hopper) were annealed by tabular overgrowths. Although boundary layer trapping has been identified in experimental studies and some observational studies (e.g. Faure and Schiano, 2005; Baker 2008; Milman-Barris *et al*., 2008), the lack of evidence for incompatible element enrichment corresponding to melt inclusion sizes down to ~30 μm in the vast majority of natural inclusion suites suggests that, at least for basaltic melts, diffusivities are rapid enough to balance any boundary layer effects (Nielsen *et al*., 1998; Kent, 2008).

Post-entrapment modification, however, affects all compositions measured in this study to some extent. Post-entrapment crystallization (PEC) of host olivine along the walls of the inclusion after entrapment can easily be modeled. In samples from Kilauea Iki, however, melt inclusions are not only lower in Mg, but also lower in Fe compared to what can be predicted using the liquid line of decent for whole rock and matrix glass compositions (Fig. 2.5). This loss of iron is described as diffusive Fe loss by Danyushevsky *et al*. (2000) and can be corrected for by various methods (Cottrell *et al*., 2002; Gaetani *et al*., 2002; Kent, 2008).

We use an iterative calculation with the geothermometer of Putirka *et al*. (2007) to correct measured melt inclusion values back to equilibrium with their host olivine. In this experimentally calibrated model, two equations relate the olivine/melt distribution coefficients of Mg and Fe to pressure (P), temperature (T), and melt composition (H_2O, Na_2O, K_2O, SiO_2):

(1) $\ln D_{Mg}^{ol/liq} = -a + b * (P/T) - c*[H_2O] + d/T + e*[Na_2O + K_2O]$

(2) $\ln D_{Fe}^{ol/liq} = -a + b * (P/T) - c*[H_2O] + d/T + e*[Na_2O + K_2O] + f*[SiO_2]$

where a, b, c, d, e, and f, are constants defined for each equation in Table 2.3. We use pressures and water contents from previous melt inclusion studies (Anderson and Brown, 1993; Wallace and Anderson, 1998), FeO*/FeO from whole rock wet chemistry (Murata and Richter, 1966a), and Mg and Fe concentrations measured in host olivine. The correction begins with an initial temperature of 1500 °C (well above any expected crystallization temperatures for Hawaii) and the measured melt inclusion composition. Temperatures are then iteratively decreased in 1-degree steps calculating an equilibrium Fe and Mg concentration for the melt on the basis of partitioning between melt and host olivine. The difference between the original Mg measured in the melt inclusion and the calculated Mg is used to determine the amount of olivine added back by the correction. All elements are then corrected for this amount of crystallization by mixing measured concentrations with the measured or estimated host olivine composition. Future temperature steps of the iteration then will refer back to these new compositions. The iteration is continued until Mg-Fe concentrations lie along the liquid line of decent as defined by whole rock and glass data (Fig. 2.5). Note that FeO* measured here by EMPA

are generally 0.5 wt.% lower than previous analyses of either glass (Helz, 1987) or whole rock (Murata and Richter, 1966a) samples from Kilauea Iki, yet slopes of FeO* evolution with MgO are similar. We use our measured FeO* values for internal consistency, but note that these may be systematically offset from values determined in other studies due to calibration settings unique to our analyses (FeO* is calibrated on an Fo83 crystal standard, not basalt glass). In analyses of secondary standards (Table 2.1) FeO* is slightly lower (~3%) than the accepted standard values for a number of basaltic glass standards, but the difference is not enough to explain the offset between the two data sets.

The resulting corrections calculate a median of 10% by weight PEC. For incompatible elements this is will result in a dilution of the measured inclusion concentration of the same amount, which is similar in magnitude to analytical uncertainty for most incompatible trace elements. No PEC corrections were >20%. The value of this model is that it also provides an estimate of the equilibration temperatures that serves as an additional check on the reasonableness of corrections. In addition, by using measured host olivines to correct all elements, we can accurately correct for any trace phases that are compatible in olivine (e.g., Cr, Co, Zn).

It is also important to note that by far the most important parameters in these equations are olivine Mg and Fe compositions and crystallization temperatures. Coefficients reflecting the influence of the melt composition (H_2O, $Na_2O + K_2O$, SiO_2) are all <<1 and thus have little influence on the magnitude of the correction. Pressure is also less important, as Fe-Mg partitioning in olivine is not pressure sensitive. In addition, formation pressures for melt inclusions from Kilauea Iki are well constrained from previous work (Anderson and Brown, 1993).

Results and Discussion

Analyses by EMPA and LA-ICP-MS for matrix glass, corrected melt inclusions, and host olivines are reported in Tables 2.4, 2.5, 2.6, 2.7, 2.8, and 2.9. In the following sections we discuss the trends and significance of major element variations, volatile concentrations, standard trace element compositions, and patterns of trace metals. Within

these sections we identify the effects of fractionation, mixing, and volatile exsolution on compositional variations.

Control on Major Elements and Volatile compositions

Most major element variations observed in melt inclusions and glasses can be explained with fractionation or accumulation of olivine plus Cr-spinel and late fractionation of clinopyroxene, consistent with previous whole rock (Murata and Richter, 1966a) and glass (Helz, 1987) studies (Fig. 2.6). Glass compositions range from 9.72 to 4.84 wt. % MgO with a sharp decrease in SiO_2 and CaO occurring around 7 wt. % suggesting the onset of clinopyroxene crystallization. Aluminum behaves incompatibly over the entire compositional range suggesting an overall absence of plagioclase crystallization. Whole rock compositions (Murata and Richter, 1966a) do not show the same inflection in CaO suggesting that clinopyroxene primarily is a groundmass phase and was generally not removed from the melt.

Corrected melt inclusions record more primitive compositions than matrix glasses and generally fall along compositional evolution paths defined by glass values and whole rock compositions. They are more magnesian than matrix glass (up to 13.46 wt. %) consistent with entrapment of a more primary magma during early olivine growth. Whole rock compositions range up to almost 20 wt. % MgO as a result of olivine accumulation. The most magnesian glasses known from Hawaii are around 15 wt. % MgO (Clague *et al*., 1991; Clague *et al*., 1995) suggesting these melt inclusion compositions are both reasonable and approach that of a primary melt composition.

MELTS modeling (Ghiroso and Sack, 1995; Asimow and Ghiroso, 1998) using two primitive melt inclusions compositions at 1 kbar pressure, QFM redox conditions (to match initial cpx fractionation), and 0.5 wt. % initial water provide a good match to the observed compositional trends and closely match percentages of crystallization calculated with lever law principles. The most primitive melt inclusions require approximately 9-11% crystallization by weight of olivine + Cr-spinel while approximately 7% additional crystallization is required to reach initial clinopyroxene formation. The amount of crystallization of olivine + Cr-spinel + clinopyroxene below 7 wt. % MgO is variable

between 13-22% depending on chosen starting compositions. Since no whole rock compositions record a decrease in Ca this final compositional change is only reflecting late groundmass crystallization and is not a reflection of any actual fractionation.

Incompatible major elements (TiO_2, K_2O, Na_2O, and P_2O_5) all increase with decreasing MgO (Fig. 2.7). Most measured melt inclusions fall in line with the whole rock liquid line of decent, however, a smaller subset of inclusions record extremely low Na, high and low K, and high P values. These anomalous values are not correlated with each other. For instance, low Na samples lie along the liquid line of decent in P and K space, and high P samples are found over the entire range of K concentrations. Analytical uncertainty is not considered a likely source of error since EMPA settings for melt inclusions are identical to those for matrix glasses. These anomalous variations also offset MELTS models when selected primitive melt inclusions used for starting compositions are also outliers. The generated trends, however, closely match that of measured glasses.

One potential explanation for these variations could be boundary layer entrapment. Typically, seeing if melt inclusions fall consistently off the liquid line of decent of two elements with significantly different diffusivities can test this process (Faure and Schiano, 2005; Kent, 2008). P_2O_5 should diffuse slower than TiO_2, which could explain the high P melt inclusions (Fig. 2.8). Milman-Barris *et al*. (2008) also observed that high P zones occur in olivines during rapid growth by solute trapping, and around melt inclusions these zones are typically interrupted by low P halos. If this process occurred in the Kilauea Iki olivines, high P melt inclusions could be the result of interaction with unusually high P host olivine. In addition, Faure and Schiano (2005) also would predict that boundary layer entrapment would enrich melt inclusions in Al compared to Ca. In fact, we observe the opposite (Fig. 2.9). Instead, this relationship shows the affinity of melt inclusions to the S-1 mixing component of Wright (1973), which is generally higher in Ca and lower in Al. This same observation was made by Anderson and Brown (1993) and is consistent with inclusion formation following rapid growth associated with mixing between the two magma bodies.

Anomalous values for K and Na in melt inclusions are not as easily explained. Although Nielsen *et al*. (1998) propose some mechanisms for Na loss in breached inclusions or by contamination, these explanations do not explain variations in both K and Na and are also not expected as the melt inclusions analyzed here are exceptionally well preserved and relatively young. Although we do not have complete observations on the size or content (bubble, inclusions) of these melt inclusions, it is interesting to note that there are inclusions of all shapes, sizes, and with or without observed bubbles and chromite inclusions, that are in line with glass compositional trends for K, Na, and P. Therefore, no physical observations of the melt inclusions alone can explain the anomalies.

Of the volatile elements analyzed by EMPA, only S was detected at appreciable levels and then only in melt inclusions (Fig. 2.10). This pattern is consistent with S degassing from matrix glasses along with CO_2 and H_2O during the eruption (Anderson and Brown, 1993; Wallace and Anderson, 1998). Sulfide saturation is commonly related to FeO content and uncorrected melt inclusions lie very close to sulfide saturated MORB samples (Mathez, 1976). Wallace and Anderson (1998) also calculated that melt inclusions from Kilauea Iki are sulfide saturated based on the calculation of Wallace and Carmichael (1992). This is consistent with observations of rare sulfides in some samples from the eruption pumice (Helz, 1987; Stone and Fleet, 1991; Pitcher *et al*., 2009). Corrected melt inclusions appear to record variable amount of degassing from a sulfide saturated parental melt. It is also possible that minor amounts of sulfide could occur as PEC.

Controls on Lithophile Trace Elements

This work greatly expands the limited lithophile trace element work previously completed on Kilauea Iki (Tilling *et al*., 1987) and provides the means to further evaluate the role and source of mixing between the S-1 and S-2 components. Rare earth elements (REE) measured in glass overlap with previous whole rock analyses showing characteristic enrichment in light-REE (high La/Yb) consistent with partial melting of a deep, garnet-bearing source (Fig. 2.11). La/Yb, however, does not correlate with any

other factors (e.g., MgO, Ce), although relatively high uncertainties on Yb due to low concentrations could obscure any variations due to more subtle difference in degrees of partial melting in a garnet-bearing source region.

Mixing can be investigated by looking at incompatible element ratios that will be unaffected by fractionation of olivine or Cr-spinel. The best example from this data is Sr/Y vs. Zr/Nb (Fig. 2.12). We compare only samples with >7 wt. % MgO so clinopyroxene involvement does not influence on selection of endmember samples. Olivine and Cr-spinel do not significantly incorporate any of these four elements. However, variation in source character or partial melt percentage (especially a garnet-bearing source that would retain Y and to a lesser extent Zr in the residuum) will produce different ratios. Variations on this diagram form an apparent two-component mixing trend. Highlighting the endmembers and comparing the glass compositions to whole rock modeling of Wright (1973) suggests that the high Sr/Y, low Zr/Nb best match Wright's S-1 endmember, while the low Sr/Y, high Zr/Nb match the S-2 endmember.

Other ratio plots can be used to refine understanding of the source of each endmember. While the majority of the two mixing endmember's compositional differences can be explained by different degrees of melt from a garnet-bearing mantle source (Sc, Y, Zr, Hf, and Yb are all relatively compatible in garnet compared to Rb, Ba, and Ce, a higher degree of partial melt would release more of these compatible elements explaining the S-2 component), other ratios are more difficult to model. La/Ce, Ba/Th, and Sr/Ba are clearly distinct for both endmembers yet are more difficult to explain varying degrees of partial melt of a garnet-bearing source region (Fig. 2.12). A larger degree of partial melt changes these ratios much less than that of Sr/Y or Zr/Nb, yet identical partial melt models overestimate the Sr/Y variation and are not large enough to explain La/Ce, Ba/Th, or Sr/Ba ratios. Also, Sr/Ba should negatively correlate with La/Ce in melts derived from variations in partial melting of a homogenous source, instead the observed mixing trend is a positive correlation. These inconsistencies suggest that at least some of the variation between these two sources is probably a reflection of mantle source heterogeneities. This conclusion is also consistent with the lack of variation in REE

patterns between the two endmembers since variation in partial melting of garnet should strongly increase La/Yb ratios (compatibility in garnet of Yb >> La; Fig. 2.11).

The earliest hypothesis for the S-1 and S-2 components involved fractionation of clinopyroxene between the two endmembers, thus explaining the prominent difference in Ca (Murata and Richter, 1966a). If this were the case, Nd/Zr should increase with clinopyroxene involvement (in S-1) since Nd is more compatible in clinopyroxene than Zr, while garnet involvement would produce the opposite trend with Zr more compatible than Nd. Figure 2.12 shows what may be a clinopyroxene signature. If clinopyroxene distribution between the two magmas is a significant factor, it complicates any source interpretations that can be made. However, an important observation is that glasses that have clearly experience clinopyroxene fractionation (< 7 wt. % MgO) are not anomalous with respect to Nd/Zr, suggesting that this variation is probably not due to shallow clinopyroxene redistribution as originally suggested by Murata and Richter (1966a).

With compositional endmembers defined by trace element ratios, the compositional variations of most trace elements are easily explained. Trace elements compatible in olivine or Cr-spinel (Co, Ni, Cr) positively correlate with MgO in matrix glass, consistent with a fractionation model (Fig. 2.13). Ni and Cr both decrease by 60-70% over the range of glass compositions. Co and Sc decrease to a lesser degree (only ~25%) and are considerably more scattered. Unfortunately, these elements were not analyzed in host olivines, although data from the literature and analyses of olivine from Loihi seamount (not reported here) confirm that Ni, Cr, and Co are all highly compatible. Since we have no measured values for these elements, corrections to melt inclusions assume that concentrations are zero, resulting in corrected values falling well below the trend of glass compositions and therefore the corrected concentrations for melt inclusions are not representative of actual magmatic values.

Incompatible trace element patterns are bracketed by the identified S-1 and S-2 endmembers and olivine-control fractionation lines (Fig. 2.14 and 2.15). Within error, mixing between the identified S-1 and S-2 endmembers along with olivine fractionation can bracket the compositions of Ce, Rb, Zr, Y, Ba, Sc, Hf, and La at MgO > 7 wt. %. Concentrations of Sr are indistinguishable between the two endmembers and the overall

trend is relatively tight, increasing by 25% over the course of olivine fractionation, while Sr decreases at MgO < 7 wt. % with the addition of clinopyroxene control.

These trace element data highlight the role of magma mixing in the 1959 eruption of Kilauea Iki. Although mixing was recognized with major element data (Murata and Richter, 1966a; Wright, 1973), it was not emphasized until detailed studies of olivine phenocryst textures were made (Helz, 1987). Unlike major element data that are largely controlled by olivine fractionation, trace elements are highly controlled by mixing between the S-1 magma (richer in Rb, Ba, Ce and to a lesser extent V, Cu, and Zn) and the S-2 magma (richer in Sc, Y, Zr, La, Hf, and to some extent Yb). Although some of the variations could be due to increased partial melting of a garnet-bearing source, as discussed above, modeling of partial melt does not match all the trends. A more viable explanation may be that the magmas originate from distinct mantle sources.

Previous work by Helz (1987) argued that mixing probably occurred immediately prior to the eruption based on the timing of the deep earthquakes in August and heterogeneous glass compositions that suggest the magma was not fully equilibrated upon eruption. This study also notes that while many of the diverse olivine textures from the Kilauea Iki eruption are preserved for decades in the lava lake, compositional variations are not. Wright (1973) calculated that variable proportions of the S-1 and S-2 endmembers throughout the 1959 eruptive period suggest that some portion of the two chambers remained distinct during the eruption while each contributed magma to the conduit. The unusually shallow trapping pressures for the majority of inclusions noted by Anderson and Brown (1993) is consistent with this model if mixing between thermally distinct magmas triggered rapid olivine growth and resulting melt-inclusion entrapment.

Semi-Volatile Trace Metal Behavior

While lithophile trace elements constrain the controls of mixing and fractionation at Kilauea Iki, semi-volatile chalcophile and siderophile elements have the potential to record some degree of volatile mobility related to subaerial degassing (e.g., Norman *et al*., 2004; Collins *et al*., 2009; Zajacz and Halter, 2009). We have already assessed degassing using sulfur content. Existing studies show that sulfur degasses at low

pressures (< 3 MPa) within subvolcanic systems at Kilauea (Gerlach, 1986). The sulfur difference between melt inclusions and matrix glasses is consistent with extensive degassing of sulfur at shallow pressure during eruption (Fig. 2.10). While pervasive degassing of sulfur and other highly volatile species is a common observation in volcanic eruptions, other studies have also noted the atmospheric release of many metals (e.g., Pb, Cd, Cu, Zn) at Kilauea (Hinkley *et al*., 1999) during this process, and apparent submarine release of trace metals at Loihi Seamount (Rubin, 1997).

Here, potential volatile loss of trace elements has been examined several ways. First, metals and metal/Ce ratios (to account for fractionation) have been examined against MgO and S (Fig. 2.15 and 2.16). These figures show that there is no clear difference between melt inclusions and matrix glasses related to degassing of sulfur as evident by overlapping concentrations in melt inclusions and matrix glasses. In addition, all incompatible trace elements were examined against incompatible and refractory lithophile elements with similar mineral-melt partitioning (Ce variation diagrams shown in Figures 2.17-2.20). Once again, no differences were observed between matrix glass and melt inclusions suggesting minimal volatile loss during the eruption. Many elements with observed volatile behavior in Hawaii (e.g., Re, Cd, Bi; Norman *et al*., 2004; Pitcher *et al*., 2010) were measured but have concentrations too low to reasonably interpret variations.

Similar increased scatter on Ce variation diagrams for some semi-volatile elements (e.g., Cu) has been proposed by Collins *et al*. (2009) at Mt. Etna, Italy, to be a signature of volatile fluxing. Incompatible elements controlled by fractionation with no volatile behavior should form a tight correlation with Ce (e.g., Fig. 2.17). Volatile addition or degassing, however, would result in scatter from this fractionation trend. We see such scatter for several elements including refractory elements (Y, Zr, and Sc; Fig. 2.18) and some potential volatile metals (e.g., Cu, Zn; Fig. 2.19). The refractory element scatter is easily explained by the mixing described above. Y, Zr, and Sc all are higher in the S-2 component, while Ce is higher in the S-1 component. Mixing will therefore form negative correlations with Ce and create considerable scatter in Ce variation diagrams. Observed semi-volatile trace elements, however, are similar in both endmembers or are

slightly higher in the S-1 component (as are Ba, Rb, and Sr; Fig. 2.17) and still are relatively scattered (Fig. 2.19).

Although these observations might suggest some level of volatility for Cu, Zn, and possibly Pb, other possible mechanisms could generate similar scatter: (1) increased analytical uncertainty associated with semi-volatile elements (e.g., Chapter 2), (2) minor assimilation or contamination of material concentrated with metals such as brines (Kent *et al*., 1999a,b) or hydrothermally altered basalt, and (3) fractionation of a known or cryptic mineral phase. Analytical uncertainty is highly unlikely since elements like Rb have a broadly similar volatility-based fractionation as Cu during LA-ICP-MS (Chapter 2), yet are well-behaved in variation diagrams (Fig. 2.17). Crustal contamination is a good explanation for high Pb values found in a subset of matrix glass and melt inclusions (Fig. 2.19), although these samples do not show anomalous behavior in other highly incompatible elements that are also sensitive to contamination (e.g., Rb, Ba). We thus argue that removal of either olivine (for Zn) or sulfide (for Cu), could potentially explain a large degree of the observed variations.

Low Cu concentrations could be achieved by very small amounts of crystallization of a Cu-bearing phase. Previous analyses of sulfides from Kilauea Iki (Stone and Fleet, 1992; Pitcher *et al*., 2010) found evidence for Cu-Ni-Fe sulfides with up to 40 wt. % Cu. Removal of <<1% of such a phase (or alternatively, retention of this phase in the melting source region and/or variable dissolution of the phase during melt evolution and as S degasses) could easily explain all the observed variation Cu values. Sulfide is also the only phase during the Kilauea Iki eruption that may significantly partition Cu. In addition to EMPA and LA-ICP-MS analysis of olivine, spinel, and sulfide samples were examined by Energy Dispersive Spectroscopy (EDS) on a thin section of Iki-22 generously made available by Rosalind Helz (Fig. 2.21). As shown by a representative glass analysis, this method only reveals the approximate atomic proportion of elements present at generally >1 wt. %. Cu peaks were only observed in the sulfides. Although the Cu peak is small, it represents a considerable concentration due to the relatively high molecular weight of Cu. While Cu variation could be explained by cryptic removal of sulfide, Zn variations are easily explained by fractionation of olivine that has

~100 ppm Zn, similar to that of the melt. We therefore would not expect to find a strong increase in Zn with differentiation. Cu, however, requires either volatile fluxing or removal of a Cu-bearing phase.

All of these are alternatives to volatile behavior, however, we cannot preclude that high pressure volatile fluxing of Cu may impart some of the observed scatter. In fact, experimental work has suggested Cu may require higher pressures to efficiently be complexed with S and transported in a vapor phase (Williams *et al*., 1995, Pokrovski *et al*., 2005). In this case, we would not expect to see differences between matrix glass and melt inclusions trapped at shallow levels.

Previous work at Hawaii has argued for volatile loss of Re based on petrologic data, but not for other trace elements that we have examined (Bennett *et al*., 2000; Pitcher *et al*., 2009). Worldwide, however, other studies have argued that some elements (e.g., Cu) do behave volatility (e.g., Collins *et al*., 2009). Instead, during the 1959 eruption of Kilauea Iki it seems most probable that Cu and other semi-volatile metals are controlled by the same mixing and fractionation processes controlling other trace elements, with the exception that Cu may be also partitioned into a sulfide phase that is not apparent in surface eruptive products.

Conclusions

These results clearly confirm previous hypotheses that compositions of the 1959 eruption of Kilauea Iki were controlled by a mixture of olivine + Cr-spinel and late clinopyroxene groundmass crystallization along with mixing between two compositionally-distinct magma batches. Major element compositions are primarily influenced by fractionation processes with the exception of Ca that is enriched in the S-1 endmember (Wright, 1973). The mixing process is much more clearly identified in trace element compositions. Sc, Y, Zr, La, and Hf (±Yb) are clearly enriched in the S-2 component and Rb, Ba, and Ce (± Cu, and Zn) are clearly enriched in the S-1 component. Sr and Nb are indistinguishable between the two components, as well as La/Yb ratios. Although these trace element differences can be partially explained by degree of partial melting of a garnet-bearing source, the most likely explanation is that the two magma

batches originate from heterogeneous sources. Mixing between these two endmembers coupled with olivine fractionation explains all other variation in most trace elements.

None of the trace metals analyzed exhibit any signs of clear degassing between pre-eruptive melt inclusions and highly degassed matrix glass. In previous studies of Hawaii, Re is the only trace metal with petrologic evidence for degassing (Bennett *et al*., 2000; Pitcher *et al*., 2009). The data presented here support broadly incompatible behavior with some evidence for compatibility in major (Co and Zn in olivine) and trace (Cu in sulfide) phases.

Direct observations of submarine eruptions at Loihi seamount and direct gas analysis of recent Kilauean lava flows show evidence for release of many other trace metals including Cu (Rubin, 1998; Hinkley *et al*., 1999). This volatile behavior does not appear to be obviously preserved in rock compositions. One possibility is that Cu volatility only occurs at higher pressures and therefore is not expressed as differences between matrix glass and melt inclusions, which record eruptive degassing at shallow pressures (Williams *et al*., 1995). If this is the case, subtle variability in glass compositions could be below the resolution of our current analytical uncertainty. To further investigate this process, more detailed analysis of the sulfide phases will be necessary in order to clearly constrain the effect of sulfide saturation and mixing on each trace metal analyzed.

References

Anderson Jr, A., and Brown, G., 1993, CO 2 contents and formation pressures of some Kilauean melt inclusions, American Mineralogist, v. 78, p. 794-803.

Asimow P.D., Ghiorso MS, 1998, Algorithmic Modifications Extending MELTS to Calculate Subsolidus Phase Relations, American Mineralogist, v. 83, p. 1127-1131.

Ault, W., Eaton, J.P., and Richter, D.H., 1961, Lava temperatures in the 1959 Kilauea eruption and cooling lake, Geological Society of America Bulletin, v. 72, p. 791-794.

Baker, D., 2008, The fidelity of melt inclusions as records of melt composition, Contributions to Mineralogy and Petrology, v. 156, p. 377-395.

Bennett, V.C., Norman, M.D., and Garcia, M.O., 2000, Rhenium and platinum group element abundances correlated with mantle source components in Hawaiian picrites: sulphides in the plume, Earth and Planetary Science Letters, v. 183, p. 513-526.

Blundy, J.D., and Cashman, K.V., 2005, Rapid decompression-driven crystallization recorded by melt inclusions from Mount St. Helens volcano, Geology, v. 33, p. 793-796.

Candela, P.A., and Holland, H.D., 1986, A mass transfer model for copper and molybdenum in magmatic hydrothermal systems; the origin of porphyry-type ore deposits, Economic Geology, v. 8, p. 1-19.

Clague, D.A., Moore, J.G., Dixon, J.E., and Friesen, W.B., 1995, Petrology of submarine lavas from Kilauea's Puna Ridge, Hawaii, Journal of Petrology, v. 36, p. 299-349.

Clague, D.A., Weber, W.S., and Dixon, J.E., 1991, Picritic glasses from Hawaii, Nature, v. 353, p. 553-556.

Collins, S.J., Pyle, D.M., and Maclennan, J., 2009, Melt inclusions track pre-eruption storage and dehydration of magmas at Etna, Geology, v. 37, p. 571-574.

Cottrell, E., Spiegelman, M., and Langmuir, C.H., 2002, Consequences of diffusive reequilibration for the interpretation of melt inclusions, Geochemistry Geophysics Geosystems, v. 3, 26 p.

Danyushevsky, L.V., Della-Pasqua, F.N., and Sokolov, S., 2000, Re-equilibration of melt inclusions trapped by magnesian olivine phenocrysts from subduction-related magmas: petrological implications, Contribution to Mineralogy and Petrology, v. 138, p. 68-83.

Danyushevsky, L.V., McNeill, A., and Sobolev, A., 2002, Experimental and petrological studies of melt inclusions in phenocrysts from mantle-derived magmas: an overview of techniques, advantages and complications, Chemical Geology, v. 183, p. 5-24.

Eaton, J., and Murata, K., 1960, How volcanoes grow, Science, v. 132, p. 925-938.

Faure, F., and Schiano, P., 2005, Experimental investigation of equilibration conditions during forsterite growth and melt inclusion formation, Earth and Planetary Science Letters, v. 236, p. 882-898.

Gaetani, G.A., and Watson, E.B., 2002, Modeling the major-element evolution of olivine-hosted melt inclusions, Chemical Geology, v. 183, p. 25-41.

Gerlach, T.M., 1986, Exsolution of H2O, CO2, and S During Eruptive Episodes at Kilauea Volcano, Hawaii, Journal of Geophysical Research, v. 91, p. 12177-12185.

Ghiorso, M.S., and Sack, R.O., 1995, Chemical Mass Transfer in Magmatic Processes. IV. A Revised and Internally Consistent Thermodynamic Model for the Interpolation and Extrapolation of Liquid-Solid Equilibria in Magmatic Systems at Elevated Temperatures and Pressures, Contributions to Mineralogy and Petrology, v. 119, p. 197-212.

Helz, R.T., 1987, Diverse olivine types in lava of the 1959 eruption of Kilauea Volcano and their bearing on eruption dynamics, US Geological Survey Professional Paper, v. 1350, p. 691-722.

Hinkley, T., Lamothe, P., Wilson, S.A., Finnegan, D., and Gerlach, T., 1999, Metal emissions from Kilauea, and a suggested revision of the estimated worldwide metal output by quiescent degassing of volcanoes, Earth and Planetary Science Letters, v. 170, p. 315-325.

Holland, H.D., 1972, Granites, solutions, and base metal deposits, Economic Geology, v. 67, p. 281-301.

Kent, A.J.R., 2008, Melt inclusions in basaltic and related volcanic rocks, Reviews in Mineralogy and Geochemistry, v. 69, p. 273-331.

Kent, A.J.R., Clague, D.A., Honda, M., Stolper, E.M., Hutcheon, I.D., and Norman, M.D., 1999, Widespread assimilation of a seawater-derived component at Loihi Seamount, Hawaii, Geochimica et Cosmochimica Acta, v. 63, p. 2749–2761.

Kent, A.J.R., Norman, M.D., Hutcheon, I.D., and Stolper, E.M., 1999, Assimilation of seawater-derived components in an oceanic volcano: evidence from matrix glasses and glass inclusions from Loihi seamount, Hawaii, Chemical Geology, v.156, p. 299-319.

Kohut, E., and Nielsen, R.L., 2004, Melt inclusion formation mechanisms and compositional effects in high-An feldspar and high-Fo olivine in anhydrous mafic silicate liquids, Contributions to Mineralogy and Petrology, v. 147, p. 684-704.

Lu, F., Anderson Jr, A., and Davis, A., 1995, Diffusional gradients at the crystal/melt interface and their effect on the compositions of melt inclusions, The Journal of Geology, v. 103, p. 591-597.

Mathez, E., 1976, Sulfur solubility and magmatic sulfides in submarine basalt glass, Journal of Geophysical Research, v. 81, p. 4269-4276.

McDonough, W.F., and Sun, S., 1995, The composition of the Earth, Chemical Geology, v. 120, p. 223-253.

Milman-Barris, M.S., Beckett, J.R., Baker, M.B., Hofmann, A.E., Morgan, Z., Crowley, M.R., Vielzeuf, D., and Stolpher, E.M., 2008, Zoning of phosphorous in igneous olivine, Contributions to Mineralogy and Petrology, v. 155, p. 739-765.

Murata, K., and Richter, D.H., 1966a, Chemistry of the Lavas of the 1959-60 Eruption of Kilauea Volcano, Hawaii, US Geological Survey Professional Paper, v. 537-A, p. 1-26.

Murata, K., and Richter, D.H., 1966b, The settling of olivine in Kilauean magma as shown by lavas of the 1959 eruption, American Journal of Science, v. 264, p. 194-203.

Nielsen, R.L., Michael, P.J., and Sours-Page, R., 1998, Chemical and physical indicators of compromised melt inclusions, Geochimica et Cosmochimica Acta, v. 62, p. 831-839.

Norman, M.D., Garcia, M.O., and Bennett, V.C., 2004, Rhenium and chalcophile elements in basaltic glasses from Ko'olau and Moloka'i volcanoes: Magmatic outgassing and composition of the Hawaiian plume, Geochimica et Cosmochimica Acta, v. 68, p. 3761-3777.

Pitcher, L., Helz, R.T., Walker, R.J., and Piccoli, P.M., 2009, Fractionation of the platinum-group elements and Re during crystallization of basalt in Kilauea Iki Lava Lake, Hawaii, Chemical Geology, v. 260, p. 196-210.

Pokrovski, G.S., Roux, J., and Harrichoury, J.C., 2005, Fluid density control on vapor-liquid partitioning of metals in hydrothermal systems, Geology, v. 33, p. 657-660.

Putirka, K., Perfit, M., Ryerson, F., and Jackson, M., 2007, Ambient and excess mantle temperatures, olivine thermometry, and active vs. passive upwelling, Chemical Geology, v. 241, p. 177-206.

Richter, D.H., and Murata, K., 1966, Petrography of the Lavas of the 1959-60 Eruption of Kilauea Volcano, Hawaii, US Geological Survey Professional Paper, v. 537-D, p. 1-12.

Richter, D.H., Eaton, J.P., Murata, K., Ault, W., and Krivoy, H.L., 1970, Chronological Narrative of the 1959-60 Eruption of Kilauea Volcano, Hawaii, US Geological Survey Professional Paper, v. 537-E, p. 1-73.

Roedder, E., 1979, Origin and significance of magmatic inlcuions, Bulletin of Mineralogy, v. 102, p. 487-510.

Roedder, E., 1984, Fluid Inclusions, Reviews in Mineralogy, v. 12, p. 1-644.

Rubin, K., 1997, Degassing of metals and metalloids from erupting seamount and mid-ocean ridge volcanoes: Observations and predictions, Geochimica et Cosmochimica Acta, v. 61, p. 3525-3542.

Schiano, P., 2003, Primitive mantle magmas recorded as silicate melt inclusions in igneous minerals, Earth Science Reviews, v. 63, p. 121-144.

Simon, A., Pettke, T., Candela, P.A., Piccoli, P.M., and Heinrich, C.A., 2006, Copper partitioning in a melt-vapor-brine-magnetite-pyrrhotite assemblage, Geochimica et Cosmochimica Acta, v. 70, p. 5583-5600.

Sinton, C.W., and Duncan, R.A., 1997, Potential links between ocean plateau volcanism and global ocean anoxia at the Cenomanian-Turonian boundary, Economic Geology, v. 92, p. 836-842.

Stone, W.B., and Fleet, M.E., 1991, Nickel-copper sulfides from the 1959 eruption of Kilauea Volcano, Hawaii: Contrasting compositions and phase relations in eruption pumice and Kilauea Iki lava lake, American Mineralogist, v. 76, p. 1363-1372.

Sun, W., Bennett, V.C., Eggins, S., Arculus, R., and Perfit, M., 2003, Rhenium systematics in submarine MORB and back-arc basin glasses: laser ablation ICP-MS results, Chemical Geology, v. 196, p. 259-281.

Tilling, R.I., Wright, T.L., and Millard, H.T., 1987, Trace-element chemistry of Kilauea and Mauna Loa lava in space and time: A reconnaissance, US Geological Survey Professional Paper, v. 1350, p. 641-689.

Wallace, P.J., and Anderson Jr, A., 1998, Effects of eruption and lava drainback on the H 2 O contents of basaltic magmas at Kilauea Volcano, Bulletin of Volcanology, v. 59, p. 327-344.

Wallace, P.J., and Carmichael, I., 1992, Sulfur in basaltic magmas, Geochimica et Cosmochimica Acta, v. 56, p. 1863-1874.

Williams, T.J., Candela, P.A., and Piccoli, P.M., 1995, The partitioning of copper between silicate melts and two-phase aqueous fluids: an experimental investigation at 1 kbar, 800 C and 0.5 kbar, 850 C, Contributions to Mineralogy and Petrology, v. 121, p. 388-399.

Winter, J.D., 2001, An Introduction to Igneous and Metamorphic Petrology. Prentice-Hall Inc, Upper Saddle River, New Jersey, 697.

Witt-Eickschen, G., Palme, H., O'Neill, H.S.C., and Allen, C.M., 2009, The geochemistry of the volatile trace elements As, Cd, Ga, In and Sn in the Earth's mantle: New evidence from in situ analyses of mantle xenoliths, Geochimica et Cosmochimica Acta, v. 73, p. 1755-1778.

Wright, T.L., 1973, Magma mixing as illustrated by the 1959 eruption, Kilauea volcano, Hawaii, Geological Society of America Bulletin, v. 84, p. 849-858.

Wright, T.L., and Fiske, R.S., 1971, Origin of the differentiated and hybrid lavas of Kilauea volcano, Hawaii, Journal of Petrology, v. 12, p. 1-65.

Zajacz, Z., and Halter, W., 2009, Copper transport by high temperature, sulfur-rich magmatic vapor: Evidence from silicate melt and vapor inclusions in a basaltic andesite from the Villarrica volcano (Chile), Earth and Planetary Science Letters, v. 282, p. 115-121.

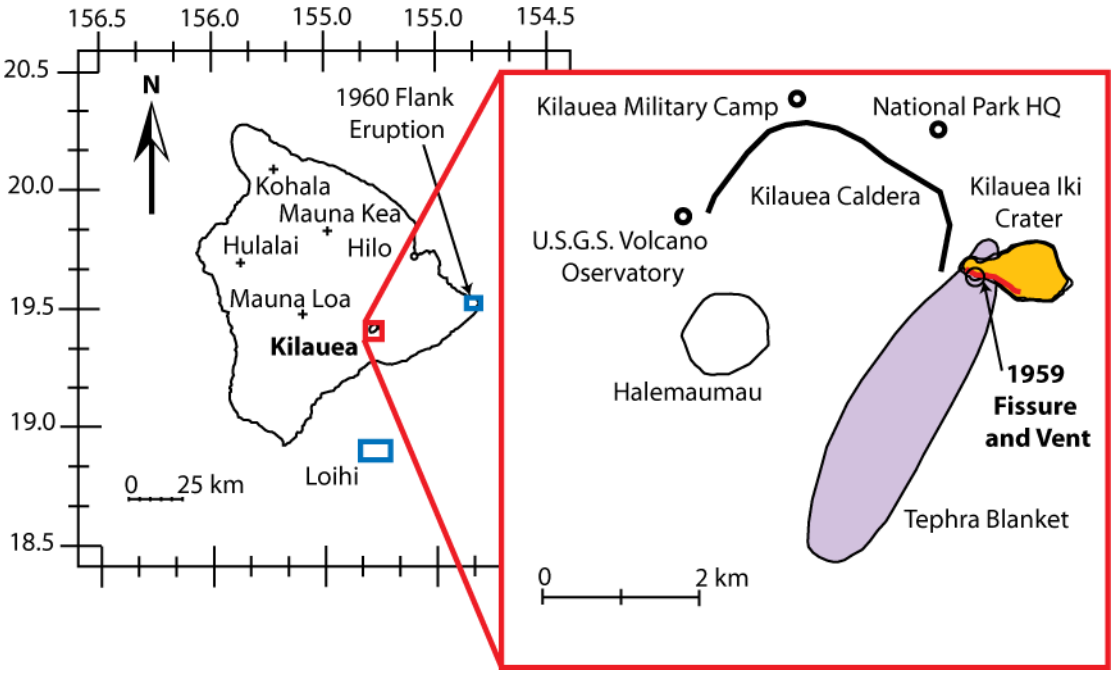

Figure 2.1. Location of Kilauea Iki on the Big Island of Hawaii. The 1959 summit eruption began as a fissure (red line) and converged to a single vent (black circle) eventually filling much of the Kilauea Iki Crater (yellow). High fire fountains spread an unusually large tephra deposit (extent shown in purple) for Hawaiian eruptions. Figure modified from Richter *et al*. (1970).

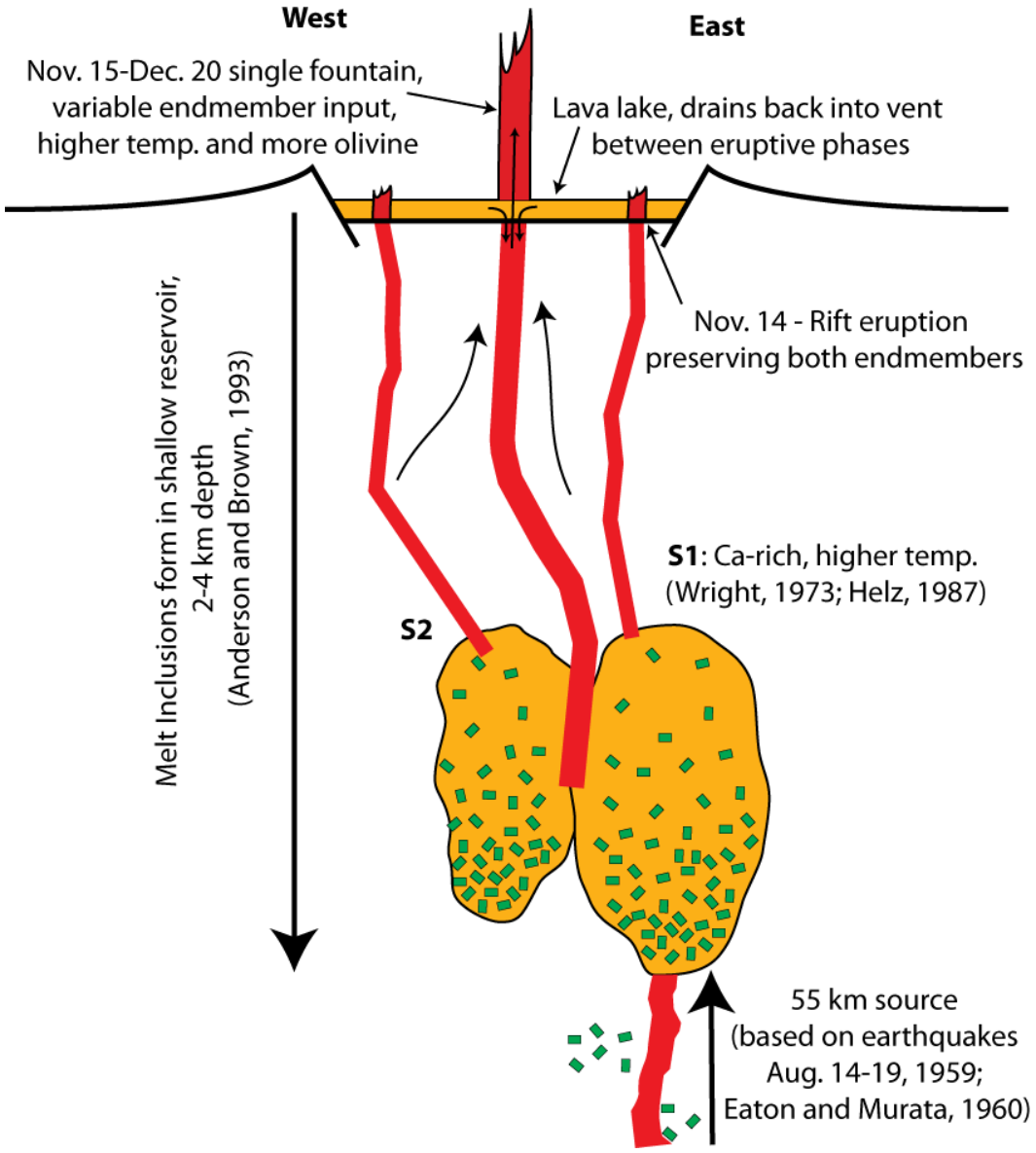

Figure 2.2. Conceptual cross section of the 1959 eruption of Kilauea Iki synthesized from all previous studies. Earthquakes from Aug. 14-19 preceded the eruption suggesting generation of magma from 55 km depth (Eaton and Murata, 1960). The eruption began on Nov. 14 along a 750 m fissure before condensing to a single fire fountain with heights reaching up to 500 m (Richter 1970). In total, 17 eruptive phases occurred through Dec. 20 filling a lava lake 125 m deep, partially cycling back erupted lava into the vent between each phase. Wright (1973) identified mixing of two endmembers ("S-1" and "S-2" which were best preserved the first day of the eruption (S-1 to the East, S-2 to the West) and variably mixed over the following month. Helz (1987) examined olivine compositions and proposed that the S-1 endmember was from a deeper source and mixed with a shallow stored, cooler endmember as well as carrying some kink-deformed xenocrystic olivines. Most melt inclusions were trapped at pressure consistent with a 2-4 km magma chamber depth (Anderson and Brown 1973).

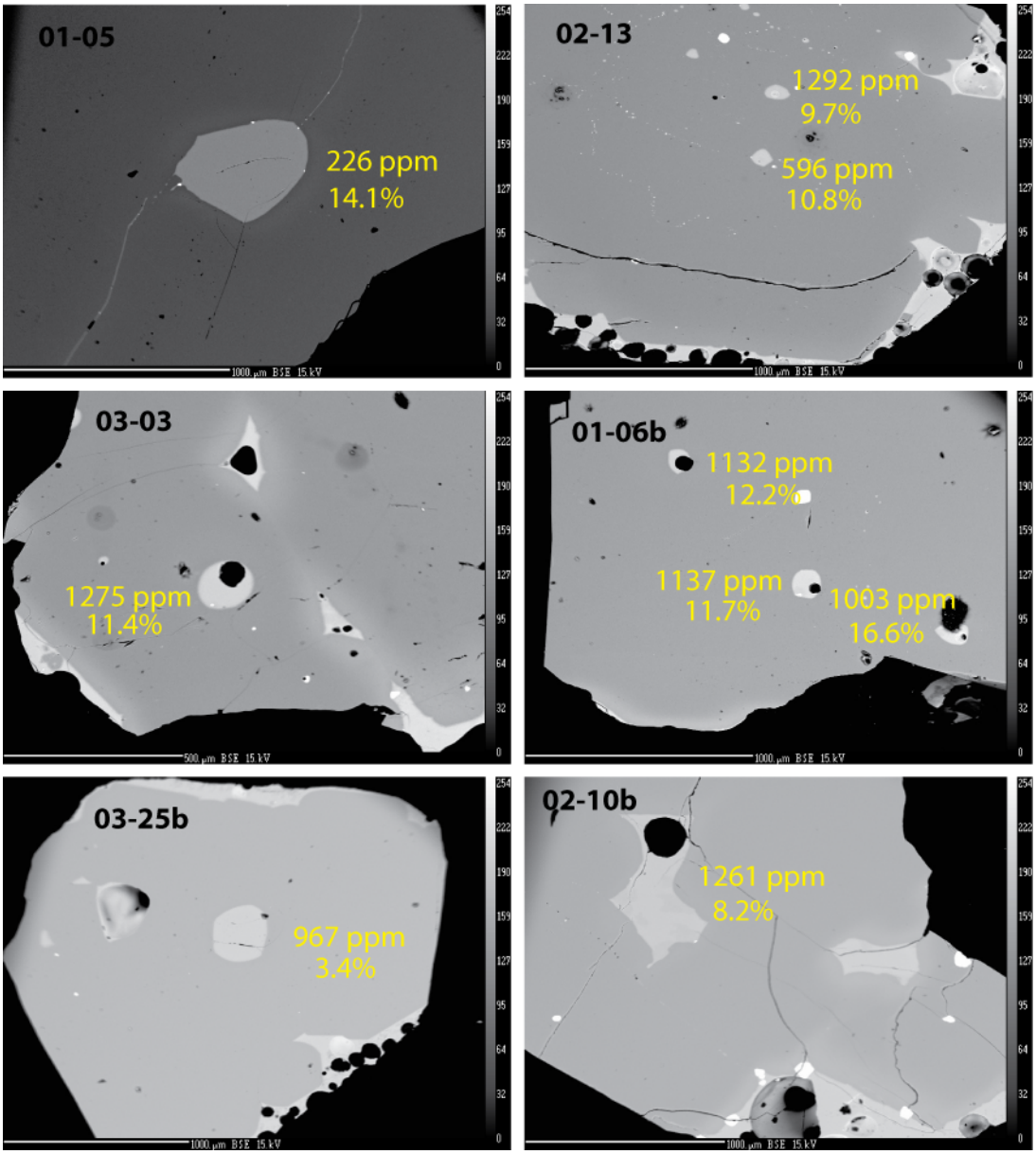

Figure 2.3. Selected BSE images of olivine-hosted melt inclusions from Kilauea Iki. Visible are a range of inclusion morphologies including breached olivines (01-05) and those with vapor bubbles and/or chromite inclusions exposed (03-03, 01-06b, 02-10b). Also shown are measured sulfur contents and percent crystallization estimated by correction for post entrapment crystallization. Note lighter rims (Fa-rich) on some inclusions (01-05) and what may be growth bands within the olivine rich in inclusions (02-13).

Table 2.1. Long-term accuracy of EMPA calibration and secondary standards.

	SiO2	TiO2	Al2O3	Cr2O3	FeO*	MnO	MgO	CaO	Na2O	K2O	P2O5	Total
BASL												
Value	50.94	4.06	12.94		13.49	0.15	5.08	9.3	2.66	0.84	0.38	99.84
Uncertainty												
Measured (n=15)	50.90	4.12	12.54		13.16	0.19	5.11	9.41	2.43	0.81	0.46	99.27
Std Dev	0.65	0.10	0.18		0.15	0.04	0.03	0.07	0.49	0.04	0.02	
Accuracy (avg/accepted %)	**99.9**	**101.5**	**96.9**		**97.6**	**126.5**	**100.6**	**101.2**	**91.4**	**96.8**	**119.9**	
BCR-2G												
Value	54.40	2.27	13.40	0.005	12.40	0.19	3.56	7.06	3.23	1.74	0.37	98.62
Uncertainty	0.40	0.04	0.40	0.001	0.30	0.01	0.09	0.11	0.07	0.04	0.01	
Measured (n=3)	54.64	2.40	14.11	0.006	12.43	0.19	3.59	7.31	2.82	1.71	0.37	99.57
Std Dev	0.04	0.03	0.07	0.034	0.08	0.03	0.01	0.04	0.09	0.04	0.01	
Accuracy (avg/accepted %)	**100.4**	**105.8**	**105.3**	**123.4**	**100.2**	**99.6**	**100.9**	**103.5**	**87.2**	**98.1**	**100.9**	
BHVO-2G												
Value	49.30	2.79	13.60	0.086	11.30	0.17	7.13	11.40	2.40	0.51	0.29	98.98
Uncertainty	0.10	0.02	0.10	0.004	0.10	0.03	0.02	0.10	0.10	0.02	0.02	
Measured (n=3)	50.54	2.85	14.03	0.044	10.99	0.13	7.21	11.58	2.16	0.52	0.29	100.33
Std Dev	0.16	0.02	0.04	0.011	0.08	0.01	0.04	0.02	0.03	0.02	0.01	
Accuracy (avg/accepted %)	**102.5**	**102.1**	**103.1**	**51.5**	**97.3**	**77.2**	**101.1**	**101.6**	**89.9**	**101.8**	**99.3**	
BIR-1G												
Value	47.50	1.04	15.50	0.115	10.40	0.19	9.40	13.30	1.85	0.03	0.03	99.35
Uncertainty	0.30	0.07	0.20	0.007	0.10	0.01	0.10	0.20	0.07	0.01	0.00	
Measured (n=3)	48.00	0.97	15.92	0.053	10.20	0.15	9.43	13.46	1.77	0.05	0.03	100.04
Std Dev	0.15	0.01	0.10	0.039	0.09	0.03	0.06	0.01	0.06	0.01	0.01	
Accuracy (avg/accepted %)	**101.1**	**93.7**	**102.7**	**46.0**	**98.1**	**80.7**	**100.3**	**101.2**	**95.7**	**150.4**	**107.2**	

Table 2.2. Analyzed masses and approximate measured concentrations.

Isotope	Melt Inclusions		Glass	Glass	Melt Inclusions	Olivine
	5/21/09	12/14/09	10/13/10	(ppm)	(ppm)	(ppm)
7Li			x	5.0		
11B	x	x	x	2.9	2.5	1.0
25Mg		x	x			
29Si	x					
43Ca	x	x	x			
45Sc	x	x	x	32	30	6.4
47Ti	x	x	x			70
51V	x	x	x	377	337	7.6
52Cr		x	x	431	481	
59Co		x	x	53	45	
60Ni			x	178		
63Cu		x		145	101	6.1
65Cu	x	x	x			
64Zn		x		135	120	100
66Zn	x	x	x			
75As			x	0.9		
85Rb	x	x	x	11	8.3	
88Sr	x	x	x	391	360	0.03
89Y	x	x	x	21	18	0.10
90Zr	x	x	x	144	124	0.07
93Nb			x	17		
98Mo	x	x	x	1.1	1.1	0.85
107Ag	x				0.05	
111Cd	x			0.25	0.21	0.06
112Cd		x	x			
115In	x		x	0.11	0.08	0.00
118Sn	x	x	x	1.6	1.5	0.37
121Sb	x		x	0.13	0.06	0.03
133Cs			x	0.15		
137Ba		x	x	150	123	
138Ba	x					
139La			x	15		
140Ce	x	x	x	41	34	
141Pr			x	5.1		
146Nd			x	23		
147Sm			x	5.7		
153Eu			x	1.9		
157Gd			x	5.3		
163Dy			x	4.4		
166Er			x	2.2		
172Yb			x	1.7		
178Hf			x	3.5		
182W	x	x	x	0.25	0.21	
205Tl		x	x	0.02	0.02	
208Pb	x	x	x	1.4	1.1	
209Bi	x				0.03	
232Th			x	1.1		
238U	x		x	0.41	0.37	

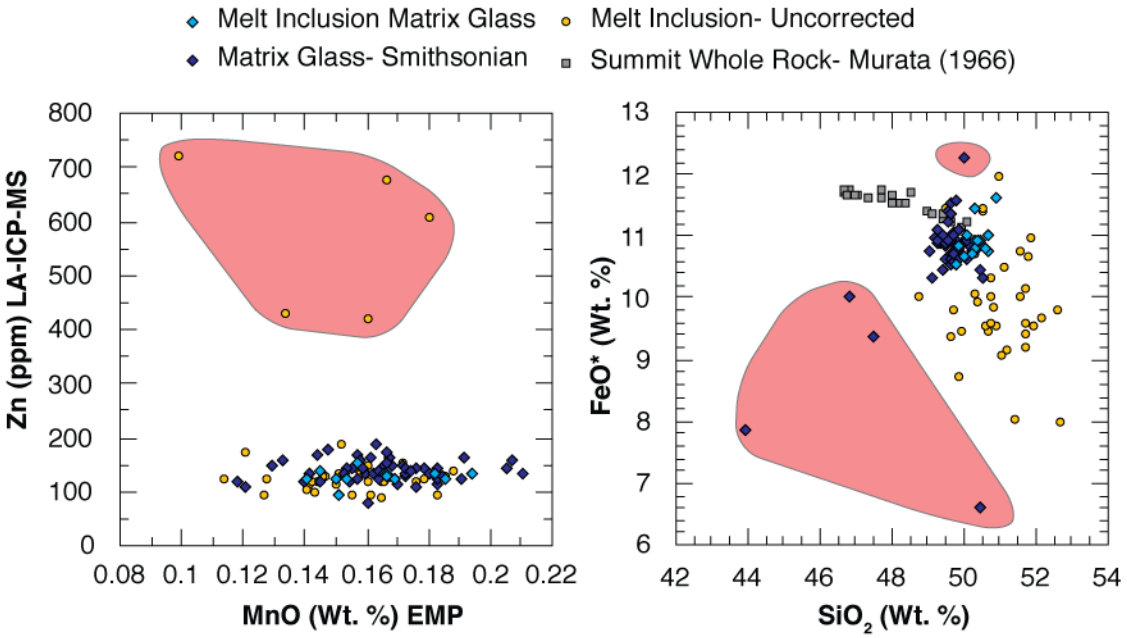

Figure 2.4. Illustration of two strategies used to ensure data quality. Shaded regions highlight rejected data. Zn and Mn are similarly compatible in olivine but are measured using both EMPA (Mn) and LA-ICP-MS (Zn). Anomalously high Zn values are the result of accidental incorporation of olivine during laser ablation. Five glass analyses have unusually high or low FeO* values that could be due to EMPA analysis near or on Cr-spinel or olivine.

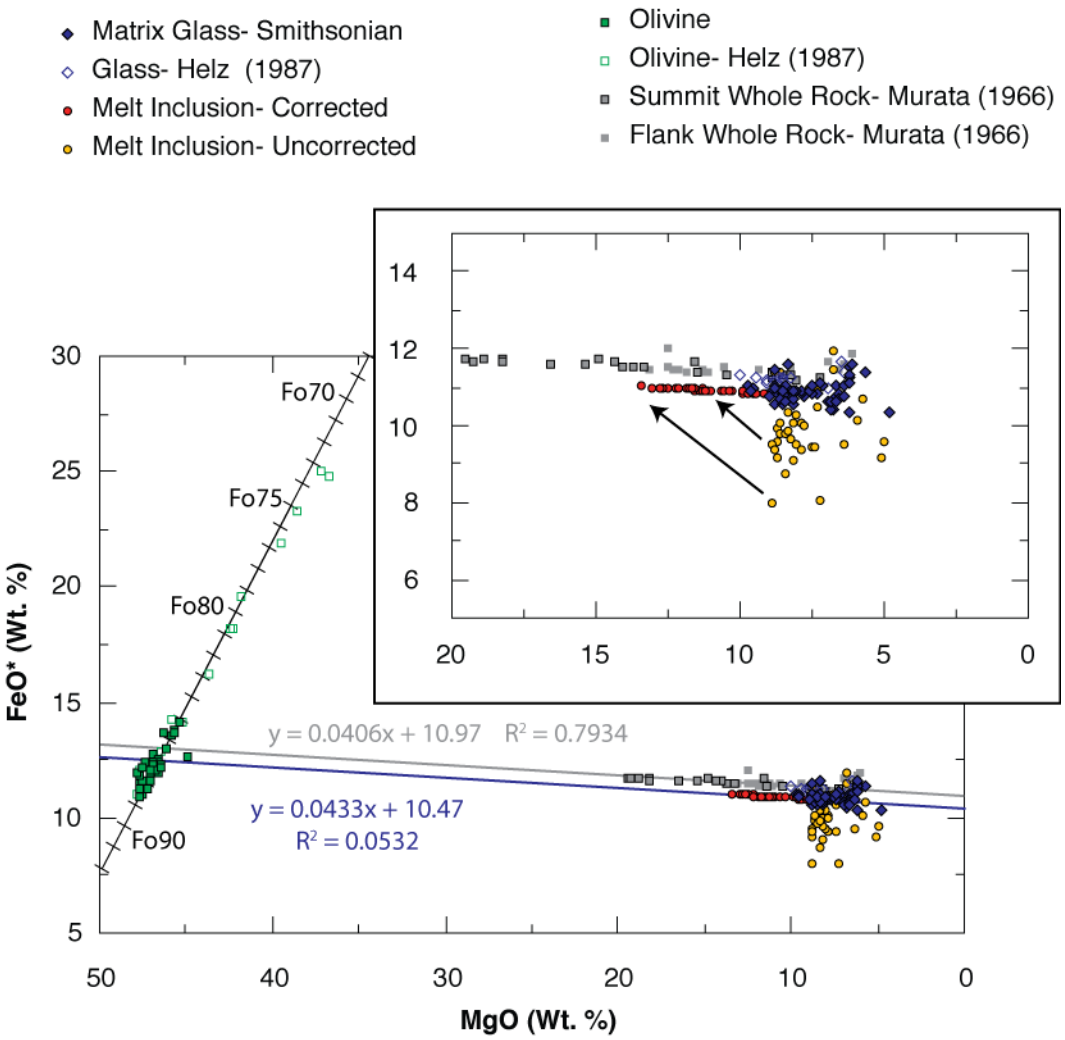

Figure 2.5. Corrections of melt inclusions for post-entrapment crystallization (PEC) and diffusive Fe-loss. Glass and whole rock compositions all lie along a relatively restricted compositional control line. Our glass and olivine FeO* values measured by EMPA are consistently offset from previous work by ~0.5 wt.% suggesting a difference in calibration between the two data sets. For internal consistency, we correct all values relative to our analyses. The slope of Fe evolution calculated with a linear regression of either whole rock values or our glass values (including only compositions >7 wt. % MgO to avoid samples affected by cpx fractionation) are similar (m=0.043-0.041) and projects to Fo88 consistent with the composition of host olivines. All melt inclusions have been iteratively corrected to this control line using the olivine-melt geothermometer of Putirka *et al*. (2007) requiring a median PEC correction of 10% by weight.

Table 2.3. Constants and parameters used in melt inclusion correction equations.

Equation Constants[a]

	a	b	c	d	e	f
Eqn 1 Mg	2.158	55.09	6.213E-02	4430	5.115E-02	N/A
Eqn 2 Fe	3.3	47.57	5.192E-02	3344	5.595E-02	1.633E-02

Melt Evolution Control Line

[FeO*]=m*[MgO]+b	
m=[b]	0.0433
b=[b]	10.47055
FeO*/FeO=[c]	1.13

Physical Conditions

Pressure (GPa)[d]	0.1
H_2O (wt.%)[d]	0.5

Calculated Temperature (deg. C)

Mean=	1272
Range=	1210-1327

[a]Olivine-Melt thermometer from Putirka *et al*. (2007)
[b]Slope and intercept calculated from a linear regression of glass analyses in this study.
[c]FeO*/FeO calculated from wet chemical analyses of Murata and Richter (1966)
[d]Pressure and water contents within the range defined by melt inclusions for Anderson and Brown (1993)

Table 2.4. Matrix glass major element concentrations (wt. %) by EMPA.

Sample	01-02	01-11	06-01	06-02	06-08	06-09	07-01
Alias 1							
Alias 2							
Source	AK*	AK	AK	AK	AK	AK	AK
Day (fr. Nov 14)							
SiO_2	50.32	50.87	50.04	50.54	50.67	49.86	50.48
TiO_2	2.73	2.77	2.93	2.93	2.99	2.93	2.82
Al_2O_3	12.98	13.15	13.25	13.47	13.49	13.45	13.15
Cr_2O_3	0.05	0.07	0.06	0.06	0.06	0.03	0.06
FeO*	11.46	11.63	10.65	10.85	10.75	10.82	10.91
MnO	0.18	0.15	0.15	0.16	0.19	0.17	0.17
MgO	8.78	8.34	8.22	7.75	7.74	7.87	8.72
CaO	11.74	12.05	11.84	11.78	11.78	11.80	11.71
Na_2O	2.10	2.08	2.22	2.27	2.23	2.23	2.19
K_2O	0.53	0.53	0.53	0.55	0.60	0.57	0.54
P_2O_5	0.27	0.29	0.28	0.30	0.30	0.28	0.28
S	0.010	0.016	0.016	0.018	0.013	0.014	0.013
Cl	0.016	0.017	0.017	0.019	0.020	0.019	0.017
F	0.019	0.017	0.028	0.039	0.012	0.036	0.044
NiO	0.03	0.03	0.01	0.01	0.02	0.02	0.01
Total	101.22	101.99	100.26	100.76	100.86	100.09	101.11

*Collected by Adam Kent from late scoria deposits.

Sample	07-02	07-03	07-04	07-05	07-06	07-07	07-08
Alias 1							
Alias 2							
Source	AK	AK	AK	AK	AK	AK	AK
Day (fr. Nov 14)							
SiO_2	50.64	50.32	50.37	50.11	49.81	50.57	50.32
TiO_2	2.97	2.93	2.94	2.87	2.88	2.98	2.94
Al_2O_3	13.77	13.40	13.45	13.02	13.05	13.69	13.61
Cr_2O_3	0.02	0.07	0.04	0.05	0.06	0.04	0.05
FeO*	11.02	10.92	10.92	11.02	10.56	10.81	10.80
MnO	0.19	0.15	0.17	0.17	0.15	0.18	0.15
MgO	7.13	7.83	8.05	8.77	8.83	7.28	7.47
CaO	11.77	11.76	11.77	11.71	11.69	11.87	11.86
Na_2O	2.35	2.24	2.25	2.16	2.12	2.29	2.23
K_2O	0.62	0.57	0.58	0.50	0.54	0.58	0.59
P_2O_5	0.28	0.27	0.28	0.28	0.27	0.29	0.29
S	0.014	0.014	0.007	0.016	0.013	0.016	0.023
Cl	0.019	0.032	0.018	0.018	0.018	0.019	0.020
F	0.034	0.036	0.030	0.027	0.029	0.010	0.030
NiO	0.00	0.02	0.03	0.03	0.01	0.01	0.02
Total	100.82	100.56	100.89	100.75	100.04	100.64	100.39

Table 2.4. (continued)

Sample	07-09	01	02	03	04	05	07
Alias 1		Iki-01	Iki-02	Iki-03	Iki-04	Iki-05	Iki-07
Alias 2		s-2	s-4			s-8	s-9
Source	AK	USGS*	USGS	USGS	USGS	USGS	USGS
Day (fr. Nov 14)		1	4	6	6	8	8
SiO_2	50.22	49.55	49.79	49.34	49.38	49.98	49.68
TiO_2	2.93	3.11	2.71	2.58	2.59	2.86	2.73
Al_2O_3	13.28	14.64	13.00	12.47	12.46	13.47	13.21
Cr_2O_3	0.06	0.04	0.07	0.08	0.08	0.04	0.07
FeO*	10.73	11.38	10.82	11.02	10.99	10.92	11.00
MnO	0.14	0.13	0.16	0.18	0.15	0.18	0.13
MgO	8.28	5.67	8.21	9.72	9.57	7.57	8.33
CaO	11.74	10.84	11.55	11.26	11.17	11.36	11.17
Na_2O	2.08	2.50	2.11	2.01	2.02	2.31	2.17
K_2O	0.54	0.65	0.50	0.48	0.49	0.55	0.50
P_2O_5	0.29	0.35	0.26	0.26	0.27	0.29	0.28
S	0.012	0.066	0.014	0.015	0.012	0.015	0.014
Cl	0.016	0.020	0.018	0.013	0.014	0.015	0.018
F	0.030	0.053	0.038	0.034	0.037	0.011	0.013
NiO	0.02	0.00	0.02	0.03	0.03	0.01	0.01
Total	100.36	99.00	99.28	99.48	99.27	99.58	99.34

*Collected by USGS staff in 1959 and provided by the Smithsonian institution. All sample numbers should be preceded by “NMNH 116111-”.

Sample	08	09	10	11	12	13	15
Alias 1	Iki-08	Iki-09	Iki-10	Iki-11	Iki-12	Iki-13	Iki-15
Alias 2	s-10	s-12	s-13	s-11	s-14**	s-15	s-17
Source	USGS	USGS	USGS	USGS	USGS	USGS	USGS
Day (fr. Nov 14)	13	15	16	13	21	22	24
SiO_2	50.35	49.74	49.88	49.81	49.60	49.31	49.62
TiO_2	2.90	2.94	2.91	2.78	3.05	2.73	2.80
Al_2O_3	13.97	13.83	13.60	13.17	13.76	12.90	13.22
Cr_2O_3	0.03	0.04	0.04	0.06	0.00	0.07	0.04
FeO*	10.80	11.04	11.09	10.94	11.03	10.90	10.92
MnO	0.21	0.16	0.18	0.16	0.17	0.17	0.17
MgO	6.64	6.71	7.24	8.37	6.44	8.85	8.04
CaO	11.62	11.57	11.49	11.26	11.20	11.31	11.46
Na_2O	2.33	2.37	2.29	2.19	2.37	2.14	2.21
K_2O	0.52	0.59	0.56	0.57	0.60	0.52	0.51
P_2O_5	0.29	0.30	0.30	0.29	0.31	0.28	0.30
S	0.010	0.012	0.014	0.015	0.005	0.013	0.017
Cl	0.016	0.020	0.017	0.016	0.021	0.017	0.017
F	0.005	0.041	0.033	0.015	0.018	0.016	0.023
NiO	0.00	0.01	0.02	0.01	-0.01	0.01	0.02
Total	99.71	99.36	99.66	99.66	98.57	99.24	99.35

Table 2.4. (continued)

Sample	16	17	18	19	21	24	25
Alias 1	Iki-16	Iki-17	Iki-18	Iki-19	Iki-21	Iki-24	Iki-25
Alias 2				s-18	s-19		
Source	USGS	USGS	USGS	USGS	USGS	USGS	USGS
Day (fr. Nov 14)	21	24	25	25	28	30	31
SiO_2	49.63	49.70	49.26	49.67	49.51	49.76	49.68
TiO_2	3.16	2.91	2.69	2.76	2.72	2.69	2.74
Al_2O_3	13.70	13.31	13.01	13.26	12.96	12.89	13.20
Cr_2O_3	0.03	0.04	0.08	0.05	0.07	0.08	0.07
FeO*	11.52	11.02	10.87	10.70	10.87	10.54	10.74
MnO	0.18	0.16	0.14	0.15	0.18	0.18	0.14
MgO	6.25	7.49	8.55	8.19	8.73	8.56	8.29
CaO	11.23	11.18	11.29	11.43	11.28	11.26	11.42
Na_2O	2.39	2.20	2.18	2.16	2.19	2.15	2.21
K_2O	0.66	0.61	0.52	0.53	0.54	0.52	0.51
P_2O_5	0.32	0.29	0.28	0.30	0.27	0.29	0.28
S	0.007	0.012	0.009	0.013	0.010	0.009	0.008
Cl	0.018	0.018	0.012	0.014	0.016	0.015	0.013
F	0.063	0.033	0.041	0.034	0.018	0.038	0.011
NiO	-0.01	0.03	0.01	0.02	0.03	-0.02	0.03
Total	99.15	98.99	98.94	99.30	99.40	98.97	99.36

Sample	26	27	29	30	31	32	33
Alias 1	Iki-26	Iki-27	Iki-29	Iki-30	Iki-31	Iki-32	Iki-33
Alias 2	s-21					s-22	s-24
Source	USGS	USGS	USGS	USGS	USGS	USGS	USGS
Day (fr. Nov 14)	31	32	33	33	25	34	36
SiO_2	49.48	50.23	49.61	49.67	49.18	49.77	49.67
TiO_2	2.72	2.73	2.75	2.78	2.73	2.76	2.73
Al_2O_3	13.04	13.11	13.23	13.24	13.04	13.25	13.08
Cr_2O_3	0.06	0.08	0.07	0.07	0.07	0.05	0.09
FeO*	10.83	10.75	10.72	10.53	10.98	10.69	10.71
MnO	0.15	0.16	0.16	0.17	0.17	0.17	0.17
MgO	8.53	8.44	8.25	8.20	8.78	8.16	8.64
CaO	11.35	11.35	11.45	11.42	11.32	11.52	11.37
Na_2O	2.17	2.18	2.20	2.20	2.15	2.18	2.16
K_2O	0.54	0.52	0.55	0.52	0.51	0.55	0.50
P_2O_5	0.30	0.28	0.28	0.27	0.29	0.27	0.29
S	0.007	0.007	0.012	0.008	0.010	0.008	0.012
Cl	0.013	0.017	0.012	0.015	0.015	0.019	0.014
F	0.025	0.005	0.045	0.028	0.027	0.023	0.037
NiO	0.01	0.04	0.02	0.01	0.03	0.00	0.02
Total	99.22	99.90	99.35	99.11	99.30	99.41	99.48

Table 2.4. (continued)

Sample	34	35	36	38	42	44	47
Alias 1	Iki-34	Iki-35	Iki-36	Iki-38	Iki-42	Iki-44	Iki-47
Alias 2			s-20	s-25**	s-3**	s-7	
Source	USGS	USGS	USGS	USGS	USGS	USGS	USGS
Day (fr. Nov 14)	36	34	30	36	3	7	45
SiO_2	49.47	50.45	49.90	50.17	49.54	49.44	49.10
TiO_2	2.79	2.89	2.87	2.92	2.91	2.75	3.01
Al_2O_3	13.09	13.95	13.99	14.01	13.98	13.24	15.24
Cr_2O_3	0.04	0.03	0.06	0.03	0.01	0.07	0.03
FeO*	10.62	10.44	10.70	10.85	11.23	11.03	10.33
MnO	0.16	0.16	0.13	0.17	0.21	0.16	0.14
MgO	8.39	6.81	6.79	6.58	6.20	8.41	4.84
CaO	11.32	11.81	11.68	11.62	11.14	11.28	10.13
Na_2O	2.18	2.34	2.35	2.32	2.42	2.20	2.70
K_2O	0.55	0.57	0.56	0.58	0.62	0.53	0.64
P_2O_5	0.28	0.30	0.29	0.30	0.31	0.28	0.33
S	0.005	0.006	0.002	0.009	0.011	0.014	0.004
Cl	0.016	0.018	0.016	0.017	0.018	0.012	0.017
F	0.039	0.031	0.040	0.029	0.042	0.045	0.038
NiO	0.04	0.02	-0.01	0.01	0.01	0.02	0.02
Total	98.99	99.81	99.36	99.61	98.65	99.47	96.58

Sample	51	53	55	56	58	60	61
Alias 1	Iki-51	Iki-54	Iki-56	Iki-57	Iki-59	Iki-61	Iki-62
Alias 2	Iki-51*						
Source	USGS	USGS	USGS	USGS	USGS	USGS	USGS
Day (fr. Nov 14)	8	13	5	7	24	22	26
SiO_2	49.66	50.06	49.78	49.27	49.60	50.55	50.07
TiO_2	3.12	2.79	3.05	3.08	2.83	3.16	2.90
Al_2O_3	13.75	13.29	13.84	13.63	13.81	14.03	13.80
Cr_2O_3	0.02	0.08	0.01	0.01	0.05	0.04	0.05
FeO*	11.36	10.92	11.58	11.09	10.63	10.33	10.64
MnO	0.18	0.19	0.21	0.18	0.16	0.16	0.15
MgO	6.25	8.02	6.11	6.19	6.68	6.21	6.92
CaO	11.21	11.57	11.14	11.19	11.69	10.72	11.79
Na_2O	2.45	2.25	2.43	2.36	2.24	2.29	2.36
K_2O	0.61	0.55	0.59	0.60	0.57	0.62	0.56
P_2O_5	0.33	0.30	0.31	0.30	0.29	0.35	0.27
S	0.011	0.009	0.010	0.011	0.004	0.011	0.002
Cl	0.018	0.013	0.018	0.023	0.016	0.016	0.015
F	0.043	0.031	0.014	0.034	0.054	0.029	0.056
NiO	0.01	-0.01	0.02	0.02	0.03	0.01	0.02
Total	99.00	100.06	99.12	97.99	98.66	98.53	99.59

Table 2.4. (continued)

Sample	62	63	64	65	70	72	73
Alias 1	Iki-63	Iki-64	Iki-65	Iki-66	Iki-71	Iki-73	Iki-74
Alias 2							
Source	USGS	USGS	USGS	USGS	USGS	USGS	USGS
Day (fr. Nov 14)	32	4	5	13	6	26	7
SiO_2	49.39	49.74	49.48	49.72	49.30	49.83	49.56
TiO_2	2.87	2.89	2.62	2.87	2.55	2.97	2.77
Al_2O_3	13.68	13.70	12.83	13.91	12.43	14.15	13.18
Cr_2O_3	0.03	0.05	0.06	0.03	0.08	0.05	0.05
FeO*	10.45	10.60	10.90	10.72	10.93	10.79	10.92
MnO	0.19	0.18	0.15	0.17	0.16	0.18	0.17
MgO	6.83	6.88	8.55	6.58	9.63	6.37	8.11
CaO	11.60	11.70	11.50	11.58	11.22	11.46	11.20
Na_2O	2.26	2.29	2.11	2.30	2.09	2.34	2.16
K_2O	0.54	0.55	0.52	0.57	0.50	0.64	0.54
P_2O_5	0.28	0.28	0.27	0.30	0.26	0.30	0.28
S	0.005	0.003	0.015	0.009	0.018	0.003	0.013
Cl	0.012	0.013	0.014	0.017	0.014	0.014	0.014
F	0.026	0.012	0.018	0.026	0.040	0.015	0.020
NiO	-0.02	0.01	0.00	-0.01	0.03	0.02	0.00
Total	98.15	98.92	99.05	98.79	99.27	99.13	98.99

Sample	74	76
Alias 1	Iki-75	Iki-77
Alias 2		
Source	USGS	USGS
Day (fr. Nov 14)	10	32
SiO_2	49.07	49.89
TiO_2	2.62	2.89
Al_2O_3	12.65	13.94
Cr_2O_3	0.09	0.05
FeO*	10.76	10.61
MnO	0.14	0.16
MgO	8.94	6.70
CaO	11.61	11.63
Na_2O	2.08	2.33
K_2O	0.51	0.57
P_2O_5	0.26	0.28
S	0.011	0.002
Cl	0.015	0.013
F	0.034	0.040
NiO	0.04	0.01
Total	98.85	99.11

*All samples sourced by USGS are from the Smithsonian and should be preceded by prefix: NMNH116111.

Table 2.5. Matrix glass trace element concentrations (ppm) by LA-ICP-MS.

Sample	01	02	03	04	05	07	08
Li	3.48	4.37	3.62		2.76	6.51	5.69
B		3.55	2.96	4.25	3.68	3.74	3.37
Sc		34.7	32.6	43.3	31.6	29.9	30.4
V		349.8	337.8	449.2	360.4	360.8	373.9
Cr		438.4	622.5	806.2	330.5	453.8	305.0
Co		53.1	59.9	76.9	50.3	54.1	47.9
Ni	118	174	265		147	202	110
Cu		160	128	170	132	178	163
Zn		132	132	177	142	149	143
As		0.71	0.95	1.11	0.63	1.05	1.51
Rb	7.3	9.4	9.7	12.6	10.5	10.3	11.1
Sr	296	374	362	491	385	387	402
Y	16.3	20.9	20.4	26.7	24.8	19.7	20.6
Zr	106	142	139	184	166	139	144
Nb	12.9	16.0	17.0		17.6	17.2	17.3
Mo		0.98	1.16	1.73	0.54	1.10	1.02
Cd		0.26	0.32	0.43	0.32	0.69	0.19
In		0.13	0.10	0.12	0.09	0.99	0.12
Sn		1.84	1.37	2.00	1.48	1.86	1.63
Sb		0.20	0.11	0.27	0.09	0.18	0.15
Cs	0.07	0.13	0.17		0.34	0.17	0.16
Ba	116	138	136	189	141	147	150
La	11.7	14.1	13.5		16.2	14.8	15.0
Ce	30.6	37.1	35.7	49.6	36.2	40.0	40.6
Pr	3.93	4.81	4.45		4.44	4.86	5.05
Nd	15.7	21.9	21.1		19.4	21.9	22.8
Sm	4.18	5.38	5.87		5.80	4.27	5.75
Eu	1.53	1.87	1.59		1.75	1.78	1.88
Gd	4.41	5.17	4.53		6.60	5.49	4.80
Dy	3.32	4.77	4.10		6.05	4.05	4.08
Er	1.30	2.19	1.93		3.04	1.79	2.47
Yb	1.23	1.49	1.12		1.06	1.90	1.78
Hf	2.73	3.33	3.34		4.43	3.42	3.54
W		0.26	0.23	0.23	0.37	0.31	0.39
Pb		1.26	1.30	1.88	1.40	1.46	1.44
Tl		0.01	0.03	0.02	0.03	0.04	0.06
Th	0.90	1.04	0.94		1.21	1.04	1.18
U	0.30	0.37	0.30		0.40	0.46	0.45

Table 2.5. (continued)

Sample	09	10	11	12	13	15	16
Li	4.28	4.79	4.63	4.25	4.45	4.16	5.84
B	3.53	3.43	2.82	2.78	2.81	4.04	2.24
Sc	33.9	33.1	32.4	30.1	34.8	34.4	41.5
V	390.7	358.2	389.6	351.2	356.2	393.1	350.6
Cr	230.6	239.5	488.6	198.1	590.1	531.3	667.3
Co	50.1	51.4	62.0	44.8	73.0	79.3	44.0
Ni	108	124	188	102	213	179	95
Cu	163	168	149	132	161	150	119
Zn	145	145	135	128	150	165	110
As	1.03	0.73	1.27	0.86	1.25	0.54	0.62
Rb	11.1	10.8	10.2	10.5	10.2	11.2	9.7
Sr	418	415	374	392	371	393	355
Y	23.5	24.0	20.7	20.4	22.0	20.8	24.4
Zr	162	165	149	145	151	143	160
Nb	18.0	18.2	16.8	17.9	16.7	17.3	18.2
Mo	1.06	1.15	0.88	0.88	1.32	0.95	0.99
Cd	0.36	0.25	0.21	0.23	0.10	0.33	0.27
In	0.06	0.11	0.13	0.06	0.10	0.10	0.08
Sn	1.67	1.68	1.63	1.38	2.41	1.76	1.34
Sb	0.23	0.26	0.24	0.19	0.16	0.13	0.11
Cs	0.14	0.15	0.24	0.15	0.20	0.18	0.13
Ba	162	155	143	150	137	152	140
La	16.0	16.6	14.5	15.3	15.3	15.9	17.0
Ce	41.6	39.7	37.7	39.0	35.8	40.9	36.3
Pr	5.17	4.98	4.86	5.24	4.83	5.12	5.39
Nd	25.7	23.8	23.0	23.6	22.7	24.3	25.0
Sm	5.61	5.85	5.74	5.87	6.16	5.90	7.23
Eu	1.97	1.87	1.84	1.82	2.02	1.84	2.03
Gd	5.58	5.72	5.49	5.10	5.54	4.32	6.74
Dy	5.09	5.21	4.64	4.59	4.58	4.56	5.69
Er	2.41	2.62	2.26	2.27	2.21	2.01	2.47
Yb	1.85	1.67	1.92	1.69	1.41	1.75	1.95
Hf	4.29	4.12	3.71	4.04	3.89	3.77	4.86
W	0.23	0.40	0.34	0.23	0.29	0.12	0.29
Pb	1.24	1.23	1.60	1.03	2.44	1.50	1.03
Tl	0.01	0.04		0.04	0.05	0.02	0.03
Th	1.24	1.37	0.96	1.26	1.13	1.11	1.39
U	0.39	0.38	0.36	0.41	0.42	0.45	0.42

Table 2.5. (continued)

Sample	17	18	19	21	24	25	26
Li	5.44	4.01	6.36	3.76	5.02	5.06	3.65
B	2.39	3.44		2.08	3.15	2.87	3.49
Sc	34.6	35.1		36.6	34.9	34.7	34.2
V	306.7	335.0		320.8	351.5	334.6	384.4
Cr	373.0	476.0		468.2	480.2	464.6	609.7
Co	38.2	53.1		50.8	52.6	50.6	57.6
Ni	195	183	176	195	184	222	217
Cu	100	131		126	145	117	152
Zn	78	121		112	135	119	143
As	1.98	1.13		1.47	1.31	0.60	0.80
Rb	9.4	9.3	8.7	9.2	10.0	9.7	11.1
Sr	365	375	380	378	371	379	378
Y	22.9	22.9	24.0	23.9	20.9	21.5	20.3
Zr	150	155	174	160	142	146	138
Nb	15.6	16.7	16.6	16.7	16.6	17.6	16.9
Mo	0.98	1.07		1.44	1.16	0.86	0.75
Cd	0.11	0.18		0.26	0.44	0.08	0.33
In	0.18	0.05		0.11	0.12	0.06	0.10
Sn	1.43	1.62		1.34	2.00	1.01	1.70
Sb	0.11	0.08		0.12	0.18	0.12	0.10
Cs	0.12	0.08		0.11	0.06	0.14	0.17
Ba	128	135	134	138	140	146	147
La	16.1	16.3	16.5	15.4	14.1	15.0	15.0
Ce	33.0	36.0	33.7	36.5	38.3	37.6	38.7
Pr	4.81	5.12	5.01	5.03	4.77	5.40	5.20
Nd	23.6	24.0	25.9	23.0	21.4	23.0	22.8
Sm	6.21	6.71	5.66	5.36	5.02	7.25	5.85
Eu	1.80	1.81	2.06	1.78	1.83	1.79	1.98
Gd	6.09	5.22	5.67	5.75	5.06	5.06	5.19
Dy	4.99	4.86	5.70	5.16	3.69	4.57	4.47
Er	2.47	2.30	2.63	2.60	2.31	2.44	1.97
Yb	1.99	1.67	1.78	2.36	1.67	1.62	1.81
Hf	4.34	4.09	5.17	4.20	3.24	3.38	3.60
W	0.27	0.21		0.25	0.11	0.18	0.30
Pb	2.24	1.19		1.21	1.48	1.02	1.35
Tl		0.02		0.01	0.00	0.02	0.03
Th	1.23	1.11	1.09	1.22	1.02	1.25	1.20
U	0.46	0.42	0.39	0.30	0.37	0.41	0.35

Table 2.5. (continued)

Sample	27	29	30	31	32	33	34
Li	5.25	4.97	5.06	5.36	5.07	5.18	5.67
B	3.69	4.48	4.21	3.59	3.62	2.71	4.85
Sc	31.5	30.0	32.5	31.6	36.9	31.8	31.4
V	399.7	330.5	372.6	349.7	323.8	393.8	355.3
Cr	554.5	443.0	492.1	529.7	443.2	558.9	475.1
Co	60.1	50.7	55.4	57.8	46.5	64.8	57.1
Ni	237	213	203	215	197	211	257
Cu	210	120	148	127	77	158	199
Zn	168	124	174	148	134	146	186
As	1.33	1.14	1.51	1.00	1.14	1.77	0.68
Rb	12.0	10.5	10.7	11.5	9.2	11.6	10.7
Sr	381	382	388	391	375	391	382
Y	19.9	21.0	20.4	19.9	22.0	20.4	20.6
Zr	144	140	143	136	152	137	141
Nb	17.6	17.0	16.7	17.6	18.0	16.2	17.8
Mo	1.47	1.15	0.93	1.21	1.21	1.12	1.39
Cd	0.25	0.47	0.37	0.28	0.31	0.38	0.22
In	0.12		0.08	0.13	0.13	0.03	0.13
Sn	1.47	1.48	1.74	1.96	1.67	1.97	2.08
Sb	0.11	0.22	0.18	0.15	0.09	0.16	0.22
Cs	0.14	0.13	0.17	0.08	0.12	0.12	0.11
Ba	149	146	150	152	140	153	146
La	15.3	14.7	14.7	15.1	15.0	14.4	15.2
Ce	41.6	39.4	40.0	41.4	36.6	41.3	39.0
Pr	4.85	5.14	4.87	4.95	5.11	5.04	4.97
Nd	22.7	22.2	22.2	25.8	23.6	22.4	22.9
Sm	5.27	5.14	5.31	5.51	4.63	4.90	5.06
Eu	1.80	1.87	1.82	1.98	1.93	1.80	1.98
Gd	5.82	5.73	5.35	4.62	5.52	5.30	5.43
Dy	4.40	4.34	4.60	4.30	4.26	4.20	4.86
Er	2.03	2.05	1.81	2.29	2.43	2.19	2.02
Yb	1.56	1.65	1.56	1.65	1.81	1.64	1.63
Hf	3.77	3.92	3.48	3.50	3.63	2.94	3.14
W	0.19	0.15	0.21	0.24	0.11	0.32	0.24
Pb	1.76	1.81	4.48	1.60	2.11	1.60	3.94
Tl	0.10	0.01	0.02	0.05			
Th	1.11	1.08	1.21	1.04	1.03	1.03	0.95
U	0.32	0.44	0.42	0.41	0.49	0.36	0.44

Table 2.5. (continued)

Sample	35	36	38	42	44	47	51
Li	6.44	5.84	5.79	4.89	5.47	6.34	5.60
B	3.33	3.38	3.08	3.30	3.23	2.30	2.98
Sc	32.6	31.8	30.7	25.9	29.5	27.0	31.5
V	387.6	380.6	381.0	413.2	422.4	377.4	401.7
Cr	318.3	357.8	249.2	198.4	512.8	316.5	578.1
Co	53.0	52.1	50.8	57.1	65.1	49.8	48.8
Ni	122	139	119	269	193	76	111
Cu	172	173	158	184	161	154	150
Zn	166	160	154	160	157	136	135
As	1.08	1.04	1.19	1.37	0.89	1.08	1.53
Rb	12.9	12.6	13.2	12.1	11.1	11.4	11.3
Sr	422	419	426	372	386	396	368
Y	20.7	20.1	21.8	16.7	17.7	17.9	18.3
Zr	143	142	151	121	130	129	135
Nb	18.8	17.9	18.9	15.3	17.4	20.2	19.7
Mo	1.53	0.90	1.10	0.93	1.47	0.94	1.01
Cd	0.27	0.04	0.28	0.27	0.44	0.21	0.24
In	0.13	0.14	0.11	0.08	0.10	0.08	0.08
Sn	1.93	1.92	2.00	2.11	1.98	1.85	1.42
Sb	0.13	0.29	0.19	0.16	0.13	0.09	0.10
Cs	0.09	0.13	0.15	0.15	0.21	0.15	0.23
Ba	175	170	170	153	156	163	158
La	15.2	15.7	16.1	12.6	14.5	16.1	15.9
Ce	45.9	44.2	45.9	43.1	41.3	44.1	43.2
Pr	5.56	5.37	5.38	4.61	5.16	5.76	5.48
Nd	25.4	24.6	23.5	19.7	22.9	24.0	24.4
Sm	6.17	5.92	5.66	4.20	5.16	5.28	5.37
Eu	1.93	1.98	1.93	1.80	1.92	2.02	1.93
Gd	5.08	5.43	5.41	4.18	4.52	4.68	5.18
Dy	4.90	4.58	4.62	3.63	4.00	3.74	4.46
Er	2.16	2.18	2.20	1.88	1.74	1.96	2.26
Yb	1.71	1.70	1.70	1.56	1.48	1.34	1.56
Hf	3.40	3.48	3.45	2.67	2.97	2.88	3.00
W	0.36	0.48	0.23	0.35	0.33	0.20	0.21
Pb	1.44	1.56	1.32	1.60	1.47	1.58	1.23
Tl	0.02	0.03	0.01	0.02	0.03	0.02	0.02
Th	0.98	1.13	1.09	1.03	1.00	1.00	1.26
U	0.56	0.43	0.46	0.43	0.40	0.51	0.46

Table 2.5. (continued)

Sample	53	55	56	58	60	61	62
Li	5.48	3.49	5.14	4.66	5.69	5.28	5.32
B	3.10	3.45	2.87	2.53	2.69	2.83	2.74
Sc	29.8	29.5	30.9	31.5	29.9	31.4	32.9
V	412.6	353.2	401.4	400.9	395.6	392.8	366.6
Cr	586.5	222.3	330.6	418.3	218.7	352.2	317.0
Co	61.4	46.2	48.5	56.7	43.9	48.3	45.0
Ni	165	118	109	164	111	336	234
Cu	165	150	153	144	125	152	140
Zn	162	133	142	142	123	141	122
As	0.80	0.91	0.65	0.71	0.88	0.64	1.58
Rb	11.4	8.6	10.9	11.4	12.6	10.9	10.8
Sr	390	347	395	407	408	404	399
Y	18.0	19.2	21.0	20.5	24.2	20.3	22.0
Zr	129	142	155	147	173	144	158
Nb	17.9	14.0	19.1	18.6	20.4	17.2	16.7
Mo	1.30	0.87	1.22	1.35	1.28	0.98	1.15
Cd	0.22	0.30	0.20	0.26	0.13	0.27	0.35
In	0.12	0.08	0.07	0.11	0.09		0.15
Sn	1.79	2.07	1.81	1.56	1.58	1.70	1.83
Sb	0.10	0.33	0.14	0.05	0.02	0.07	0.01
Cs	0.19	0.04	0.33	0.23	0.21	0.16	0.24
Ba	156	135	160	158	167	156	150
La	14.9	12.7	16.8	16.0	17.6	15.6	16.1
Ce	42.7	37.9	43.8	42.2	44.7	41.3	40.7
Pr	5.19	4.56	5.82	5.46	5.69	5.30	5.35
Nd	22.8	20.5	25.3	24.6	26.3	23.4	25.6
Sm	5.19	4.71	5.70	6.31	6.22	6.10	6.97
Eu	1.89	1.78	2.13	2.06	2.28	1.90	1.94
Gd	4.54	4.71	5.29	5.71	4.78	5.50	5.96
Dy	4.04	4.12	4.97	4.06	4.33	3.95	4.95
Er	1.79	1.88	1.76	2.48	2.49	2.33	2.68
Yb	1.44	1.33	1.71	2.10	1.51	1.63	1.86
Hf	3.08	3.49	3.30	3.46	4.31	3.43	4.87
W	0.10	0.22	0.35	0.36	0.29	0.21	0.10
Pb	1.54	1.28	1.33	1.47	1.34	1.12	1.41
Tl	0.03	0.01	0.01	0.02	0.03	0.01	0.02
Th	1.13	0.78	1.18	1.18	1.20	0.93	1.25
U	0.42	0.41	0.37	0.35	0.48	0.26	0.46

Table 2.5. (continued)

Sample	63	64	65	70	72	73	74
Li	4.28	3.94	3.64	4.08	4.93	5.17	5.72
B	2.71	3.08	2.89	3.42	3.97	2.67	2.31
Sc	32.9	34.5	32.6	30.7	31.6	28.9	30.7
V	383.8	359.0	381.7	380.0	388.6	365.9	427.1
Cr	331.8	505.0	279.5	677.4	386.4	406.4	664.8
Co	48.4	54.3	47.2	65.1	47.3	54.9	70.2
Ni	123	162	95	230	86	186	226
Cu	144	132	142	141	152	139	161
Zn	125	132	136	140	128	127	166
As	0.13	0.71	1.22	1.06	1.01	1.12	0.71
Rb	10.1	9.3	9.9	9.7	9.8	10.7	11.4
Sr	409	366	403	374	412	394	376
Y	22.2	21.6	23.3	19.8	20.9	19.2	17.5
Zr	154	150	165	133	144	132	123
Nb	17.8	16.3	17.6	16.4	16.6	16.7	15.8
Mo	1.03	1.02	0.78	0.98	1.35	1.07	1.09
Cd	0.33	0.22	0.28	0.29	0.31	0.13	0.34
In	0.20	0.07	0.10	0.19	0.01	0.21	0.11
Sn	1.89	1.44	1.69	1.52	1.68	2.09	1.62
Sb	0.14	0.11	0.09	0.20	0.15	0.08	0.16
Cs	0.32	0.12	0.12	0.17	0.13	0.19	0.12
Ba	154	133	148	142	151	152	149
La	16.9	14.8	17.8	15.2	15.2	14.9	14.0
Ce	40.7	36.8	40.5	39.4	40.3	40.0	41.5
Pr	5.57	4.85	5.89	5.02	4.98	5.17	4.77
Nd	26.1	22.6	26.4	23.4	22.7	22.7	21.5
Sm	6.56	4.82	6.06	4.92	5.34	6.06	5.09
Eu	1.94	1.91	2.09	1.70	1.88	1.89	1.76
Gd	6.57	5.40	7.10	4.49	5.44	5.47	4.40
Dy	4.31	5.08	6.44	4.03	4.18	3.90	3.91
Er	1.89	2.50	3.18	2.53	2.28	2.00	1.80
Yb	1.53	1.74	1.98	1.45	1.66	1.58	1.43
Hf	4.44	3.92	4.71	3.28	3.49	3.38	3.35
W	0.25	0.17	0.42	0.38	0.27	0.27	0.31
Pb	1.51	1.20	1.38	1.22	2.49	1.47	1.57
Tl	0.01	0.02	0.01	0.01	0.02	0.01	0.01
Th	1.17	1.41	1.28	1.17	1.14	1.11	0.98
U	0.41	0.37	0.29	0.37	0.34	0.50	0.50

Table 2.5. (continued)

Sample	76	06-01	06-02	06-08	06-09	07-01	07-02
Li	5.66						
B	3.28	2.44	2.42	2.48	2.25	2.45	2.57
Sc	29.1	33.5	34.2	32.8	32.3	32.3	33.5
V	397.7	396.5	379.9	403.3	403.6	369.4	369.6
Cr	321.1	472.1	375.8	430.9	420.7	520.1	301.1
Co	49.8	55.5	52.6	56.4	54.7	57.0	49.9
Ni	125						
Cu	155	122	207	152	120	143	145
Zn	141	126	155	136	136	133	126
As	0.74	0.69	0.66	0.75	0.48	0.77	0.44
Rb	11.3	10.4	10.8	12.6	11.3	11.1	10.5
Sr	410	407	399	397	407	392	414
Y	19.7	21.8	21.6	19.1	20.8	21.1	22.3
Zr	138	148	148	138	142	146	156
Nb	18.7						
Mo	1.53	1.01	1.29	1.13	0.91	1.20	1.04
Cd	0.15	0.18	0.27	0.15	0.22	0.17	0.19
In	0.13	0.11	0.12	0.09	0.14	0.14	0.21
Sn	1.23	1.58	1.67	1.43	1.74	1.55	1.61
Sb	0.14	0.11	0.14	0.10	0.16	0.11	0.12
Cs	0.24						
Ba	161	159	155	160	159	149	161
La	15.9						
Ce	44.9	44.1	41.3	44.6	43.1	40.7	41.2
Pr	5.51						
Nd	26.0						
Sm	5.64						
Eu	1.90						
Gd	4.92						
Dy	4.20						
Er	1.66						
Yb	1.66						
Hf	3.38						
W	0.19	0.31	0.29	0.28	0.31	0.24	0.19
Pb	1.56	1.28	1.33	1.38	1.52	1.14	1.59
Tl	0.01	0.02	0.02	0.02	0.01	0.02	0.02
Th	1.16						
U	0.40						

Table 2.5. (continued)

Sample	07-03	07-04	07-05	07-06	07-07	07-08	07-09
Li							
B	1.85	1.99	1.87	1.38	2.39	2.04	2.45
Sc	33.6	33.3	32.8	33.6	31.4	31.5	31.8
V	324.7	365.1	388.3	362.6	405.2	410.2	390.2
Cr	361.8	410.9	518.2	483.6	400.0	368.1	469.4
Co	42.3	50.3	57.7	55.5	49.9	52.8	54.8
Ni							
Cu	106	106	136	138	154	155	131
Zn	96	121	130	125	133	136	124
As	2.24	0.59	0.51	0.44	0.58	0.65	0.51
Rb	8.9	10.0	10.7	10.3	11.7	11.7	10.9
Sr	386	409	401	406	403	406	400
Y	22.3	23.0	20.5	22.0	20.9	19.6	20.2
Zr	163	155	146	153	148	138	142
Nb							
Mo	0.75	1.08	1.06	1.04	1.09	1.03	0.76
Cd	0.18	0.19	0.18	0.26	0.16	0.10	0.18
In	0.13	0.10	0.08	0.25	0.25	0.08	0.06
Sn	1.41	1.51	1.48	1.58	1.64	1.59	1.29
Sb	0.17	0.10	0.11	0.14	0.10	0.07	0.12
Cs							
Ba	136	154	155	148	164	161	162
La							
Ce	34.8	41.4	43.4	41.7	45.5	43.4	43.3
Pr							
Nd							
Sm							
Eu							
Gd							
Dy							
Er							
Yb							
Hf							
W	0.23	0.28	0.20	0.16	0.23	0.29	0.26
Pb	5.61	1.64	1.35	1.33	1.77	1.38	1.06
Tl	0.02	0.01	0.01	0.02	0.02	0.03	0.02
Th							
U							

Table 2.6. Corrected melt inclusion major element (wt. %) composition.

Sample	01-01-1	01-01-2	01-05	01-13	02-10	02-13-1	02-13-2
PEC %*	13.8	13.2	14.1	13.0	12.3	9.7	10.8
Temp. (C)	1275	1307	1309	1310	1280	1246	1260
SiO_2	49.06	49.09	48.73	48.82	48.89	48.67	49.15
TiO_2	2.31	2.10	2.70	2.34	2.53	2.37	2.31
Al_2O_3	12.05	11.70	12.26	11.58	11.90	11.98	11.83
Cr_2O_3	0.05	0.09	0.07	0.05	0.05	0.09	0.08
FeO*	10.93	10.99	10.97	10.99	10.93	10.91	10.93
MnO	0.14	0.18	0.14	0.15	0.15	0.16	0.14
MgO	11.42	12.24	12.51	12.66	11.55	10.67	11.01
CaO	11.10	10.71	9.48	10.36	11.03	12.31	11.88
Na_2O	2.13	2.10	2.11	2.16	2.01	1.85	1.86
K_2O	0.37	0.34	0.58	0.35	0.48	0.30	0.33
P_2O_5	0.22	0.22	0.29	0.34	0.26	0.48	0.33
S	0.13	0.13	0.02	0.11	0.11	0.13	0.06
Cl	0.02	0.01	0.01	0.01	0.02	0.01	0.02
F	0.01	0.02	0.04	0.02	0.03	0.02	0.02
NiO	0.06	0.07	0.08	0.05	0.06	0.04	0.06
Total	100.00	100.00	100.00	100.00	100.00	100.00	100.00
Fo (host)	87.2	87.2	88.0	88.1	87.3	86.8	86.9

*Post entrapment crystallization percentage.

Sample	03-01	03-03	03-04	03-09-1	03-09-2	03-06	03-25
PEC %	9.2	11.4	13.8	8.1	8.1	17.3	3.7
Temp. (C)	1276	1278	1289	1266	1263	1311	1232
SiO_2	49.26	48.57	48.18	48.81	48.80	48.04	50.00
TiO_2	2.39	2.51	2.47	2.37	2.47	2.35	2.37
Al_2O_3	11.98	11.88	11.92	12.20	11.93	11.38	12.31
Cr_2O_3	0.11	0.06	0.08	0.08	0.08	0.10	0.08
FeO*	10.91	10.94	10.97	10.93	10.91	11.01	10.86
MnO	0.18	0.15	0.12	0.14	0.15	0.14	0.16
MgO	11.25	11.64	12.17	11.15	11.06	13.01	9.89
CaO	10.75	11.53	11.40	11.62	11.91	11.47	11.53
Na_2O	2.18	1.84	1.70	1.92	1.79	1.69	1.94
K_2O	0.46	0.40	0.47	0.36	0.38	0.31	0.45
P_2O_5	0.29	0.26	0.29	0.32	0.27	0.26	0.24
S	0.14	0.13	0.11	0.03	0.15	0.13	0.11
Cl	0.02	0.02	0.02	0.01	0.02	0.01	0.02
F	0.02	0.02	0.02	0.02	0.03	0.03	0.02
NiO	0.05	0.04	0.07	0.03	0.05	0.07	0.03
Total	100.00	100.00	100.00	100.00	100.00	100.00	100.00
Fo (host)	87.0	87.5	87.9	87.1	87.0	88.5	85.8

Table 2.6. (continued)

Sample	03-26	04-06	04-09	04-10-1	04-10-2	04-17	04-22
PEC %	8.6	9.7	9.4	18.2	17.9	18.3	12.1
Temp. (C)	1223	1273	1264	1274	1280	1306	1268
SiO_2	49.29	49.29	48.62	47.58	48.07	48.74	48.91
TiO_2	2.46	2.40	2.51	2.46	2.34	2.13	2.54
Al_2O_3	12.53	11.92	12.03	12.41	12.21	11.16	11.76
Cr_2O_3	0.08	0.06	0.07	0.11	0.07	0.09	0.11
FeO*	10.85	10.93	10.94	10.95	10.95	11.00	10.94
MnO	0.17	0.17	0.16	0.10	0.13	0.16	0.18
MgO	9.53	11.35	11.25	11.73	11.83	12.83	11.30
CaO	12.07	11.03	11.63	11.99	11.58	11.20	11.50
Na_2O	2.17	2.09	1.85	1.72	1.98	1.72	1.80
K_2O	0.40	0.35	0.46	0.40	0.39	0.35	0.44
P_2O_5	0.25	0.22	0.27	0.27	0.24	0.40	0.31
S	0.14	0.11	0.10	0.13	0.11	0.12	0.13
Cl	0.02	0.01	0.02	0.02	0.01	0.01	0.01
F	0.02	0.01	0.02	0.03	0.03	0.02	0.01
NiO	0.03	0.05	0.06	0.08	0.05	0.08	0.05
Total	100.00	100.00	100.00	100.00	100.00	100.00	100.00
Fo (host)	85.6	87.1	87.2	87.8	87.7	88.3	87.2

Sample	04-25	04-23	01-06b-1	01-06b-2	01-06b-3	02-01b-1	02-01b-2
PEC %	11.1	10.7	12.2	11.7	16.6	9.9	10.4
Temp. (C)	1231	1281	1304	1273	1322	1254	1263
SiO_2	50.05	49.18	47.48	48.49	48.15	50.33	50.30
TiO_2	2.71	2.34	2.43	2.47	2.64	2.30	2.33
Al_2O_3	12.75	11.87	11.91	12.26	11.65	12.25	12.29
Cr_2O_3	0.03	0.09	0.05	0.08	0.07	0.05	0.09
FeO*	10.88	10.95	10.96	10.94	11.00	10.96	10.96
MnO	0.15	0.11	0.13	0.15	0.15	0.16	0.14
MgO	9.90	11.76	12.15	11.64	12.74	11.59	11.76
CaO	10.65	10.84	10.92	11.33	10.16	10.95	10.59
Na_2O	1.99	2.05	1.99	1.38	2.21	0.60	0.67
K_2O	0.52	0.36	0.82	0.60	0.59	0.36	0.38
P_2O_5	0.27	0.23	0.91	0.44	0.39	0.23	0.26
S	0.02	0.10	0.11	0.12	0.10	0.11	0.13
Cl	0.01	0.01	0.03	0.02	0.03	0.01	0.01
F	0.03	0.03	0.05	0.04	0.04	0.02	0.01
NiO	0.05	0.05	0.06	0.05	0.09	0.07	0.07
Total	100.00	100.00	100.00	100.00	100.00	100.00	100.00
Fo (host)	85.8	87.5	87.9	87.6	88.1	87.4	87.5

Table 2.6. (continued)

Sample	02-05b	02-15b	02-13b	02-10b	03-01b	03-04b	03-08b
PEC %	4.1	7.8	8.7	8.2	10.4	6.3	8.1
Temp. (C)	1263	1243	1269	1279	1285	1277	1222
SiO_2	49.31	49.27	48.18	48.09	48.89	49.44	50.54
TiO_2	2.32	2.44	2.55	2.94	2.47	2.80	2.39
Al_2O_3	12.45	12.47	12.13	12.23	12.01	12.64	12.40
Cr_2O_3	0.06	0.07	0.11	0.06	0.09	0.07	0.07
FeO*	10.90	10.88	10.92	10.92	10.95	10.85	10.91
MnO	0.13	0.18	0.16	0.14	0.15	0.17	0.16
MgO	10.58	10.29	11.26	11.22	11.66	9.49	10.41
CaO	11.32	11.57	11.93	11.11	10.66	12.02	11.70
Na_2O	2.04	2.00	1.93	2.11	2.14	1.71	0.61
K_2O	0.39	0.35	0.34	0.64	0.47	0.53	0.35
P_2O_5	0.28	0.26	0.34	0.32	0.28	0.29	0.23
S	0.13	0.13	0.07	0.13	0.13	0.12	0.13
Cl	0.02	0.01	0.01	0.02	0.02	0.02	0.01
F	0.03	0.03	0.03	0.02	0.02	0.04	0.03
NiO	0.04	0.06	0.06	0.03	0.07	-0.19	0.05
Total	100.00	100.00	100.00	100.00	100.00	100.00	100.00
Fo (host)	86.4	86.3	87.3	87.2	87.4	85.0	86.4

Sample	03-24b	03-25b	04-24b
PEC %	0.4	3.4	13.3
Temp. (C)	1210	1229	1327
SiO_2	49.64	49.71	48.50
TiO_2	2.61	2.44	2.29
Al_2O_3	12.32	12.51	11.30
Cr_2O_3	0.07	0.05	0.07
FeO*	10.82	10.86	11.03
MnO	0.17	0.16	0.17
MgO	9.14	9.73	13.46
CaO	12.20	11.66	10.51
Na_2O	2.00	2.03	1.87
K_2O	0.46	0.46	0.33
P_2O_5	0.35	0.22	0.23
S	0.16	0.10	0.12
Cl	0.02	0.01	0.01
F	0.01	0.04	0.04
NiO	0.05	0.03	0.07
Total	100.00	100.00	100.00
Fo (host)	85.1	85.7	88.6

Table 2.7. Corrected melt inclusion trace element composition (ppm).

Sample	01-01-2	01-05	01-13	02-10	02-13-1	02-13-2	03-01
B	1.61	2.24	2.22	2.90	4.88	9.48	2.80
Sc	31.7	25.8	28.0	28.9	32.3	32.0	29.7
V	331	277	327	330	376	371	343
Cr							
Co							
Cu	77	128	52	92	76	104	97
Zn	125	98	124	114	120	114	133
Rb	7.3	11.5	7.0	11.1	4.9	8.5	9.0
Sr	320	380	326	385	264	834	384
Y	17.1	21.7	16.5	18.1	19.7	18.4	17.3
Zr	119	164	115	136	102	112	136
Mo	0.99	1.33	0.97	1.10	0.77	1.18	1.20
Ag	0.07	0.08		0.04	0.04	0.09	
Cd	0.22	0.17	0.06	0.34	0.13		0.19
In	0.10	0.07	0.07	0.04	0.09	0.08	0.09
Sn	1.31	1.61	1.45	1.33	1.00	1.22	1.57
Sb	0.08	0.02	0.06			0.23	
Ba	96	144	98	142	73	156	121
Ce	29.0	39.5	30.3	39.7	23.5	26.5	36.3
W	0.15	0.22	0.21	0.25		0.14	0.22
Pb	0.98	1.33	1.08	1.22	0.72	1.52	1.16
U	0.29	0.42	0.27	0.47	0.23	0.31	0.41

Sample	03-03	03-04	03-09-1	03-09-2	03-06	03-25	04-06
B	2.87	2.80	2.22	3.08	3.63	2.30	2.42
Sc	27.9	29.1	29.7	31.3	29.6	29.5	29.3
V	383	367	359	379	358	360	317
Cr							
Co							
Cu	72	60	127	109	87	161	105
Zn	129	164	117	131	174	144	120
Rb	11.0	10.7	7.1	8.1	7.1	9.6	6.3
Sr	360	430	281	359	319	340	317
Y	16.8	18.4	16.9	19.0	18.7	17.2	18.8
Zr	111	148	104	129	123	110	115
Mo	1.09	1.65	0.92	1.05	1.50	0.98	0.85
Ag	0.04	0.18	0.06	0.04		0.04	0.05
Cd	0.26	0.54		0.11	0.22	0.11	0.21
In	0.07	0.07	0.08	0.08	0.09	0.10	0.08
Sn	1.53	2.18	1.23	1.26	1.64	1.43	1.34
Sb	0.09	0.07					0.04
Ba	140	143	101	113	93	124	93
Ce	39.3	48.6	28.5	37.2	33.2	34.0	27.5
W	0.23	0.28			0.17	0.21	0.17
Pb	1.42	1.68	0.90	0.94	1.04	1.07	0.92
U	0.44	0.53	0.29	0.37	0.29	0.35	0.24

Table 2.7. (continued)

Sample	04-09	04-25	04-23	01-06b-1	01-06b-2	01-06b-3
B	4.01	1.95	2.49	2.89	2.53	3.41
Sc	29.9	28.7	28.5	32.2	31.3	30.9
V	406	336	328	287	292	241
Cr				427	430	391
Co				36.8	38.2	27.7
Cu	127	107	100	25	25	25
Zn	147	125	123	94	95	96
Rb	10.6	10.4	6.9	14.2	10.0	9.3
Sr	366	389	311	641	542	647
Y	16.5	20.8	17.4	20.2	21.5	22.0
Zr	121	145	110	181	179	248
Mo	1.26	1.02	0.82	1.60	1.37	1.37
Ag	0.05	0.08	0.05			
Cd	0.16	0.08	0.27	0.25	0.48	0.21
In	0.10	0.09	0.09			
Sn	1.57	1.54	1.48	1.71	1.87	2.38
Sb		0.06	0.06			
Ba	140	151	93	199	149	181
Ce	42.5	38.9	28.6	47.5	40.5	51.9
W		0.19	0.23	0.33	0.26	0.43
Pb	1.24	1.13	1.04	2.59	1.33	4.07
U	0.38	0.40	0.27			

Sample	02-01b-2	02-05b	02-15b	02-13b	02-10b	03-01b
B	1.54	1.46		2.34	2.44	
Sc	28.8	28.5	36.2	32.7	33.0	29.3
V	317	306	268	311	339	342
Cr	525	453	424	378	481	710
Co	45.2	44.7	35.3	41.2	45.0	49.1
Cu	128	144	94	88	61	106
Zn	115	121	95	91	103	128
Rb	7.3	7.0	5.3	4.3	12.3	6.7
Sr	284	324	323	460	475	370
Y	17.4	17.5	23.0	20.1	20.2	18.4
Zr	108	120	143	130	165	134
Mo	0.90	1.32	0.63	0.64	1.14	0.49
Ag						
Cd	0.15	0.17	0.01	0.46	0.24	
In						
Sn	1.18	1.26	0.94	1.51	1.66	2.22
Sb						
Ba	104	105	86	276	194	128
Ce	26.8	31.0	25.1	30.3	49.0	34.5
W	0.17	0.12	0.08		0.26	0.46
Pb	1.00	0.98	0.66	0.67	1.30	1.16
U						

Table 2.7. (continued)

Sample	03-08b	03-24b	03-25b	04-24b	04-10-1	04-10-2	04-17
B			4.15	1.55			
Sc	37.8	37.2	30.6	31.2			
V	383	428	406	293			
Cr	464	642	556	545			
Co	46.6	64.1	59.4	44.4			
Cu	70	169	176	113			
Zn	118	151	144	118			
Rb	6.5	9.3	11.0	5.7			
Sr	297	400	354	286			
Y	20.2	18.0	17.9	19.6			
Zr	121	145	114	126			
Mo	2.00		2.86	0.77			
Ag							
Cd	0.43	0.75	0.36	0.11			
In							
Sn	1.86	1.52	2.31	1.57			
Sb							
Ba	98	122	134	83			
Ce	27.0	37.7	35.4	26.3			
W	0.17	0.18		0.06			
Pb	3.80	1.37	1.35	1.49	1.05	0.67	0.78
U					0.39	0.55	0.35

Sample	04-22	01-01-1	03-26
B			
Sc			
V			
Cr			
Co			
Cu			
Zn			
Rb			
Sr			
Y			
Zr			
Mo			
Ag			
Cd			
In			
Sn			
Sb			
Ba			
Ce			
W	0.27		
Pb	1.56		
U	0.56		

Table 2.8. Olivine major element composition (wt. %) by EMPA.

Sample	01-01-1	01-01-2	01-05	01-13	02-10	02-13-1	02-13-2
SiO_2	39.70	39.70	39.62	39.86	39.63	39.69	39.74
TiO_2	0.01	0.01	0.02	0.02	0.03	0.02	0.02
Al_2O_3	0.06	0.06	0.05	0.06	0.05	0.05	0.06
Cr_2O_3	0.08	0.08	0.08	0.09	0.07	0.06	0.07
FeO*	12.31	12.31	11.61	11.51	12.15	12.74	12.51
MnO	0.17	0.17	0.16	0.19	0.19	0.18	0.17
MgO	47.12	47.12	47.66	47.64	47.00	46.92	46.64
CaO	0.26	0.26	0.24	0.24	0.30	0.28	0.31
Na_2O	0.00	0.00	0.00	0.00	-0.01	0.01	0.00
K_2O	0.00	0.00	0.00	0.00	-0.01	-0.01	-0.01
NiO	0.41	0.41	0.42	0.45	0.41	0.38	0.37
Total	100.12	100.12	99.85	100.06	99.80	100.32	99.87
Fo	87.2	87.2	88.0	88.1	87.3	86.8	86.9

Sample	03-01	03-03	03-04	03-09-1	03-09-2	03-06	03-25
SiO_2	39.31	39.61	39.72	39.61	39.45	39.53	39.52
TiO_2	0.02	0.03	0.02	0.02	0.03	0.02	0.01
Al_2O_3	0.05	0.05	0.05	0.05	0.07	0.08	0.06
Cr_2O_3	0.08	0.08	0.08	0.06	0.08	0.08	0.05
FeO*	12.40	11.99	11.62	12.34	12.32	11.04	13.53
MnO	0.15	0.15	0.14	0.17	0.18	0.10	0.17
MgO	46.63	47.03	47.57	46.63	46.40	47.59	45.81
CaO	0.26	0.29	0.29	0.30	0.29	0.26	0.29
Na_2O	-0.01	0.00	0.00	0.00	0.00	0.01	0.01
K_2O	0.00	0.00	-0.01	0.00	0.00	0.00	0.01
NiO	0.41	0.35	0.37	0.35	0.34	0.39	0.38
Total	99.31	99.58	99.84	99.54	99.15	99.09	99.85
Fo	87.0	87.5	87.9	87.1	87.0	88.5	85.8

Sample	03-26	04-06	04-09	04-10-1	04-10-2	04-17	04-22
SiO_2	39.53	39.86	39.61	40.16	39.59	40.55	40.09
TiO_2	0.01	0.01	0.02	0.02	0.02	0.01	0.01
Al_2O_3	0.04	0.06	0.04	0.05	0.05	0.06	0.05
Cr_2O_3	0.05	0.07	0.07	0.08	0.08	0.09	0.08
FeO*	13.77	12.37	12.39	11.82	11.93	11.31	12.30
MnO	0.21	0.19	0.16	0.15	0.14	0.18	0.19
MgO	45.75	46.96	47.39	47.62	47.83	47.68	46.89
CaO	0.28	0.26	0.27	0.28	0.28	0.26	0.27
Na_2O	0.01	0.00	0.01	0.01	0.01	0.00	0.00
K_2O	0.00	0.00	-0.01	0.00	0.00	-0.01	0.00
NiO	0.30	0.39	0.37	0.40	0.36	0.45	0.39
Total	99.95	100.18	100.31	100.59	100.29	100.58	100.27
Fo	85.6	87.1	87.2	87.8	87.7	88.3	87.2

Table 2.8. (continued)

Sample	04-25	04-23	01-06b-1	01-06b-2	01-06b-3	02-01b-1	02-01b-2
SiO_2	39.75	39.77	39.74	39.74	39.83	39.58	39.64
TiO_2	0.02	0.02	0.03	0.01	0.02	0.01	0.02
Al_2O_3	0.06	0.04	0.06	0.06	0.07	0.06	0.05
Cr_2O_3	0.06	0.08	0.08	0.07	0.10	0.07	0.09
FeO*	13.68	12.15	11.55	11.91	11.31	12.08	11.92
MnO	0.21	0.16	0.20	0.19	0.13	0.18	0.13
MgO	46.25	47.55	47.13	47.02	47.19	46.86	46.61
CaO	0.28	0.25	0.24	0.25	0.24	0.25	0.26
Na_2O	0.01	-0.01	0.01	0.01	0.01	0.01	0.01
K_2O	0.00	-0.01	-0.01	0.00	0.00	-0.01	0.01
NiO	0.35	0.40	0.37	0.41	0.43	0.37	0.42
Total	100.68	100.40	99.40	99.68	99.35	99.47	99.15
Fo	85.8	87.5	87.9	87.6	88.1	87.4	87.5

Sample	02-05b	02-15b	02-13b	02-10b	03-01b	03-08b	03-24b
SiO_2	38.78	39.29	39.40	39.51	39.65	39.89	39.23
TiO_2	0.02	0.02	0.01	0.02	0.01	0.01	0.02
Al_2O_3	0.03	0.03	0.05	0.05	0.06	0.05	0.04
Cr_2O_3	0.05	0.07	0.09	0.08	0.07	0.06	0.07
FeO*	12.59	13.05	12.12	12.18	12.12	12.94	14.14
MnO	0.18	0.20	0.18	0.19	0.16	0.18	0.18
MgO	44.99	46.08	46.70	46.41	47.10	46.19	45.37
CaO	0.27	0.28	0.27	0.25	0.25	0.27	0.30
Na_2O	0.00	0.02	0.00	0.00	0.00	0.00	0.00
K_2O	-0.02	0.00	0.00	0.02	-0.01	0.02	0.00
NiO	0.35	0.38	0.38	0.35	0.42	0.36	0.39
Total	97.24	99.42	99.20	99.06	99.84	99.96	99.73
Fo	86.4	86.3	87.3	87.2	87.4	86.4	85.1

Sample	03-25b	04-24b
SiO_2	39.50	40.09
TiO_2	0.02	0.02
Al_2O_3	0.06	0.08
Cr_2O_3	0.04	0.09
FeO*	13.64	10.93
MnO	0.19	0.15
MgO	45.73	47.75
CaO	0.29	0.25
Na_2O	0.01	0.00
K_2O	-0.01	-0.02
NiO	0.34	0.43
Total	99.82	99.77
Fo	85.7	88.6

Table 2.9. Olivine trace element composition (ppm).

Sample	01-01-1	01-05	01-13	04-06	04-10-1	04-17	04-23
B	0.8	1.3		1.0		0.6	1.1
Ca	980	1370	665	1267	1244	1485	1143
Sc	4.9	5.8	4.8	6.6	6.4	6.4	6.6
Ti	56.5	77.3	48.1	71.5	70.2	72.0	63.3
V	7.4	7.1	10.4	7.6	7.6	7.6	8.7
Cu	9.2	5.8	7.2	6.0	6.5	6.1	4.6
Zn	104	96	134	100	98	93	113
Y	0.0	0.1	0.1	0.1	0.1	0.1	0.1
Zr		0.1	0.0	0.1	0.0	0.1	0.1
Mo	0.8	0.5	1.3	0.7	0.8	1.2	0.9
Cd		0.1			0.1	0.0	0.1
Sn	0.4	0.3	0.1	0.4	0.5	0.5	0.3

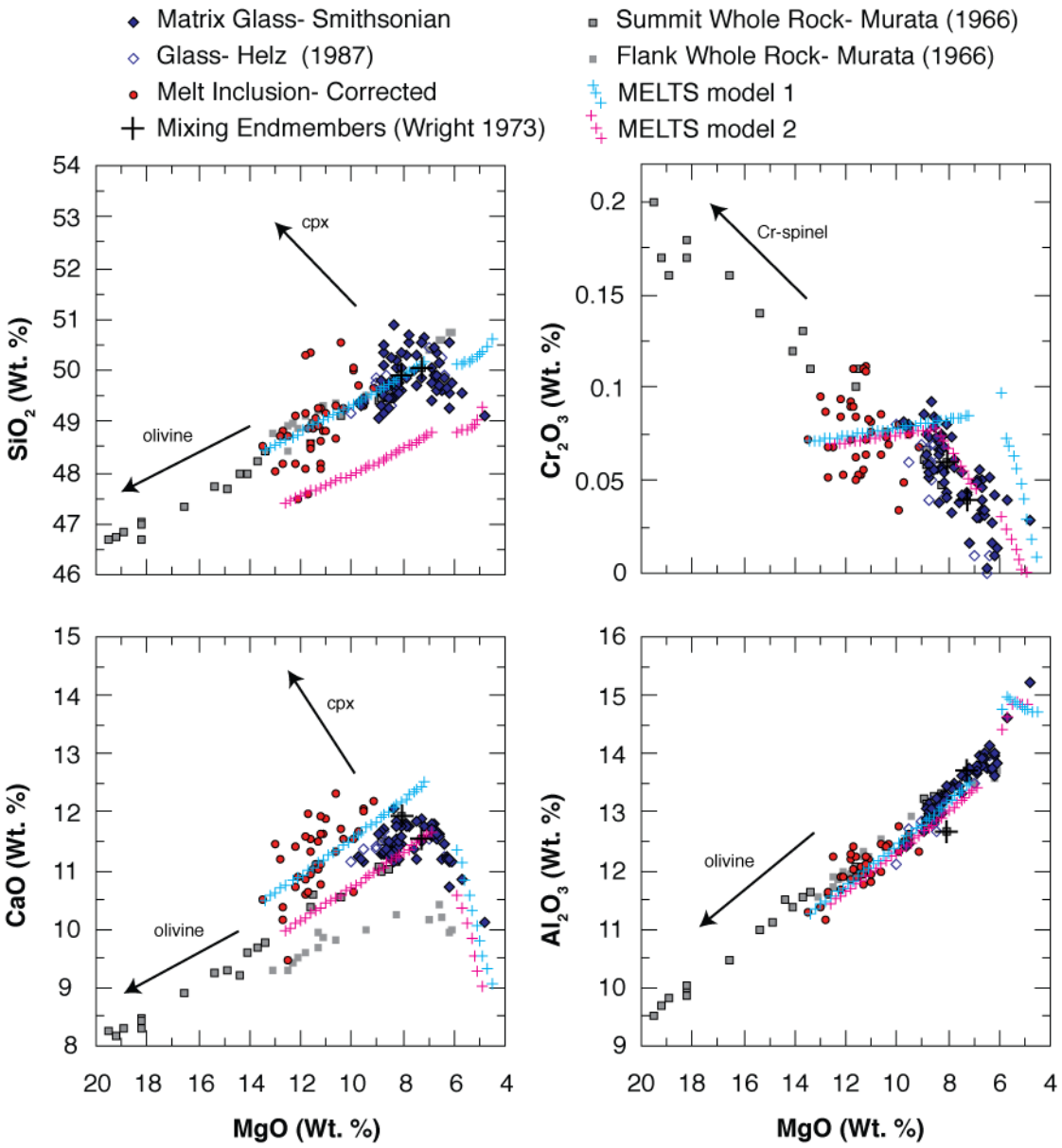

Figure 2.6. Major element Fenner diagrams. These show influence of olivine and Cr-spinel and late clinopyroxene (cpx) control on glass values <7 wt. % MgO. Corrections for PEC place melt inclusions at more primitive values than glass and in line with expected compositional trends. Note linearity of Al_2O_3 at all MgO values that suggests no involvement of plagioclase. Preliminary MELTs modeling easily matches the trend of the data with a 1 kbar depth, 0.5 wt.% water, and primitive melt inclusion starting compositions. Note very late plagioclase in the MELTs model is consistent with observations of rare plagioclase microlites in thin section observations by Helz (1987).

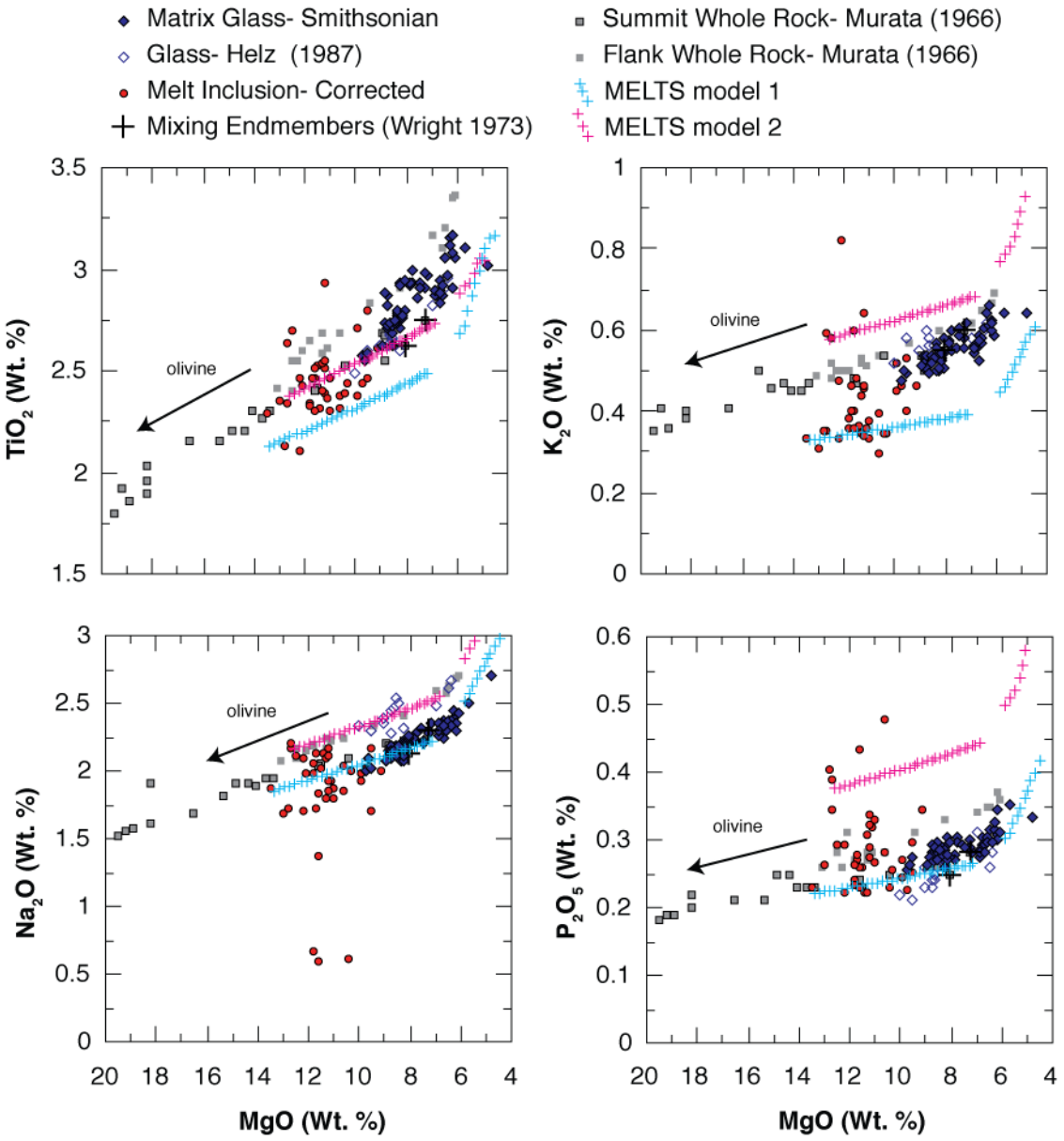

Figure 2.7. Incompatible major elements all correlate linearly with MgO. Melt inclusion compositions are considerably more scattered than glass compositions although analytical conditions are identical for both materials. There is no consistent relationship, however, between inclusions that are unusually low in Na and high or low in K. Note that MELTs models again generally bracket observations. Models above and below the main glass trend are due to starting with anomalous melt inclusion compositions.

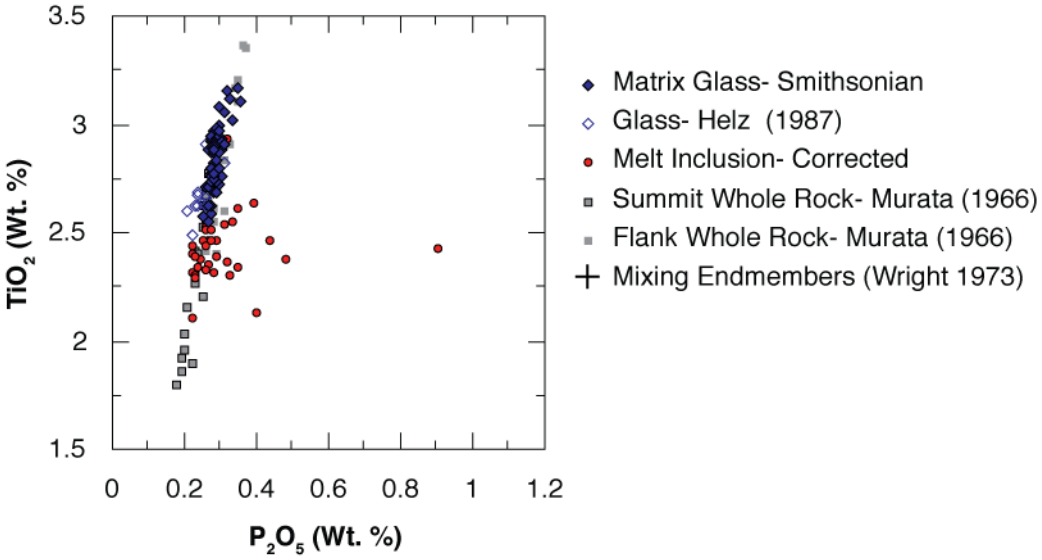

Figure 2.8. Ti and P are tightly correlated for whole rock and glass compositions, but several melt inclusions are unusually high in P. These inclusions could be enriched from trapping of a boundary layer, although experimental work (Faure and Schiano, 2005) has suggested that boundary layers should also be enriched in Al in Fig. 6. Most melt inclusions are in-line with glass and whole rock values.

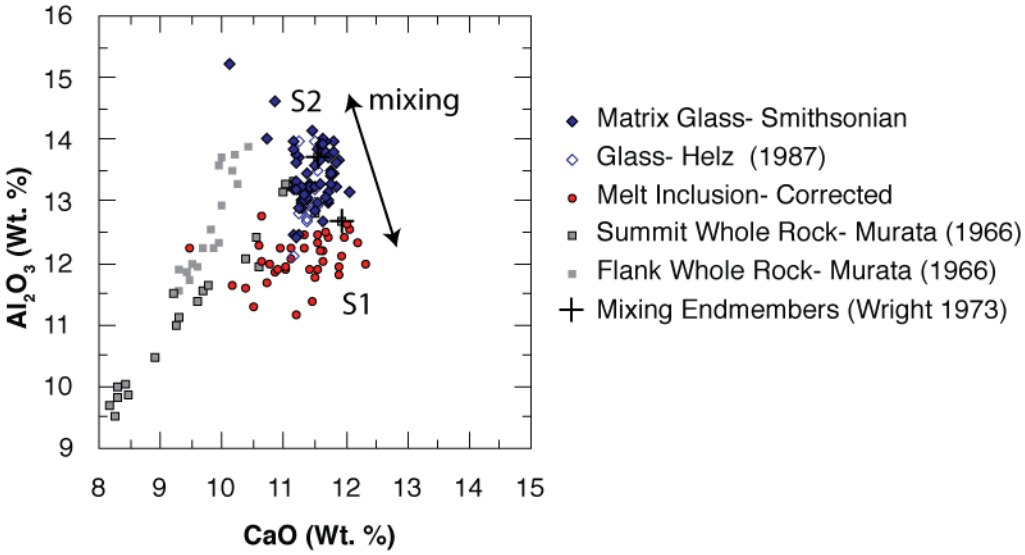

Figure 2.9. Variation in Ca and Al highlight the mixing endmembers S-1 and S-2 identified by Wright (1973) in whole rock compositions. Our measured values generally lie between these two compositions while melt inclusions have more affinity with the S-1 endmember.

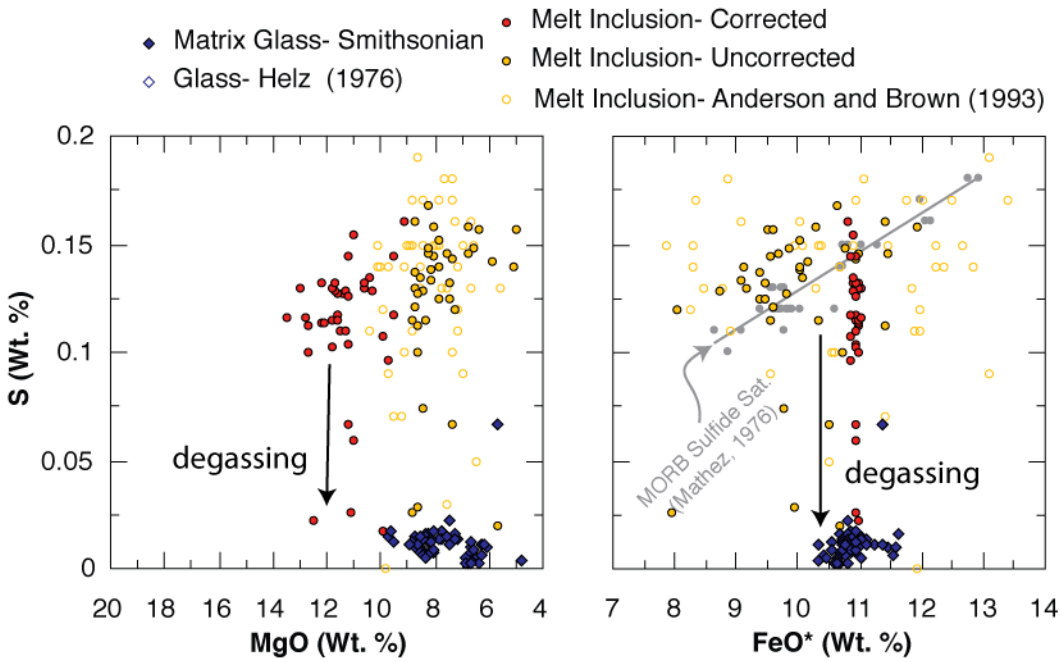

Figure 2.10. Volatile elements measured with EMPA. Sulfur is strongly degassed in matrix glass while melt inclusions lie close to or at sulfide saturation (both theoretical as calculated by Wallace and Anderson, 1998, and measured values in sulfide saturated MORB glasses from Mathez, 1987).

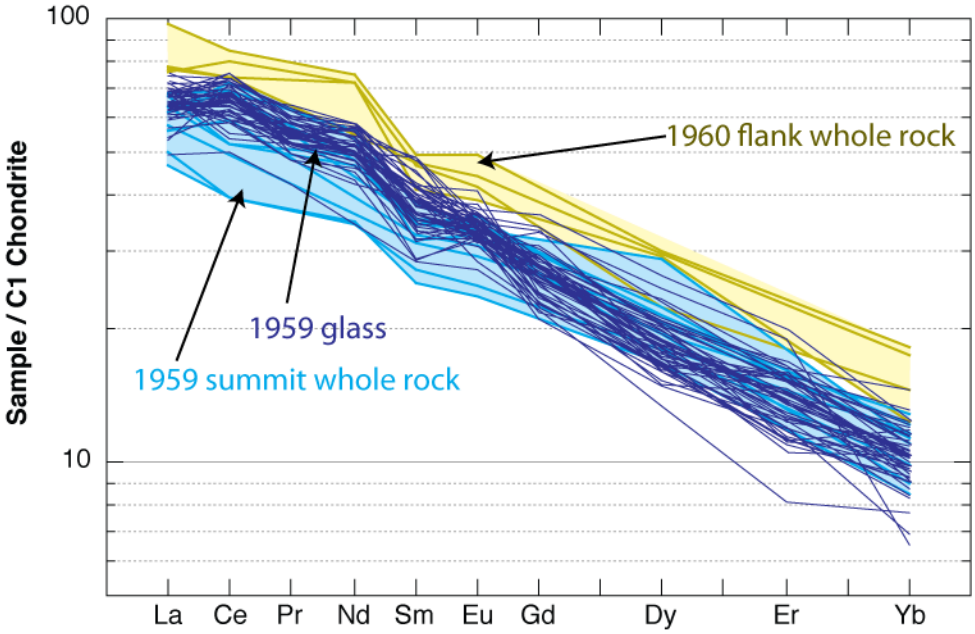

Figure 2.11. Chondrite-normalized rare earth element variations diagram. Whole rock values from the 1959 summit eruption and 1960 flank eruption are shown for reference (Tilling *et al*., 1987), while chondritic values are from (McDonough and Sun, 1995). LA-ICP-MS compositions are consistent with previous work suggesting an enriched source typical of ocean island basalts but distinct from the 1960 flank lavas and other Kilauean summit eruptions.

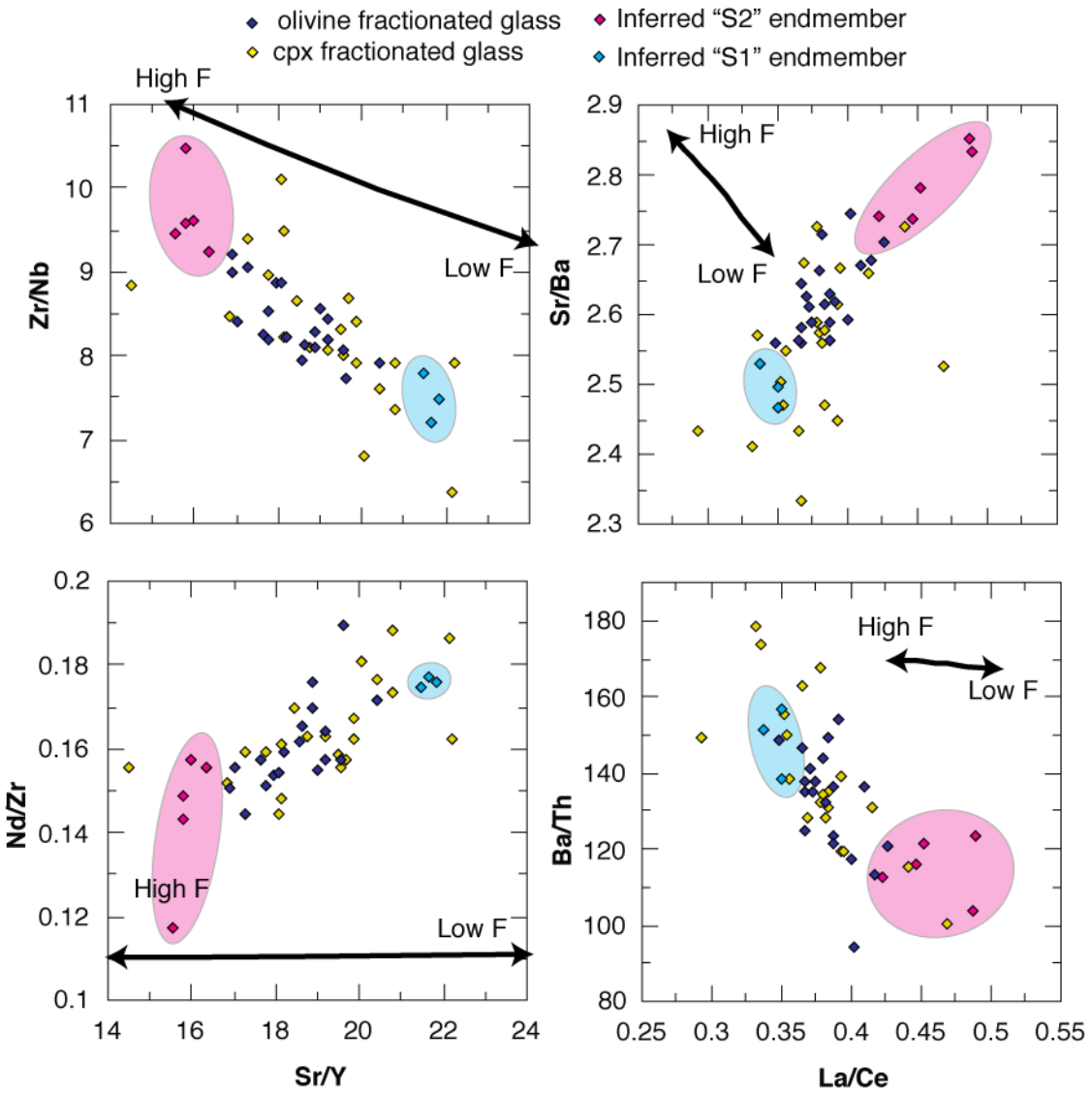

Figure 2.12. Several incompatible trace element ratios show strong mixing variations. This variation can be only explained by mixing of at least two compositional endmembers. Also shown are conceptual vectors for batch partial melting of a garnet-lherzolite source (note: these are vectors only showing the trend and magnitude of ratio variations with various partial melt percentages, not actual partial melt compositions). The lines on the right two graphs are proportional to a partial melt percentage (F) = ~8-22%; these same endpoints extend well beyond the axis of the left two graphs. While partial melting can explain the approximate shape of variation for Zr/Nb, and to a lesser extent Nd/Zr and Ba/Th, a single partial melting model does not fit for all ratios. In addition, partial melting cannot explain the La/Ce variations. These plots suggest that compositions are controlled by two magma batches each with distinct sources, and that the S-2 component may have been the result of a higher degree of partial melt.

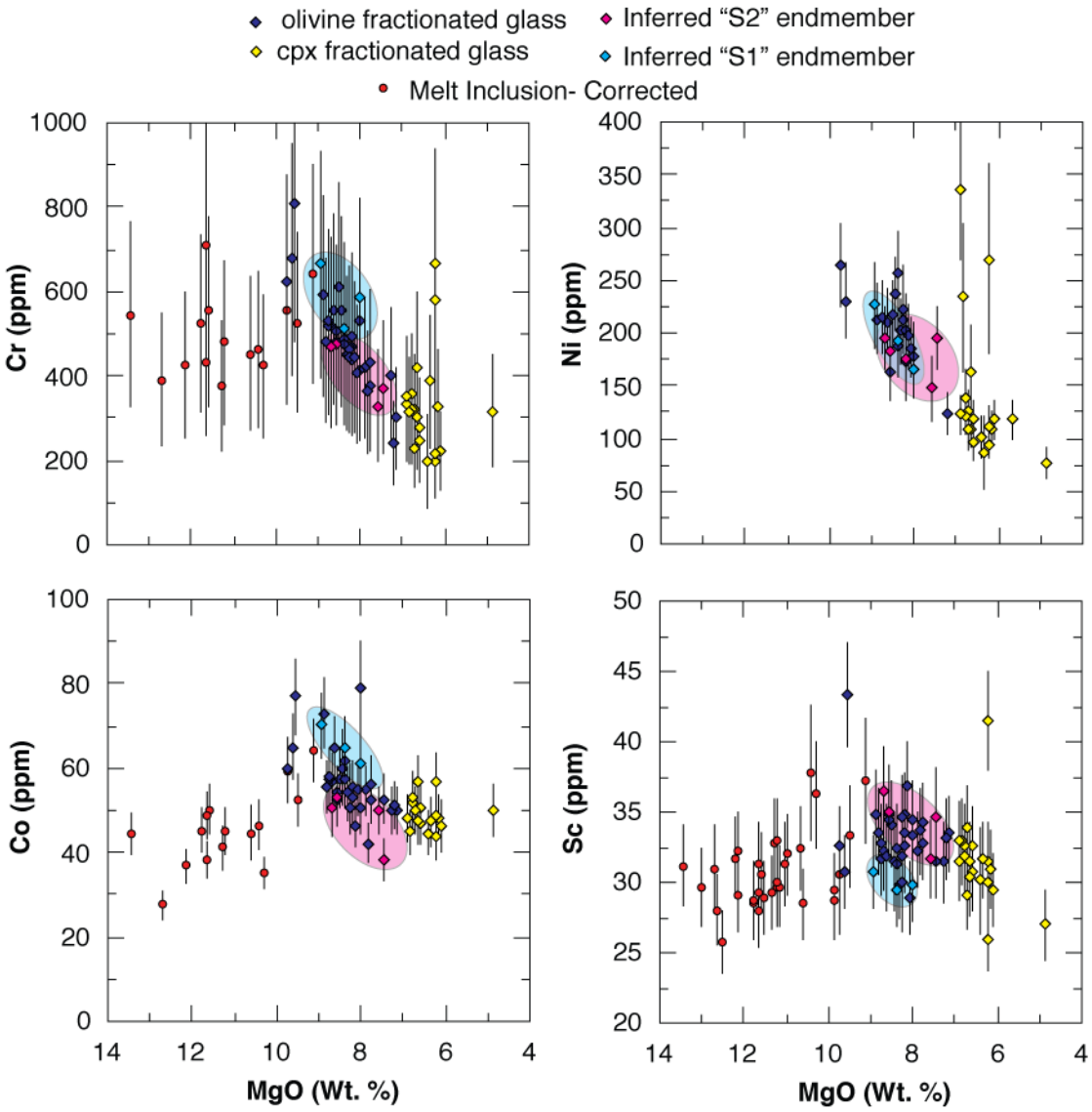

Figure 2.13. Compatible trace element Fenner diagrams show expected behavior. Cr and Co corrections in olivine are lower than expected because these two elements were not analyzed in host olivines and PEC corrections therefore diluted concentrations to unrealistic values. Moderate compatibility of Sc in olivine could explain the fairly flat pattern observed at MgO > 7 wt. %. Error bars are 2 se.

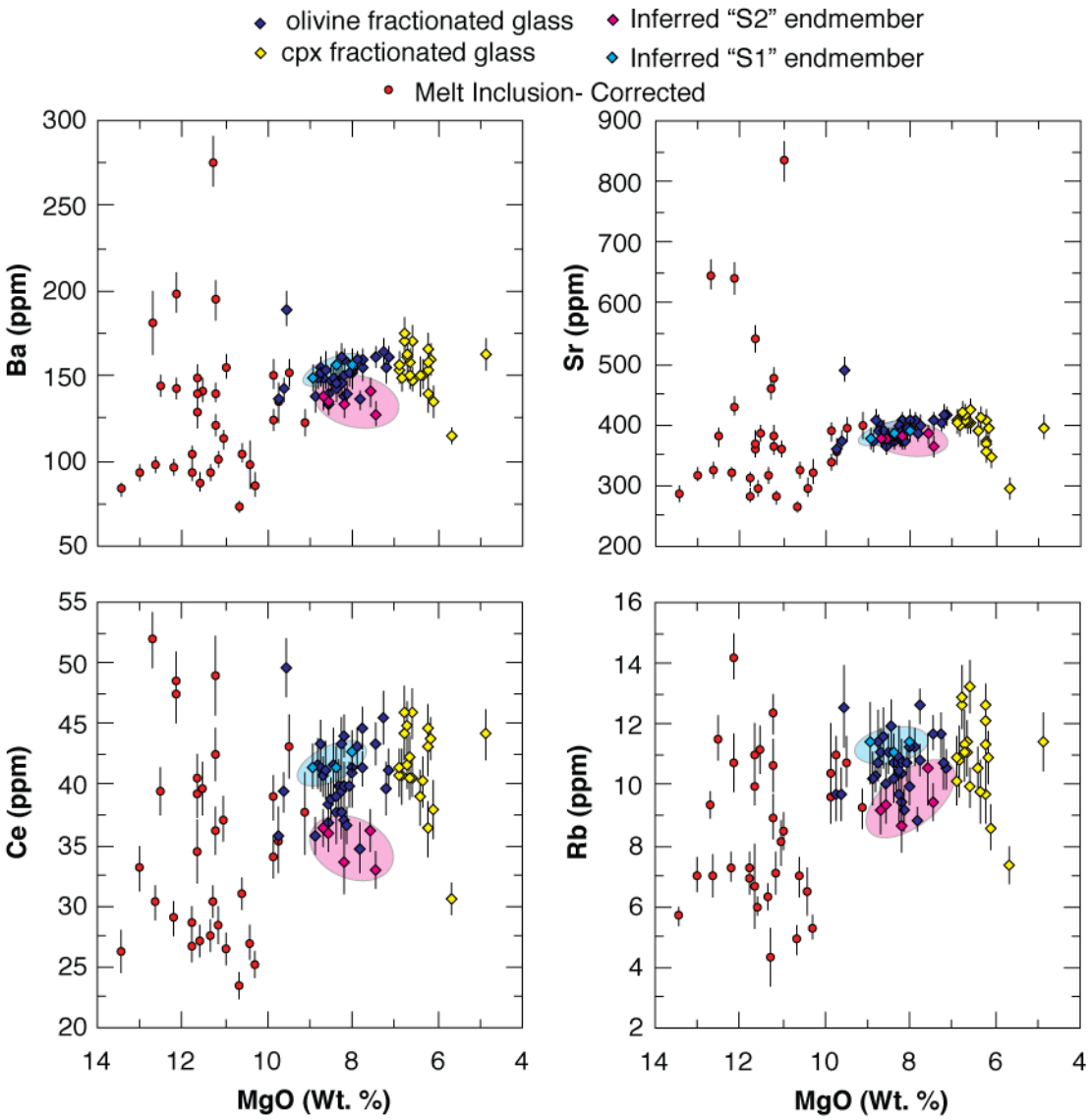

Figure 2.14. Incompatible trace element Fenner diagrams. These do not display the tight correlations as seen in incompatible major elements and are not easily explained by fractionation. Only Sr is more consistent with fractionation increasing until ~7 wt. % MgO. Note, that using the mixing endmembers identified in Figure 12, we can explain most scatter as a combination of mixing and olivine fractionation. Melt inclusions may trap more extreme endmember compositions. Ba, Ce, and Rb are all higher in the S-1 endmember.

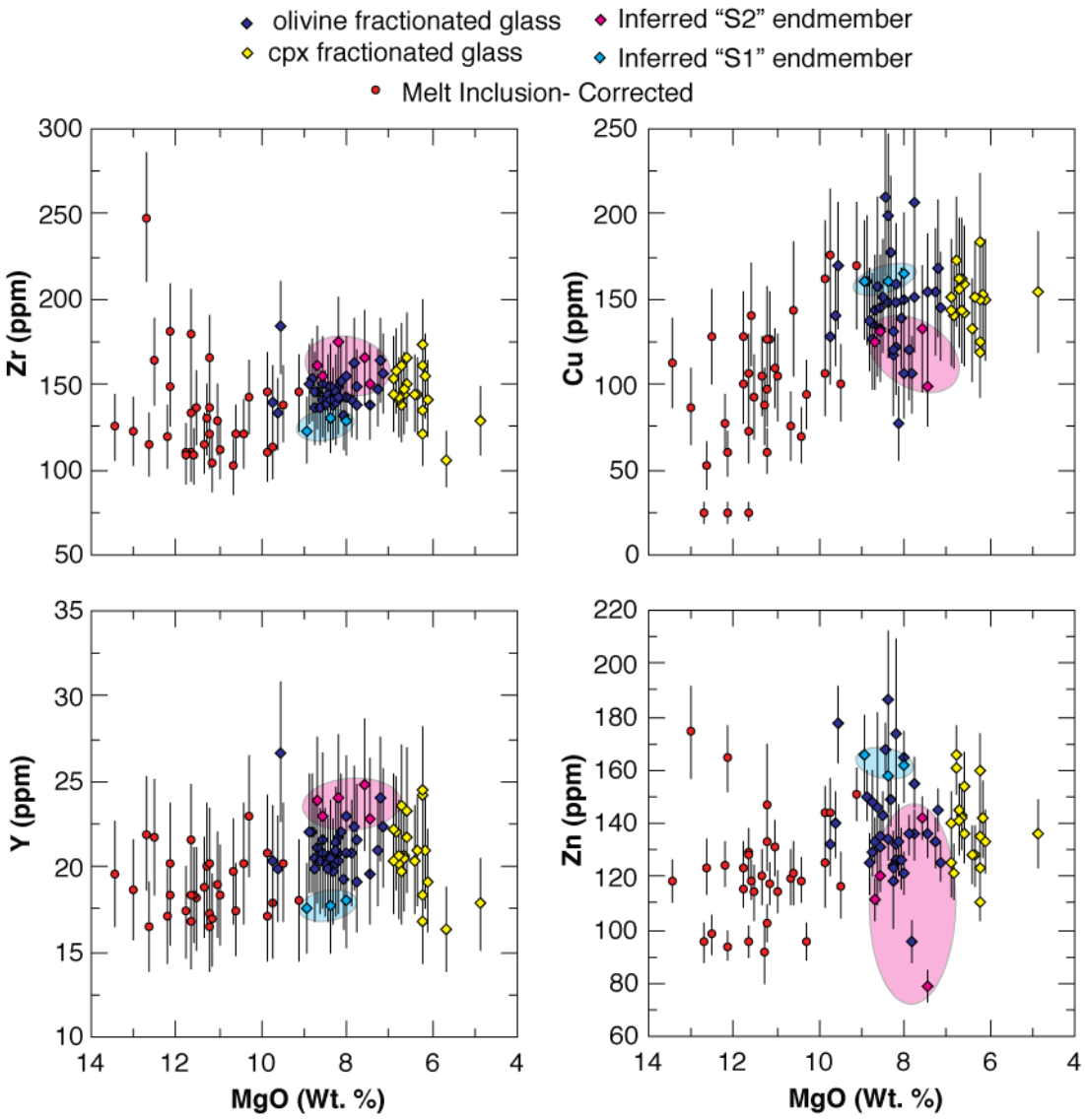

Figure 2.15. Additional trace element Fenner diagrams. These highlight mixing between two endmembers. Zr, Y, and Sc (from Fig. 13) are all compatible in garnet and to a lesser extent in clinopyroxene, are higher in the S-2 endmember while Zn and Cu may be higher in the S-1 endmember. Cu values are high scattered by do not behave volatility as Sulfur does, instead with lower concentrations in melt inclusions suggesting broad enrichment in more evolved matrix glass.

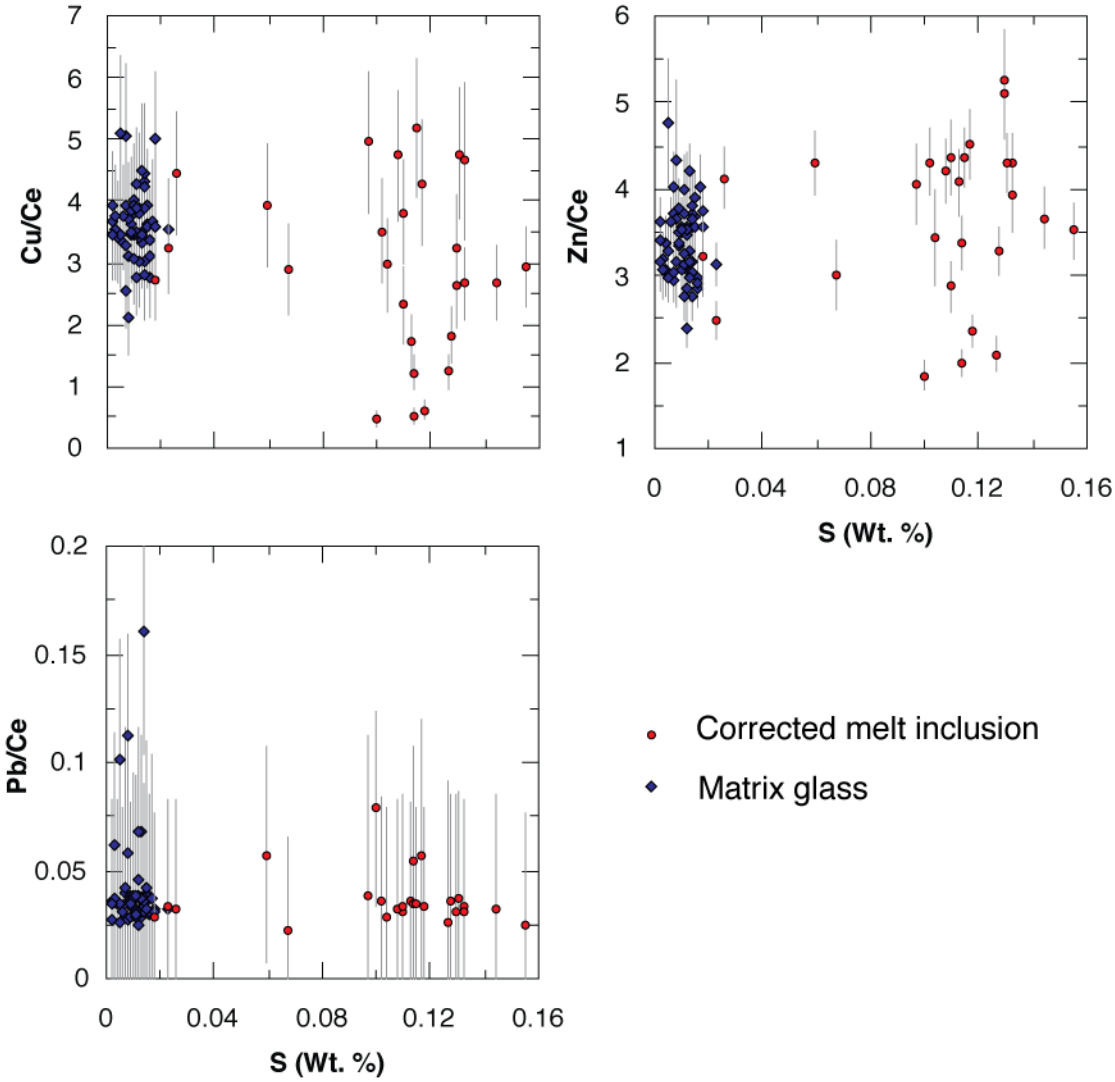

Figure 2.16. Incompatible and semi-volatile element ratios with incompatible and refractory Ce. These plots should separate the effect of fractionation from any volatile behavior. Although sulfur is depleted in matrix glass, no trace metals have any similar signature even accounting for fractionation.

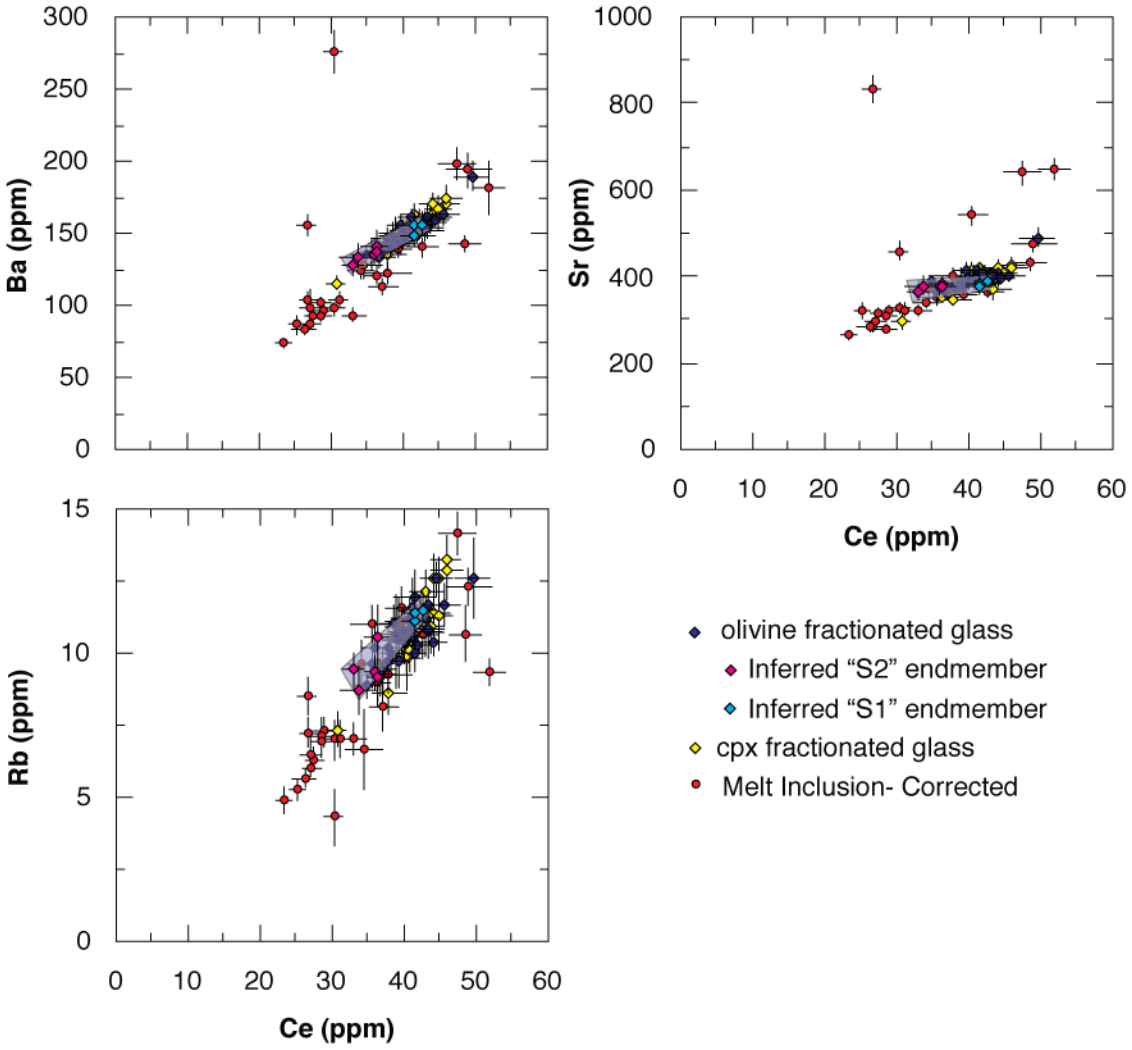

Figure 2.17. Ce variation diagrams show very tight correlation with incompatible trace elements. Since all these elements are higher or equal in the S-1 endmember compared to the S-2 endmember, mixing between the S-1 and S-2 endmembers results in a straight line parallel with a fractionation trend (see shaded purple field).

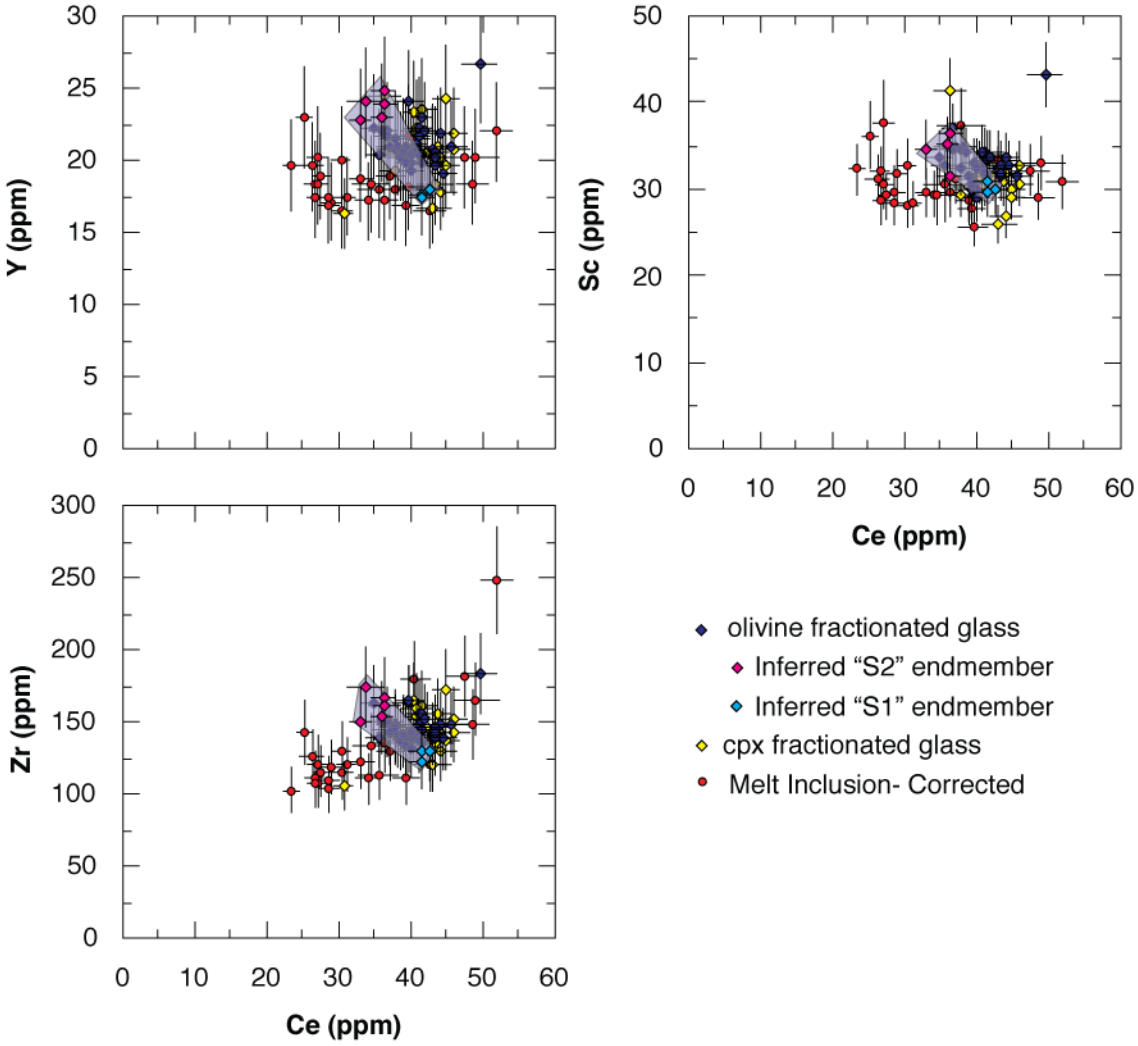

Figure 2.18. Y, Zr, and Sc all poorly correlate with Ce. This pattern is a result of their enrichment in the S-2 endmember while Ce is enriched in the S-1 endmember. As a result, mixing results in increased scatter. If these elements are plotted against each other (e.g., Y vs. Zr) a linear trend is formed as in Fig. 16.

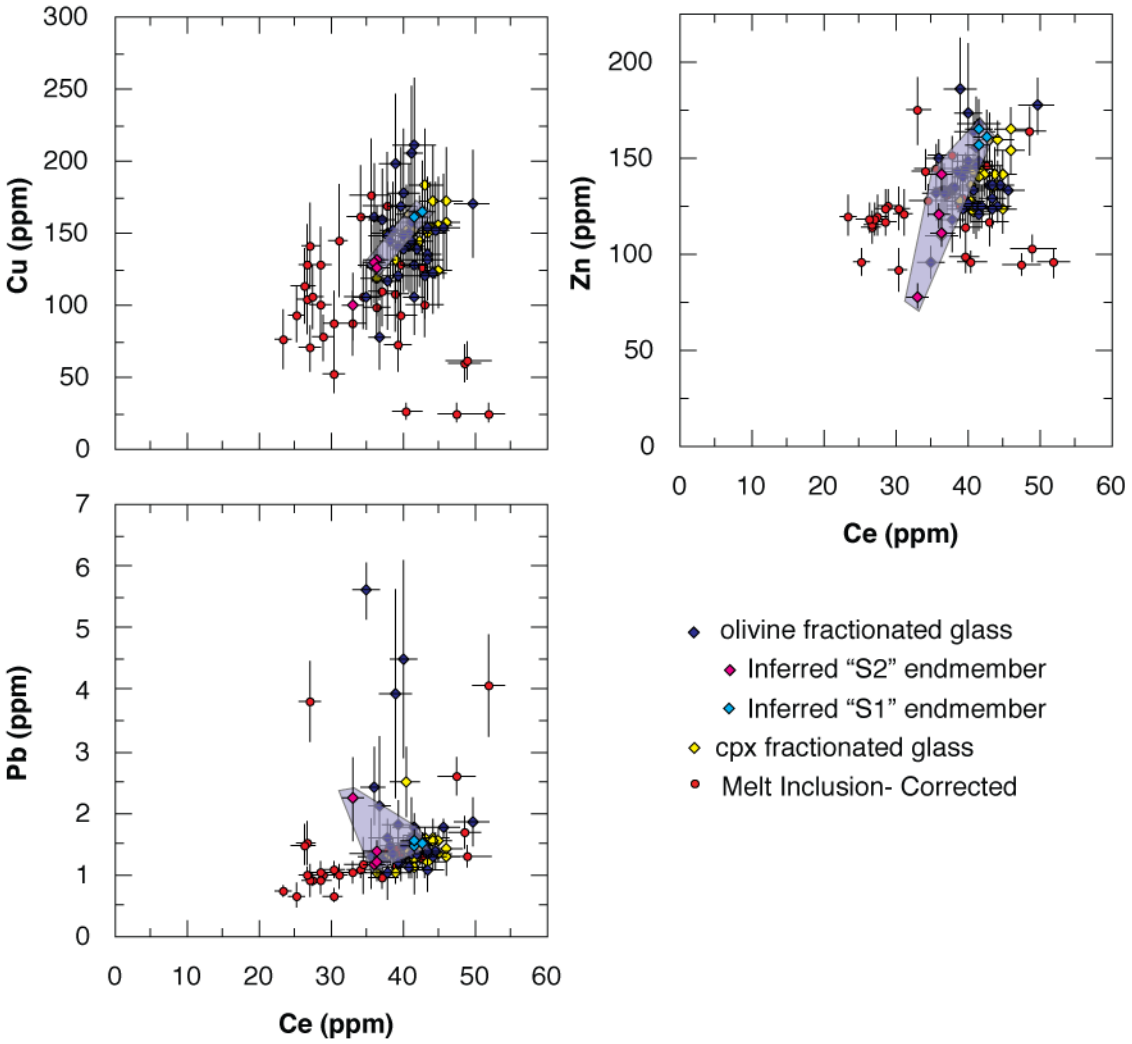

Figure 2.19. Ce variation diagrams with potentially volatile trace elements. These show considerably more scatter than traditional trace elements. In general, this scatter cannot be explained by mixing (Cu) or shallow degassing: the mixing array is parallel to the olivine-control fractionation and there is no difference between degassed matrix glass and undegassed melt inclusions trapped at higher pressures. Variation in Zn easily could be due to moderate compatibility in olivine while variations in Pb can easily be explained by minor assimilation. Cu variability is more difficult to explain, however, removal of very minor amounts of Cu-Ni-Fe sulfides could easily explain any depletions in matrix glass or melt inclusions. Alternatively, some Cu scatter could be due to volatile mobility at high pressure that would not be recorded in compositional differences between the glass and melt inclusions.

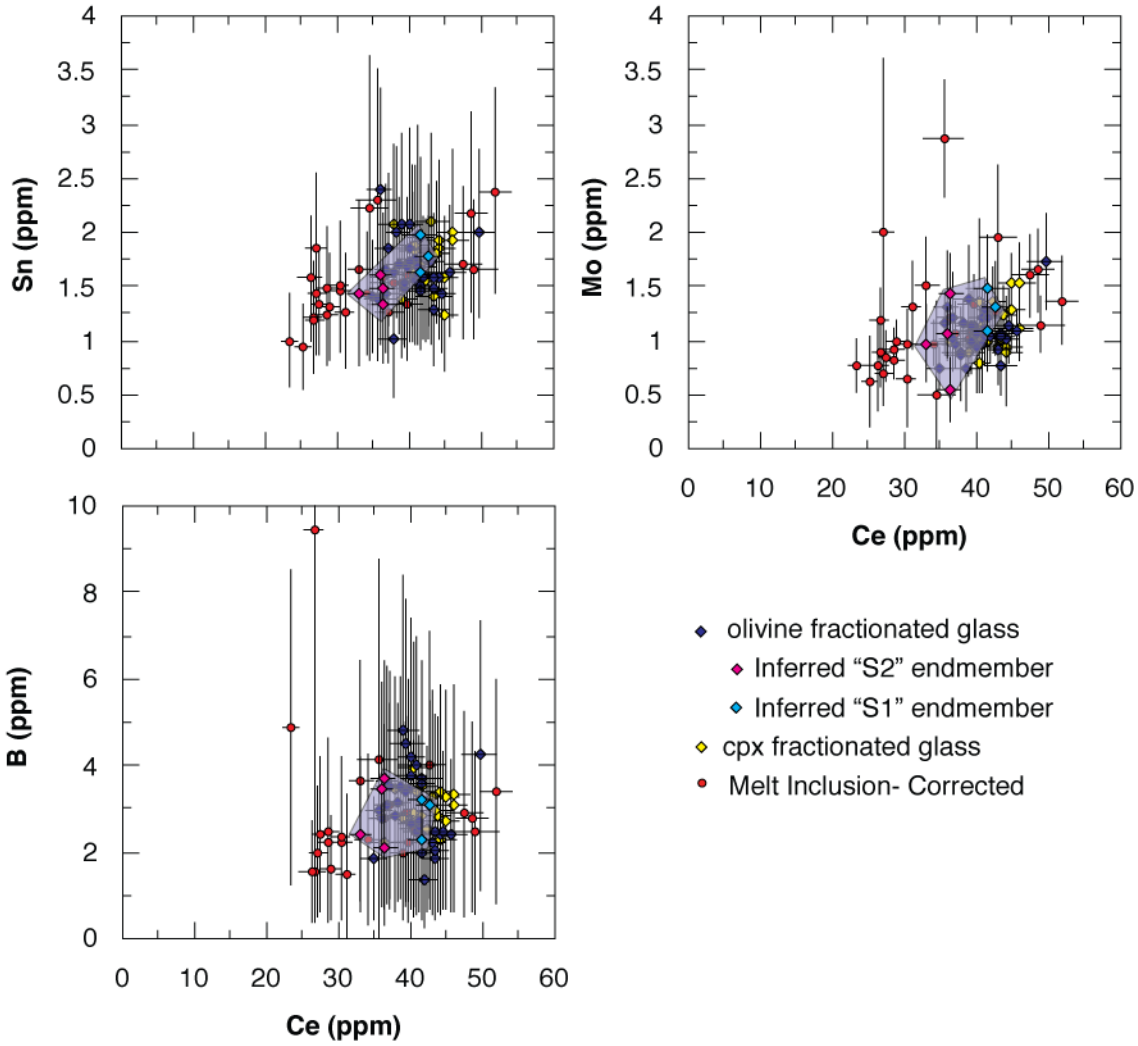

Figure 2.20. Semi-volatile trace elements present at low concentrations. Most semi-volatile elements measured were < 1 ppm complicating any potential to interpret trends, although no obvious differences between melt inclusions and matrix glass were ever observed.

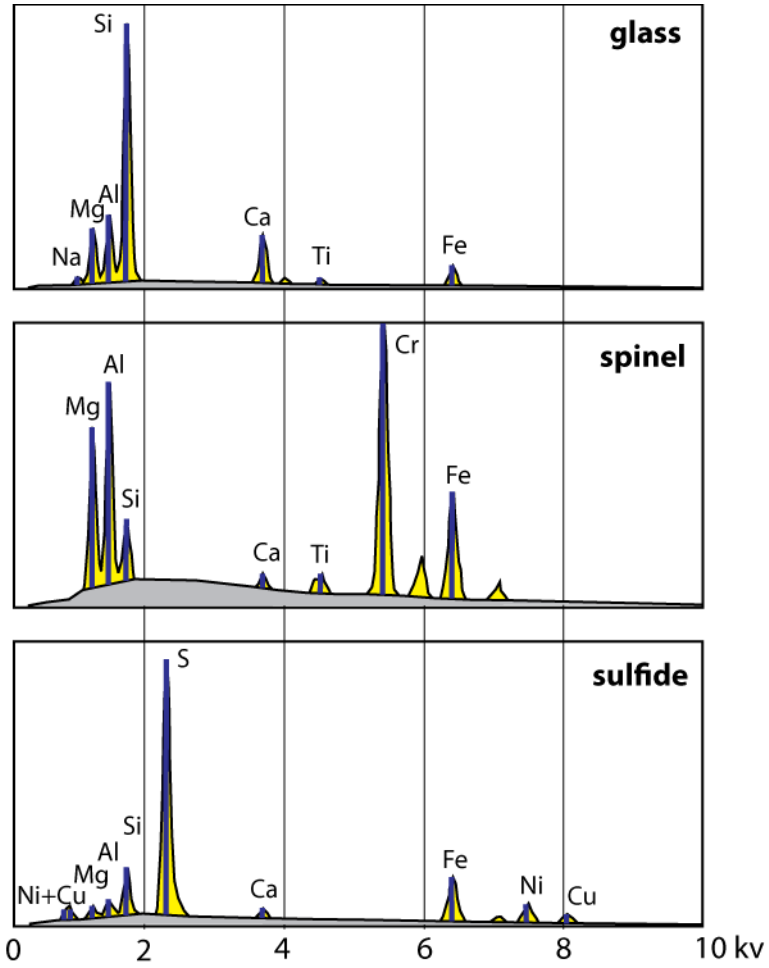

Figure 2.21. EDS (energy dispersive spectroscopy) analysis of glass, spinel, and sulfide from the Iki-22 thin section. Of known phases in the Kilauea Iki eruption, only sulfide significantly partitions Cu.

4. Conclusions

The results of this study provide a useful framework for future work of semi-volatile trace metals in the earth sciences. The work on LA-ICP-MS analysis techniques outlined in Chapter 2 documents the magnitude of analytical uncertainty related to LA-ICP-MS analysis, identifies the primary sources of uncertainty, and documents the suitability of GSE-1G and GSD-1G as calibration standards. The work also highlights the importance of ablation chamber geometry and carrier gas flow characteristics as a control on LA-ICP-MS analysis. Newer ablation systems using two-volume cell geometries should be less susceptible to the within cell fractionations that we observe, although this has not been demonstrated in the literature to date.

Application of the analytical techniques developed in Chapter 2 should be beneficial for studies of shallow crustal processes in magmatic systems. These studies may be especially fruitful in arc environments for the understanding of both volcanic vapor transfer and ore deposits. The addition of more complex volatile species (Cl, H_2O) in arcs and felsic magmas may facilitate complexing and mobility of many trace metals.

The initial study of the 1959 Kilauea Iki both provides a case study for understanding of trace metal behavior in shallow basaltic systems and highlights many complications of the interpretation of trace metal data in these environments. Before attempting to understand potential volatility of trace metals, the fundamental mixing and fractionation controls of a system must be thoroughly documented. Even in well-studied systems, these processes can remain enigmatic. However there is also no clear evidence of loss of semi-volatile metals during the extended shallow degassing that accompanied this eruption.

Future studies should first focus on a broader picture of Ocean Island Basalt evolution of trace metals. Extensive data have already been collected for Loihi seamount and will be combined with geochemical databases to get a worldwide picture of trace metal behavior. These data, together with further studies of oceanic magma systems, can then be used as a base for understanding metal behavior in large igneous provinces and

other tectonic environments. This data will play a key role in understanding the environmental impacts of large igneous provinces.

Bibliography

Anderson Jr, A., and Brown, G., 1993, CO 2 contents and formation pressures of some Kilauean melt inclusions, American Mineralogist, v. 78, p. 794-803.

Asimow P.D., Ghiorso MS, 1998, Algorithmic Modifications Extending MELTS to Calculate Subsolidus Phase Relations, American Mineralogist, Volume 83, p. 1127-1131.

Ault, W., Eaton, J.P., and Richter, D.H., 1961, Lava temperatures in the 1959 Kilauea eruption and cooling lake, Geological Society of America Bulletin, v. 72, p. 791-794.

Baker, D., 2008, The fidelity of melt inclusions as records of melt composition, Contributions to Mineralogy and Petrology, v. 156, p. 377-395.

Bennett, V.C., Norman, M.D., and Garcia, M.O., 2000, Rhenium and platinum group element abundances correlated with mantle source components in Hawaiian picrites: sulphides in the plume, Earth and Planetary Science Letters, v. 183, p. 513-526.

Bleiner, D., and Bogaerts, A., 2007, Computer simulations of sample chambers for laser ablation-inductively coupled plasma spectrometry, Spectrochimica Acta Part B: Atomic Spectroscopy, v. 62, p. 155-168.

Bleiner, D., and Chen, Z., 2008, Computer Modeling of Laser Ablation Elemental Microanalysis, Mineralogical Association of Canada Short Course, v. 40, p. 35-52.

Bleiner, D., and Gunther, D., 2001, Theoretical description and experimental observation of aerosol transport processes in laser ablation inductively coupled plasma mass spectrometry, Journal of Analytical Atomic Spectrometry, v. 16, p. 449-456

Blundy, J.D., and Cashman, K.V., 2005, Rapid decompression-driven crystallization recorded by melt inclusions from Mount St. Helens volcano, Geology, v. 33, p. 793-796.

Borisova, A.Y., Freydier, R., Polve, M., Jochum, K.P., Candaudap, F., 2010, Multi-Elemental Analysis of ATHO-G Rhyolitic Glass (MPI-DING Reference Material) by Femtosecond and Nanosecond LA-ICP-MS: Evidence for Signifcant Heterogeneity of B, V, Zn, Mo, Sn, Sb, Cs, W, Pt and Pb at the Millimetre Scale, Geostandards and Geoanalytical Research, v. 34, p. 245-255.

Candela, P.A., and Holland, H.D., 1986, A mass transfer model for copper and molybdenum in magmatic hydrothermal systems; the origin of porphyry-type ore deposits, Economic Geology, v. 8, p. 1-19.

Clague, D.A., Moore, J.G., Dixon, J.E., and Friesen, W.B., 1995, Petrology of submarine lavas from Kilauea's Puna Ridge, Hawaii, Journal of Petrology, v. 36, p. 299-349.

Clague, D.A., Weber, W.S., and Dixon, J.E., 1991, Picritic glasses from Hawaii, Nature, v. 353, p. 553-556.

Collins, S. J., Pyle, D. M., and Maclennan, J., 2009, Melt inclusions track pre-eruption storage and dehydration of magmas at Etna, Geology, v. 37, p. 571-574.

Cottrell, E., Spiegelman, M., and Langmuir, C.H., 2002, Consequences of diffusive reequilibration for the interpretation of melt inclusions, Geochemistry Geophysics Geosystems, v. 3, 26 p.

Danyushevsky, L.V., Della-Pasqua, F.N., and Sokolov, S., 2000, Re-equilibration of melt inclusions trapped by magnesian olivine phenocrysts from subduction-related magmas: petrological implications, Contribution to Mineralogy and Petrology, v. 138, p. 68-83.

Danyushevsky, L.V., McNeill, A., and Sobolev, A., 2002, Experimental and petrological studies of melt inclusions in phenocrysts from mantle-derived magmas: an overview of techniques, advantages and complications, Chemical Geology, v. 183, p. 5-24.

Durrant, S.F., 1999, Laser ablation inductively coupled plasma mass spectrometry: achievements, problems, prospects, Journal of Analytical Atomic Spectrometry, v.,14, p. 1385-1403.

Eaton, J., and Murata, K., 1960, How volcanoes grow, Science, v. 132, p. 925-938.

Eggins, S., and Shelley, J.M.G., 2002, Compositional heterogeneity in NIST SRM 610-617 glasses, Geostandards Newsletter: The Journal of Geostandards and Geoanalytical Research, v. 26, p. 269-286.

Eggins, S., Kinsley, L., and Shelley, J., 1998, Deposition and element fractionation processes during atmospheric pressure laser sampling for analysis by ICP-MS, Applied Surface Science, v. 127, p. 278-286.

Faure, F., and Schiano, P., 2005, Experimental investigation of equilibration conditions during forsterite growth and melt inclusion formation, Earth and Planetary Science Letters, v. 236, p. 882-898.

Fryer, B., Jackson, S.E., and Longerich, H., 1995, The design, operation and role of the laser-ablation microprobe coupled with an inductively coupled plasma; mass spectrometer (LAM-ICP-MS) in the earth sciences, Canadian Mineralogist, v. 33, p. 303-312.

Gaetani, G.A., and Watson, E.B., 2002, Modeling the major-element evolution of olivine-hosted melt inclusions, Chemical Geology, v. 183, p. 25-41.

Gerlach, T.M., 1986, Exsolution of H2O, CO2, and S During Eruptive Episodes at Kilauea Volcano, Hawaii, Journal of Geophysical Research, v. 91, p. 12177-12185.

Ghiorso, M.S., and Sack, R.O., 1995, Chemical Mass Transfer in Magmatic Processes. IV. A Revised and Internally Consistent Thermodynamic Model for the Interpolation and Extrapolation of Liquid-Solid Equilibria in Magmatic Systems at Elevated Temperatures and Pressures, Contributions to Mineralogy and Petrology, Volume 119, p. 197-212.

Guillong, M., Hametner, K., Reusser, E., Wilson, S.A., and Gunther, D., 2005, Preliminary Characterization of New Glass Reference Materials (GSA-1G, GSC-1G, GSD-1G, GSE-1G) by Laser Ablation-Inductively Coupled Plasma-Mass Spectrometry Using 193 nm, 213 nm and 266 nm Wavelengths, Geostandards and Geoanalytical Research, v. 26, p. 315-331.

Guillong, M., Horn, I., and Gunther, D., 2003, A comparison of 266 nm, 213 nm and 193 nm produced from a single solid state Nd:YAG laser for laser ablation ICP-MS, Journal of Analytical Atomic Spectrometry, v. 18, no. 10, p. 1224-1230.

Günther, D., and Heinrich, C.A., 1999, Comparison of the ablation behaviour of 266 nm Nd: YAG and 193 nm ArF excimer lasers for LA-ICP-MS analysis, Journal of Analytical Atomic Spectrometry, v. 14, p. 1369-1374.

Günther, D., Jackson, S.E., and Longerich, H., 1999, Laser ablation and arc/spark solid sample introduction into inductively coupled plasma mass spectrometers, Spectrochimica Acta Part B: Atomic Spectroscopy, v. 54, p. 381-409.

Helz, R.T., 1987, Diverse olivine types in lava of the 1959 eruption of Kilauea Volcano and their bearing on eruption dynamics, US Geological Survey Professional Paper, v. 1350, p. 691-722.

Hinkley, T., Lamothe, P., Wilson, S.A., Finnegan, D., and Gerlach, T., 1999, Metal emissions from Kilauea, and a suggested revision of the estimated worldwide metal output by quiescent degassing of volcanoes, Earth and Planetary Science Letters, v. 170, p. 315-325.

Hirata, T., and Nesbitt, R., 1995, U-Pb isotope geochronology of zircon: evaluation of the laser probe-inductively coupled plasma mass spectrometry technique, Geochimica et Cosmochimica Acta, v. 59, p. 2491-2500.

Holland, H.D., 1972, Granites, solutions, and base metal deposits, Economic Geology, v. 67, p. 281-301.

Hu, Z., Liu, Y., Chen, L., Zhou, L., Li, M., Zong, K., Zhu, L., and Gao, S., 2011, Contrasting matrix induced elemental fractionation in NIST SRM and rock glasses during laser ablation ICP-MS analysis at high spatial resolution, Journal of Analytical Atomic Spectrometry, v. 26, p. 425-430.

Jackson, S.E., 2001, The Application of Nd:YAG Lasers in LA-ICP-MS, in Laser-ablation-ICPMS in the earth sciences: Principles and applications, p. 29-45.

Jackson, S.E., 2008, Calibration Strategies for Elemental Analysis by LA-ICP-MS, Mineralogical Association of Canada Short Course, v. 40, p. 169-188.

Jenner, F.E., O'neill, H.S.C., Arculus, R.J., and Mavrogenes, J.A., 2010, The Magnetite Crisis in the Evolution of Arc-related Magmas and the Initial Concentration of Au, Ag and Cu, Journal of Petrology, v. 51, p. 2445-2464.

Jochum, K., Nohl, U., Herwig, K., Lammel, E., Stoll, B., and Hofmann, A., 2005, GeoReM: A new geochemical database for reference materials and isotopic standards, Geostandards and Geoanalytical Research, v. 29, p. 333-338.

Kent, A.J.R., 2008, Melt inclusions in basaltic and related volcanic rocks, Reviews in Mineralogy and Geochemistry, v. 69, p. 273-331.

Kent, A.J.R., and Ungerer, C., 2006, Analysis of light lithophile elements (Li, Be, B) by laser ablation ICP-MS: Comparison between magnetic sector and quadrupole ICP-MS, American Mineralogist, v. 91, p. 1401-1411.

Kent, A.J.R., and Ungerer, C.A.A., 2005, Production of barium and light rare earth element oxides during LA-ICP-MS microanalysis, Journal of Analytical Atomic Spectrometry, v. 20, p. 1256-1262.

Kent, A.J.R., Clague, D.A., Honda, M., Stolper, E.M., Hutcheon, I.D., and Norman, M.D., 1999, Widespread assimilation of a seawater-derived component at Loihi Seamount, Hawaii, Geochimica et Cosmochimica Acta, v. 63, p. 2749–2761.

Kent, A.J.R., Norman, M.D., Hutcheon, I.D., and Stolper, E.M., 1999, Assimilation of seawater-derived components in an oceanic volcano: evidence from matrix glasses and glass inclusions from Loihi seamount, Hawaii, Chemical Geology, v.156, p. 299-319.

Kohut, E., and Nielsen, R.L., 2004, Melt inclusion formation mechanisms and compositional effects in high-An feldspar and high-Fo olivine in anhydrous mafic silicate liquids, Contributions to Mineralogy and Petrology, v. 147, p. 684-704.

Lodders, K., 2003, Solar system abundances and condensation temperatures of the elements, The Astrophysical Journal, v. 591, p. 1220-1247.

Longerich, H., 2008, Laser Ablation-Inductively Coupled Plasma- Mass Spectrometry (LA-ICP-MS): An Introduction, Mineralogical Association of Canada Short Course, v. 40, p. 1-18.

Longerich, H., Jackson, S.E., and Günther, D., 1996, Laser ablation inductively coupled plasma mass spectrometric transient signal data acquisition and analyte concentration calculation, Journal of Analytical Atomic Spectrometry, v. 11, p. 899-904.

Lu, F., Anderson Jr, A., and Davis, A., 1995, Diffusional gradients at the crystal/melt interface and their effect on the compositions of melt inclusions, The Journal of Geology, v. 103, p. 591-597.

Mank, A., and Mason, P., 1999, A critical assessment of laser ablation ICP-MS as an analytical tool for depth analysis in silica-based glass samples, Journal of Analytical Atomic Spectrometry, v. 14, p. 1143-1153.

Mathez, E., 1976, Sulfur solubility and magmatic sulfides in submarine basalt glass, Journal of Geophysical Research, v. 81, p. 4269-4276.

McDonough, W.F., and Sun, S., 1995, The composition of the Earth, Chemical Geology, v. 120, p. 223-253.

Milman-Barris, M.S., Beckett, J.R., Baker, M.B., Hofmann, A.E., Morgan, Z., Crowley, M.R., Vielzeuf, D., and Stolpher, E.M., 2008, Zoning of phosphorous in igneous olivine, Contributions to Mineralogy and Petrology, v. 155, p. 739-765.

Müller, W., Shelley, M., Miller, P., and Broude, S., 2009, Initial performance metrics of a new custom-designed ArF excimer LA-ICPMS system coupled to a two-volume laser-ablation cell, Journal of Analytical Atomic Spectrometry, v. 24, p. 209-214.

Murata, K., and Richter, D.H., 1966a, Chemistry of the Lavas of the 1959-60 Eruption of Kilauea Volcano, Hawaii, US Geological Survey Professional Paper, v. 537-A, p. 1-26.

Murata, K., and Richter, D.H., 1966b, The settling of olivine in Kilauean magma as shown by lavas of the 1959 eruption, American Journal of Science, v. 264, p. 194-203.

Nielsen, R.L., Michael, P.J., and Sours-Page, R., 1998, Chemical and physical indicators of compromised melt inclusions, Geochimica et Cosmochimica Acta, v. 62, p. 831-839.

Norman, M.D., Garcia, M.O., and Bennett, V.C., 2004, Rhenium and chalcophile elements in basaltic glasses from Ko'olau and Moloka'i volcanoes: Magmatic outgassing and composition of the Hawaiian plume, Geochimica et Cosmochimica Acta, v. 68, p. 3761-3777.

Outridge, P., Doherty, W., and Gregoire, D., 1997, Ablative and transport fractionation of trace elements during laser sampling of glass and copper, Spectrochimica Acta Part B: Atomic Spectroscopy, v. 52, p. 2093-2102.

Pitcher, L., Helz, R.T., Walker, R.J., and Piccoli, P.M., 2009, Fractionation of the platinum-group elements and Re during crystallization of basalt in Kilauea Iki Lava Lake, Hawaii, Chemical Geology, v. 260, p. 196-210.

Pokrovski, G.S., Roux, J., and Harrichoury, J.C., 2005, Fluid density control on vapor-liquid partitioning of metals in hydrothermal systems, Geology, v. 33, p. 657-660.

Putirka, K., Perfit, M., Ryerson, F., and Jackson, M., 2007, Ambient and excess mantle temperatures, olivine thermometry, and active vs. passive upwelling, Chemical Geology, v. 241, p. 177-206.

Richter, D.H., and Murata, K., 1966, Petrography of the Lavas of the 1959-60 Eruption of Kilauea Volcano, Hawaii, US Geological Survey Professional Paper, v. 537-D, p. 1-12.

Richter, D.H., Eaton, J.P., Murata, K., Ault, W., and Krivoy, H.L., 1970, Chronological Narrative of the 1959-60 Eruption of Kilauea Volcano, Hawaii, US Geological Survey Professional Paper, v. 537-E, p. 1-73.

Roedder, E., 1979, Origin and significance of magmatic inlcuions, Bulletin of Mineralogy, v. 102, p. 487-510.

Roedder, E., 1984, Fluid Inclusions, Reviews in Mineralogy, v. 12, p. 1-644.

Rowe, M.C., Kent, A.J.R, and Thornber, C.R., 2008, Using amphibole phenocrysts to track vapor transfer during magma crystallization and transport: An example from Mount St. Helens, Washington, Journal of Volcanology and Geothermal Research, v. 178, p. 593-607.

Rubin, K., 1997, Degassing of metals and metalloids from erupting seamount and mid-ocean ridge volcanoes: Observations and predictions, Geochimica et Cosmochimica Acta, v. 61, p. 3525-3542.

Russo, R., Mao, X., Borisov, O., and Liu, H., 2000, Influence of wavelength on fractionation in laser ablation ICP-MS, Journal of Analytical Atomic Spectrometry, v. 15, p. 1115-1120.

Schiano, P., 2003, Primitive mantle magmas recorded as silicate melt inclusions in igneous minerals, Earth Science Reviews, v. 63, p. 121-144.

Simon, A., Pettke, T., Candela, P.A., Piccoli, P.M., and Heinrich, C.A., 2006, Copper partitioning in a melt-vapor-brine-magnetite-pyrrhotite assemblage, Geochimica et Cosmochimica Acta, v. 70, p. 5583-5600.

Sinton, C.W., and Duncan, R.A., 1997, Potential links between ocean plateau volcanism and global ocean anoxia at the Cenomanian-Turonian boundary, Economic Geology, v. 92, p. 836-842.

Stone, W.B., and Fleet, M.E., 1991, Nickel-copper sulfides from the 1959 eruption of Kilauea Volcano, Hawaii: Contrasting compositions and phase relations in eruption pumice and Kilauea Iki lava lake, American Mineralogist, v. 76, p. 1363-1372.

Sun, W., Bennett, V.C., Eggins, S., Arculus, R., and Perfit, M., 2003, Rhenium systematics in submarine MORB and back-arc basin glasses: laser ablation ICP-MS results, Chemical Geology, v. 196, p. 259-281.

Sylvester, P. J., 2008, Matrix Effects in Laser Ablation-ICP-MS, Mineralogical Association of Canada Short Course, v. 40, p. 67-78.

Tilling, R.I., Wright, T.L., and Millard, H.T., 1987, Trace-element chemistry of Kilauea and Mauna Loa lava in space and time: A reconnaissance, US Geological Survey Professional Paper, v. 1350, p. 641-689.

Wallace, P.J., and Anderson Jr, A., 1998, Effects of eruption and lava drainback on the H 2 O contents of basaltic magmas at Kilauea Volcano, Bulletin of Volcanology, v. 59, p. 327-344.

Wallace, P.J., and Carmichael, I., 1992, Sulfur in basaltic magmas, Geochimica et Cosmochimica Acta, v. 56, p. 1863-1874.

Williams, T.J., Candela, P.A., and Piccoli, P.M., 1995, The partitioning of copper between silicate melts and two-phase aqueous fluids: an experimental investigation at 1 kbar, 800 C and 0.5 kbar, 850 C, Contributions to Mineralogy and Petrology, v. 121, p. 388-399.

Winter, J.D., 2001, An Introduction to Igneous and Metamorphic Petrology. Prentice-Hall Inc, Upper Saddle River, New Jersey, 697.

Witt-Eickschen, G., Palme, H., O'Neill, H.S.C., and Allen, C.M., 2009, The geochemistry of the volatile trace elements As, Cd, Ga, In and Sn in the Earth's mantle: New evidence from in situ analyses of mantle xenoliths, Geochimica et Cosmochimica Acta, v. 73, p. 1755-1778.

Wright, T.L., 1973, Magma mixing as illustrated by the 1959 eruption, Kilauea volcano, Hawaii, Geological Society of America Bulletin, v. 84, p. 849-858.

Wright, T.L., and Fiske, R.S., 1971, Origin of the differentiated and hybrid lavas of Kilauea volcano, Hawaii, Journal of Petrology, v. 12, p. 1-65.

Yu, Z., Norman, M.D., and Robinson, P., 2003, Major and trace element analysis of silicate rocks by XRF and laser ablation ICP-MS using lithium borate fused glasses: Matrix effects, instrument response and results for international reference materials, Geostandards Newsletter: The Journal of Geostandards and Geoanalytical Research, v. 27, p. 67-89.

Zajacz, Z., and Halter, W., 2009, Copper transport by high temperature, sulfur-rich magmatic vapor: Evidence from silicate melt and vapor inclusions in a basaltic andesite from the Villarrica volcano (Chile), Earth and Planetary Science Letters, v. 282, p. 115-121.

APPENDICES

A. Detection limit calculations for LA-ICP-MS

Variable spot sizes (50, 80, 100, and 160 μm) were measured on GSE-1G, BCR-2G, and BHVO-2G to determine detection limits for selected volatile trace metals. The lower limit of detection (LLD) was calculated using analyses of GSE-1G, BHVO-2G, and BCR-2G (3 spots each) and the method of Perkins and Pearce (1995) where,

(1) LLD= 3*sqrt(2B)*(C/I),

where B is the background count rate, C is the concentration in the standard, and I is the peak intensity count rate.

Clear decreases in LLD were observed with increasing spot size (Table 7, Fig. 10). In most cases, the LLD was <1 ppm, however, in practice relative analytical precision deteriorates significantly when concentrations are <10-20 ppm. The LLD calculation is only approximate, and depends on the concentration in the material being ablated and in practice needs to be calculated for each individual analysis (Longerich *et al*., 1996). In these calculations, however, it is clear that the LLD is consistently decreased with increasing spot size (and therefore sample volume).

Table A1. Calculated lower limit of detection (ppm)* for different spot sizes (μm).

Mass	GSE-1G				BCR-2G				BHVO-2G			
	50	80	100	160	50	80	100	160	50	80	100	160
11B	0.60	0.27	0.21	0.14	0.74	0.44	0.41	0.24				
29Si	0.02	0.01	0.01	0.00	0.02	0.01	0.01	0.00	0.02	0.01	0.01	0.00
43Ca	0.01	0.00	0.00	0.00	0.01	0.00	0.00	0.00	0.01	0.01	0.01	0.00
45Sc	0.32	0.14	0.11	0.08	0.32	0.16	0.14	0.08	0.26	0.13	0.11	0.07
47Ti	0.00	0.00	0.00	0.00	1.14	0.69	0.50	0.34	1.48	1.11	0.76	0.56
51V	0.05	0.02	0.02	0.02	0.05	0.03	0.03	0.02	0.04	0.03	0.02	0.01
52Cr	0.98	0.42	0.36	0.24	0.05	0.02	0.02	0.01	6.18	4.08	3.71	2.66
53Cr	1.14	0.49	0.43	0.26	0.06	0.02	0.02	0.01	15.95	8.47	6.50	4.27
55Mn	0.24	0.10	0.09	0.06	0.24	0.11	0.08	0.05	0.00	0.00	0.00	0.00
57Fe	0.00	0.00	0.00	0.00	0.00	0.00	0.00	0.00	0.00	0.00	0.00	0.00
59Co	0.19	0.08	0.07	0.04	0.14	0.06	0.06	0.03	0.22	0.10	0.09	0.05
60Ni	2.14	0.93	0.78	0.48	0.17	0.09	0.08	0.05	5.25	4.01	3.76	2.97
65Cu	0.47	0.22	0.18	0.11	0.07	0.03	0.03	0.02	3.19	1.48	1.25	0.73
66Zn	0.17	0.08	0.07	0.05	0.17	0.08	0.08	0.05	0.12	0.07	0.05	0.03
75As	0.31	0.13	0.11	0.07								
85Rb	0.10	0.04	0.03	0.02	0.44	0.22	0.17	0.08	0.02	0.01	0.01	0.00
88Sr	0.04	0.01	0.02	0.01	0.04	0.02	0.02	0.01	0.05	0.04	0.02	0.02
89Y	0.02	0.01	0.01	0.01	0.06	0.03	0.02	0.02	0.02	0.01	0.01	0.00
90Zr	0.07	0.04	0.03	0.02	0.13	0.07	0.06	0.03	0.09	0.06	0.03	0.02
95Mo	0.10	0.06	0.05	0.04	7.62	2.30	2.55	1.23	0.00	0.00	0.00	0.00
98Mo	0.14	0.07	0.05	0.04	6.76	3.29	3.98	2.33	0.00	0.00	0.00	0.00
107Ag	0.02	0.02	0.01	0.01	0.05	0.01	0.02	0.01				
111Cd	0.07	0.05	0.03	0.02	0.08	0.05	0.05	0.03	0.13	0.02	0.02	0.01
115In	0.02	0.01	0.01	0.01	0.01	0.01	0.01	0.00	0.01	0.01	0.00	0.00
118Sn	0.11	0.05	0.04	0.03	0.15	0.07	0.06	0.04	0.13	0.07	0.06	0.03
121Sb	0.03	0.02	0.02	0.02	0.10	0.06	0.04	0.02	0.03	0.01	0.01	0.01
125Te												
137Ba	0.24	0.08	0.07	0.05	0.97	0.63	0.44	0.30	0.04	0.02	0.02	0.01
139La	0.02	0.01	0.01	0.01	0.03	0.02	0.02	0.01	0.01	0.01	0.01	0.00
140Ce	0.02	0.01	0.01	0.01	0.02	0.02	0.01	0.01	0.01	0.01	0.00	0.00
182W	0.06	0.03	0.02	0.02	0.17	0.04	0.05	0.04	0.03	0.01	0.01	0.01
185Re	0.05	0.02	0.02	0.01	bdl	bdl	bdl	bdl	bdl	bdl	0.00	0.00
193Ir	0.29	0.06	0.03	0.03								
197Au	0.03	0.01	0.01	0.01								
208Pb	0.03	0.02	0.02	0.01	0.18	0.10	0.06	0.05	0.01	0.00	0.00	0.00
209Bi	0.02	0.01	0.01	0.01	0.05	0.02	0.02	0.01	0.00	0.00	0.00	0.00
205Tl	0.02	0.01	0.01	0.00	0.36	0.15	0.09	0.06				

*Based on method of Perkins and Pearce (1995), reported as ppm except for Ca, Fe, and GSE-1G for Ti, which are in oxide wt. %. Blank values have no reported standard concentration to make calculation with.

B. Additional fractionation tests

Fractionation was also calculated while operating the laser at two different fluence energies (135 mJ and 190 mJ) for 120 second ablation intervals on GSD-1G and NIST-612. No significant differences in fractionation trends were observed between the two energies. In these tests, however, fractionation values were consistently higher for GSD-1G over NIST-612. Refractory lithophile elements including Ca, Sc, Ti, Ba, Zr, Y, Sr, Mg, and Ce had indices <1.1 in NIST-612. Cd and Zn fractionated more than in the GSE-1G test. Ablation depths were decreased slightly at the lower energy level (53 to 50 μm in GSD-1G, 68 to 63 μm in NIST-612).

Other fractionation tests show large variability. Fractionation over 30 second intervals (comparing the first and third 10 second intervals of ablation) is similar to 120 second intervals overall in once case.

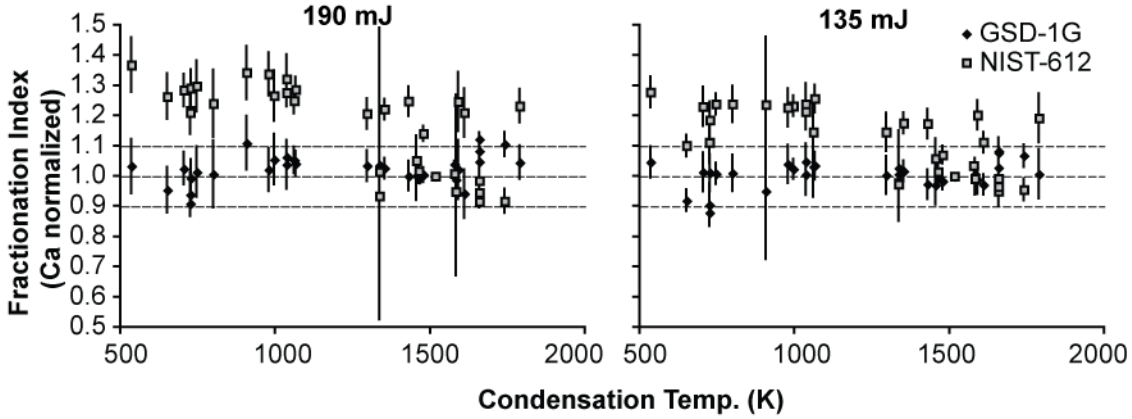

Figure B1. Results of 120 second fractionation tests at 2 different laser energy levels. In these tests, NIST-612 (likely in the sidemount position) had significantly higher fractionation indices. There was no significant difference, however, between the two energy levels.

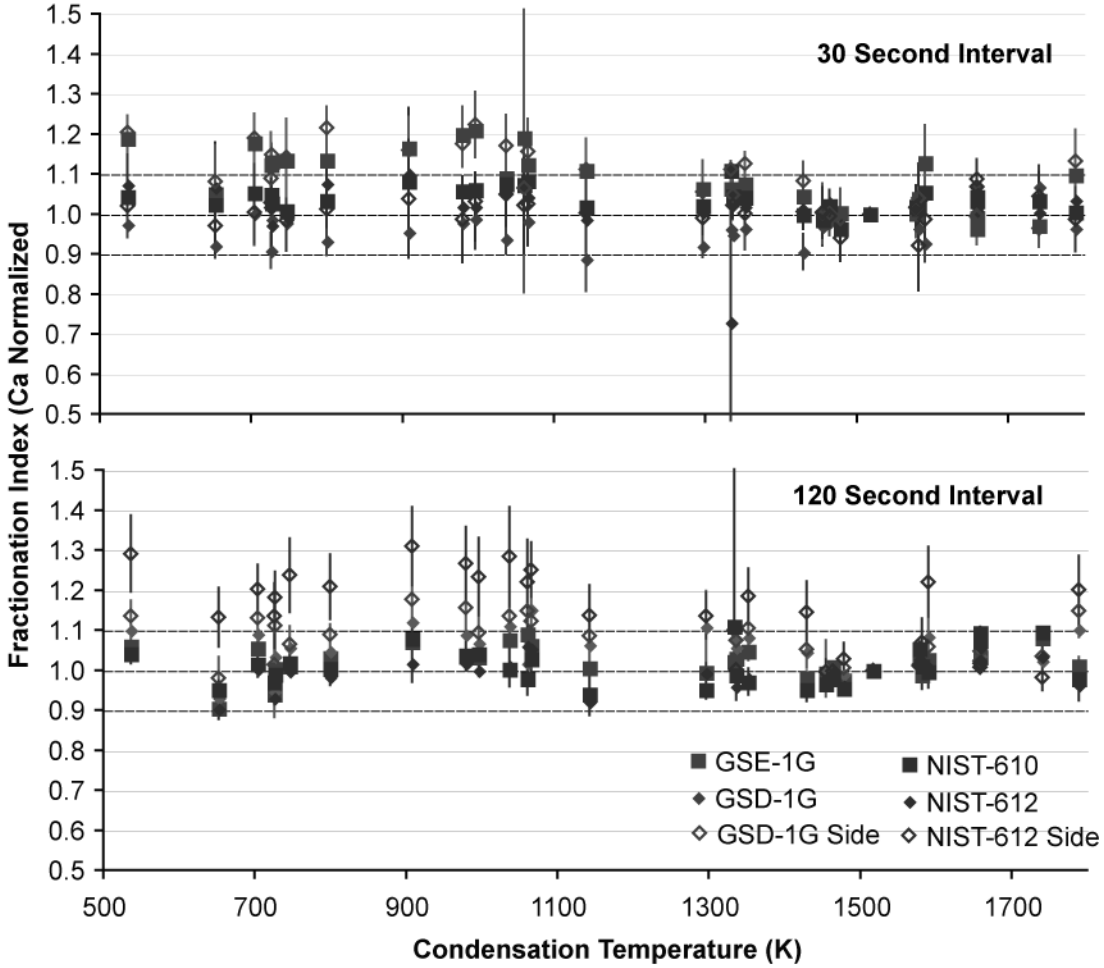

Figure B2. Comparison of all fractionation tests from 120 second and 30 second intervals. In both tests, fractionation values are generally low for most standards. Increased values in GSE-1G in the 30 second interval could largely be due to increased uncertainty when measuring small (10 second) intervals of ablation. Seeing all data in the 120 second interval shows that the GSD-1G sidemount is not nearly as fractionated as the NIST-612 sidemount. The NIST sidemount was directly under the He input, possibly resulting in lower flow while the rightmost sidemount may have fairly similar He pressures as the rest of the epoxy round.

C. Additional data on GSE-1G Transects

This section includes complete data from the GSE-1G transects which detected anomalies near cracks or fractures in the glass. Reflected light images of both the GSE-1G chips used for transects and the GSD-1G chip are also presented.

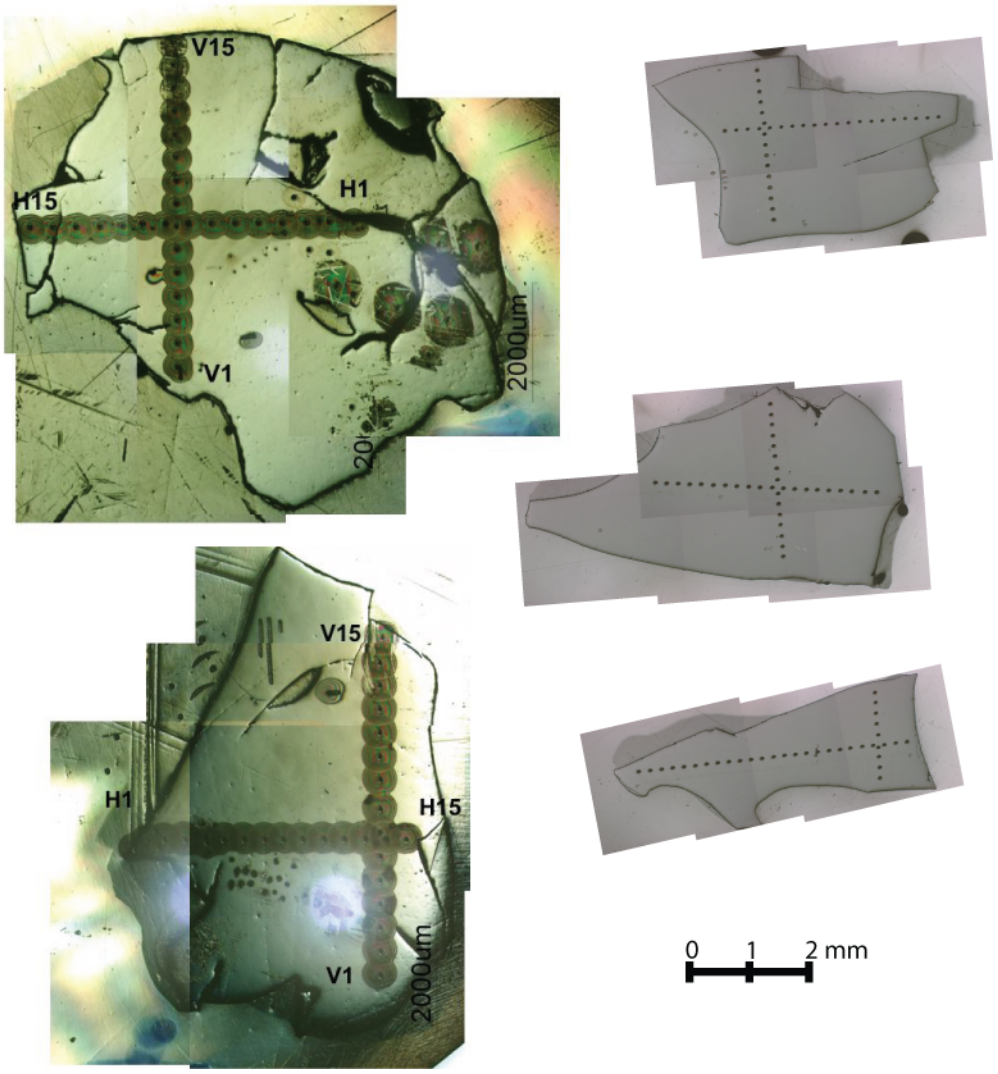

Figure C1. Reflected light image of standard chips after transect ablations. GSD-1G is on the bottom left while the large chip of GSE-1G used for dense transects is on the top left (note: the second overlapping set of ablations on GSE-1G has not been completed in this picture). The three chips on the right were used for sample chamber analysis.

Figure C2. Results for all analyzed isotopes from the GSE-1G dense transect. Figures includes the following seven pages. Symbols represent different transects while error bars are 2 se for each spot analysis.

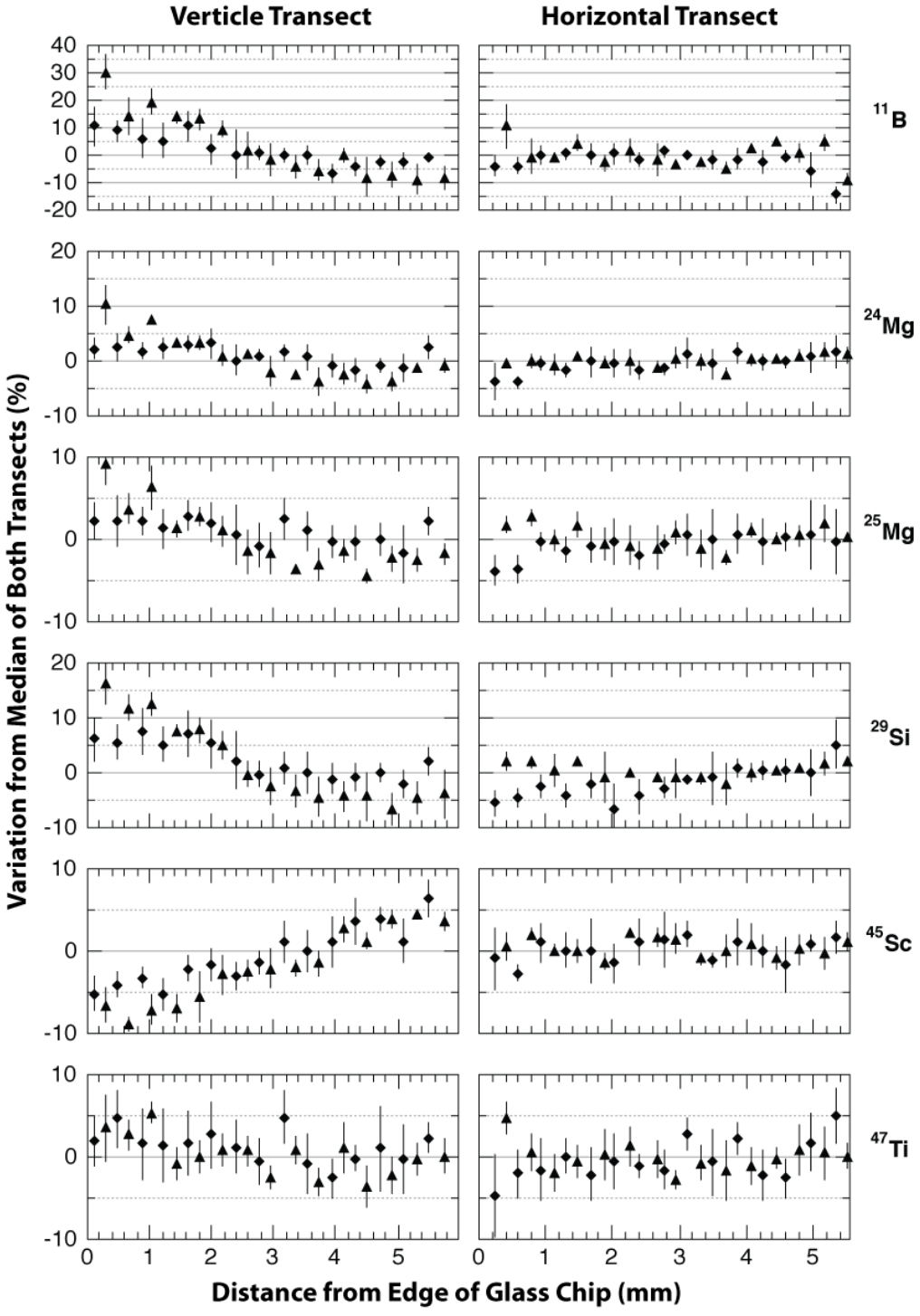
Verticle Transect
Horizontal Transect
Variation from Median of Both Transects (%)
Distance from Edge of Glass Chip (mm)
11B
24Mg
25Mg
29Si
45Sc
47Ti

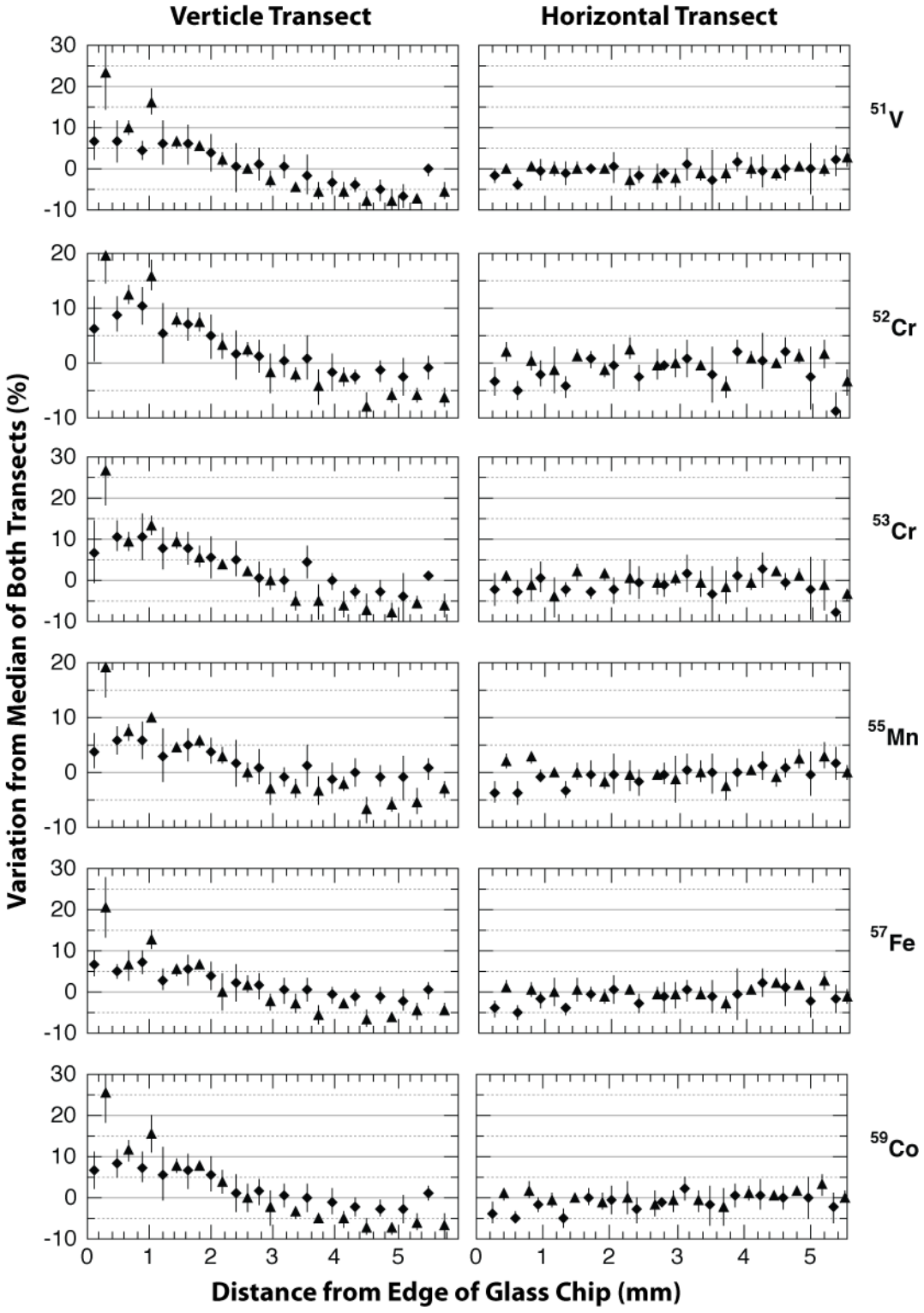
Verticle Transect
Horizontal Transect
Variation from Median of Both Transects (%)
Distance from Edge of Glass Chip (mm)
51V
52Cr
53Cr
55Mn
57Fe
59Co

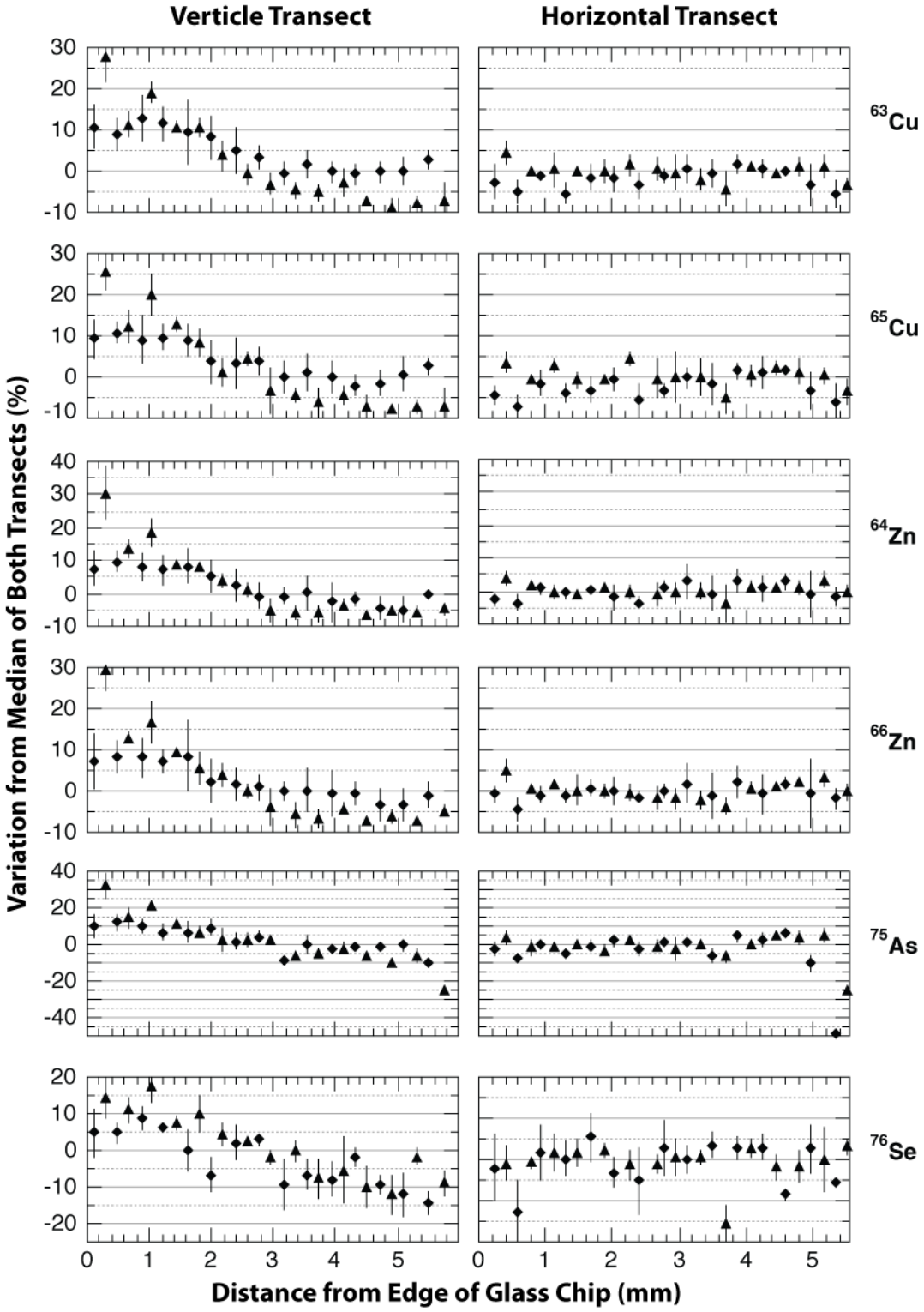
Verticle Transect
Horizontal Transect
Variation from Median of Both Transects (%)
63Cu
65Cu
64Zn
66Zn
75As
76Se
Distance from Edge of Glass Chip (mm)

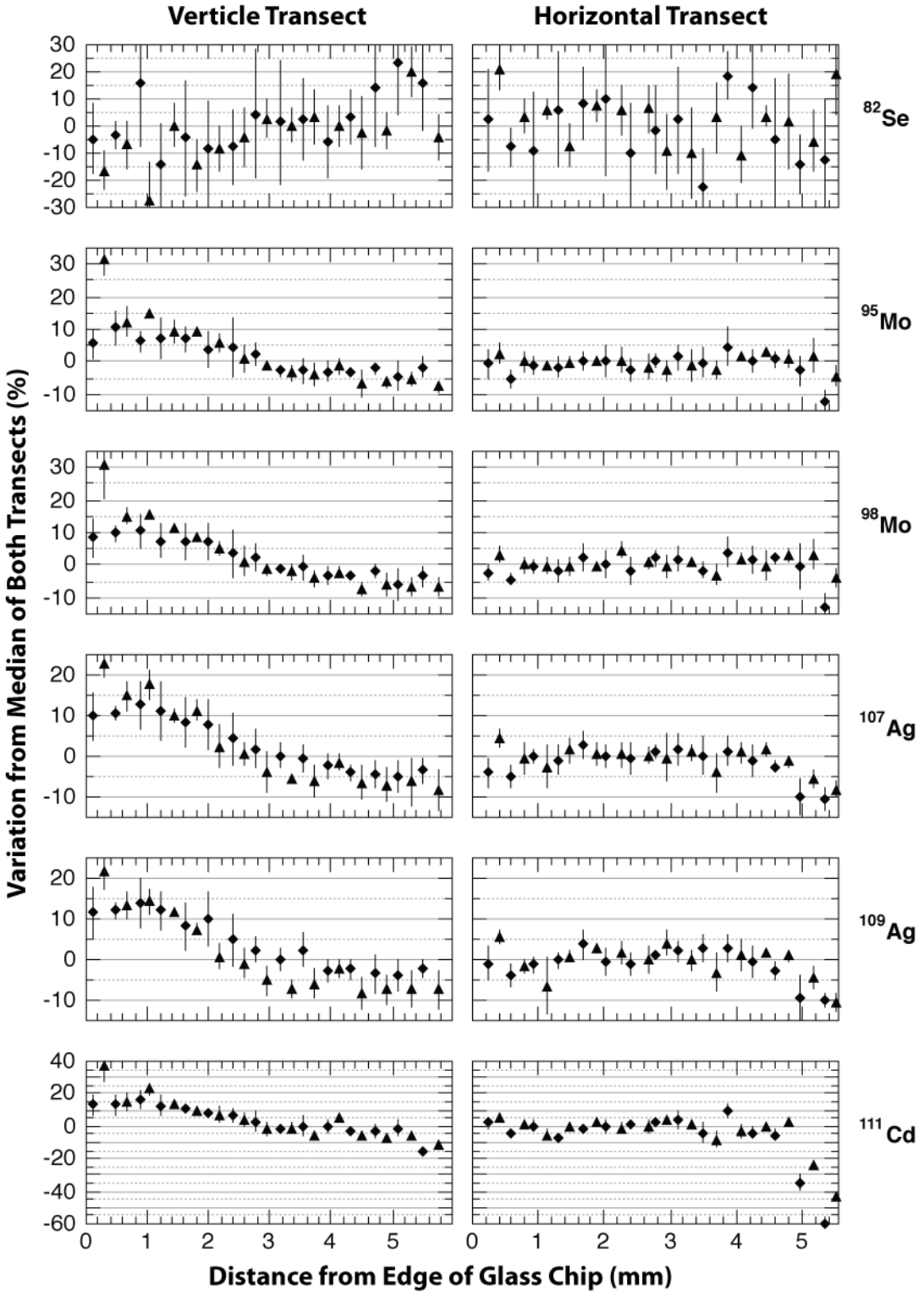
Verticle Transect
Horizontal Transect
82Se
95Mo
98Mo
107Ag
109Ag
111Cd
Variation from Median of Both Transects (%)
Distance from Edge of Glass Chip (mm)

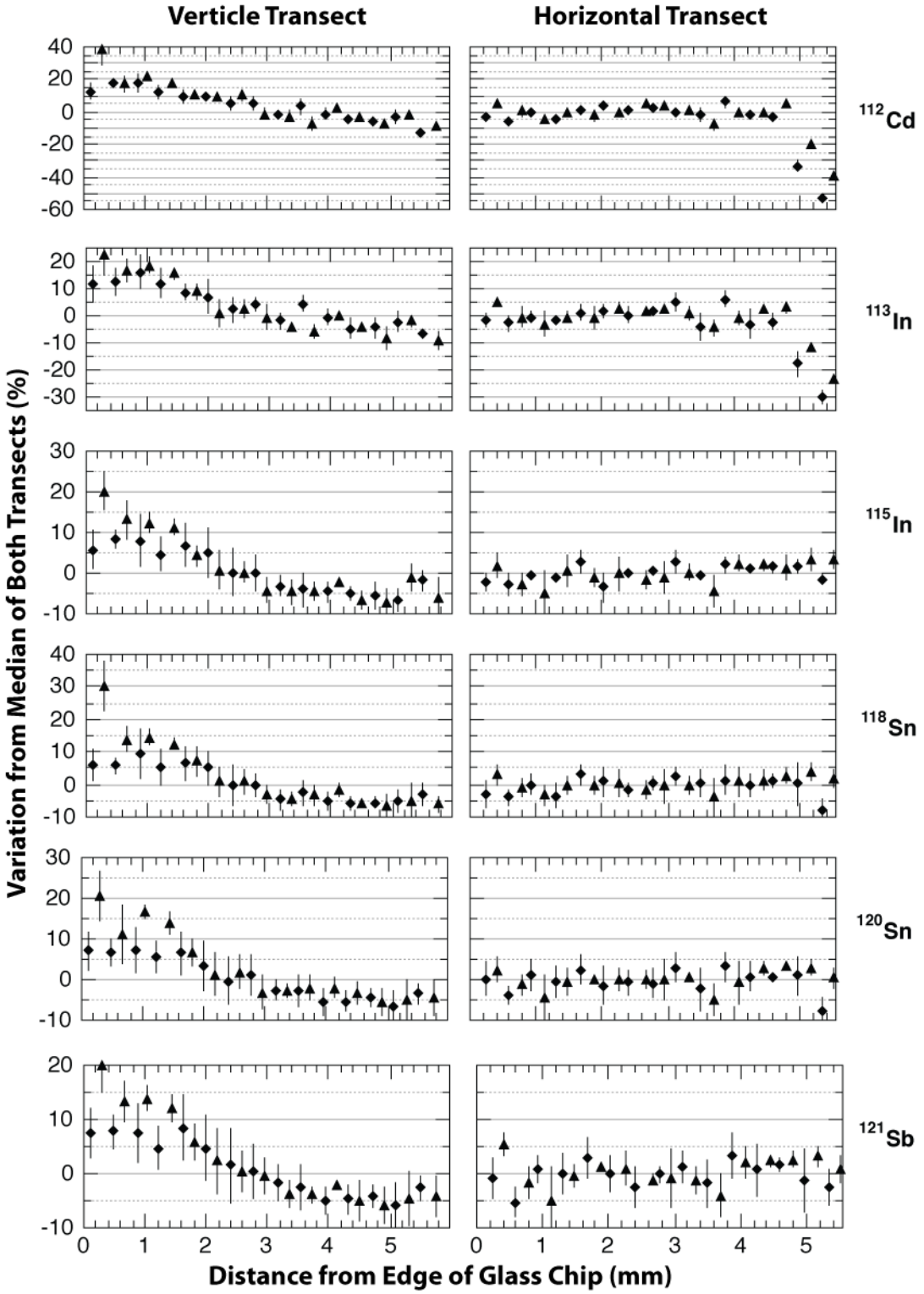
Verticle Transect
Horizontal Transect
Variation from Median of Both Transects (%)
Distance from Edge of Glass Chip (mm)
112Cd
113In
115In
118Sn
120Sn
121Sb

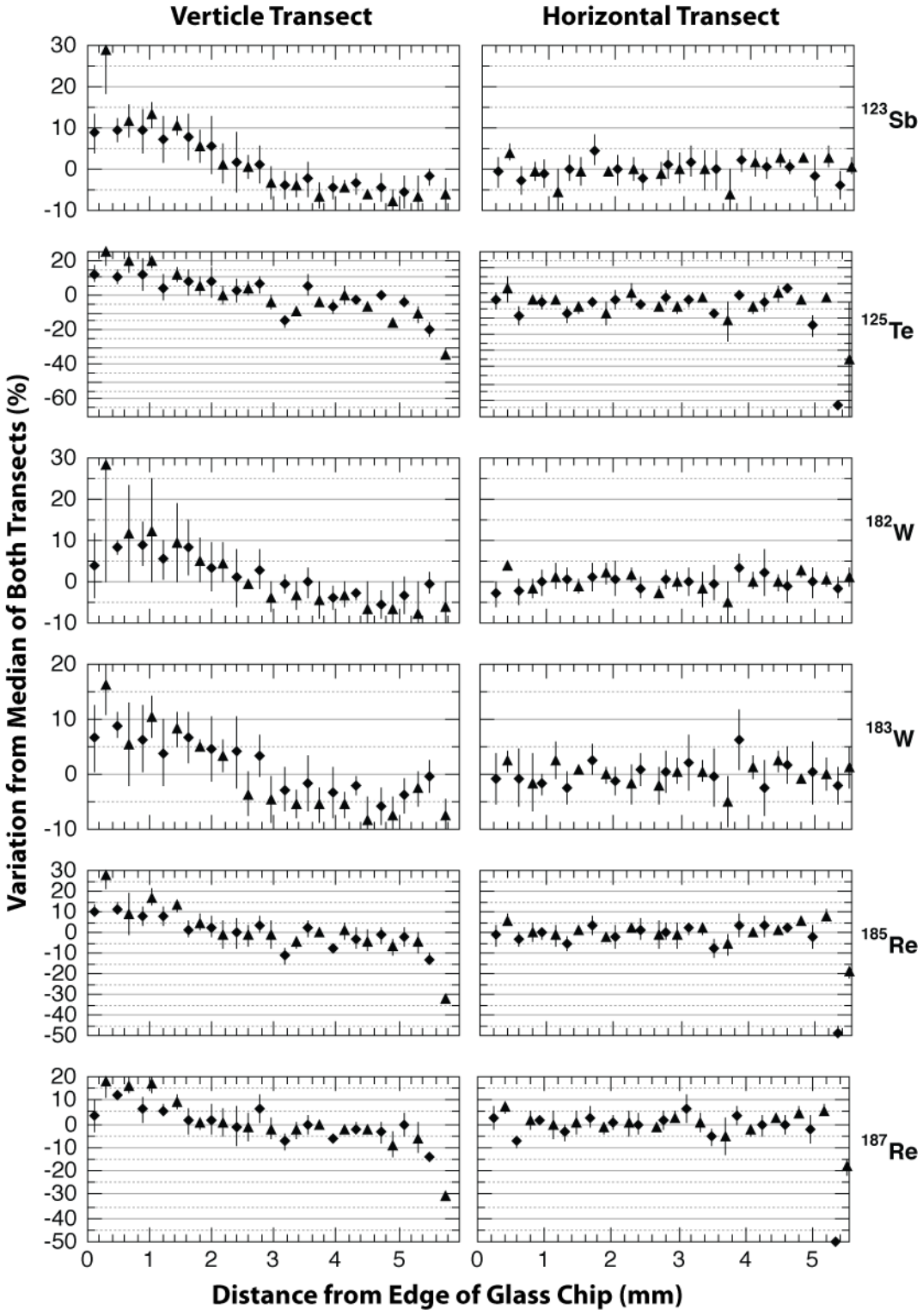
Verticle Transect
Horizontal Transect
123Sb
125Te
182W
183W
185Re
187Re
Variation from Median of Both Transects (%)
Distance from Edge of Glass Chip (mm)

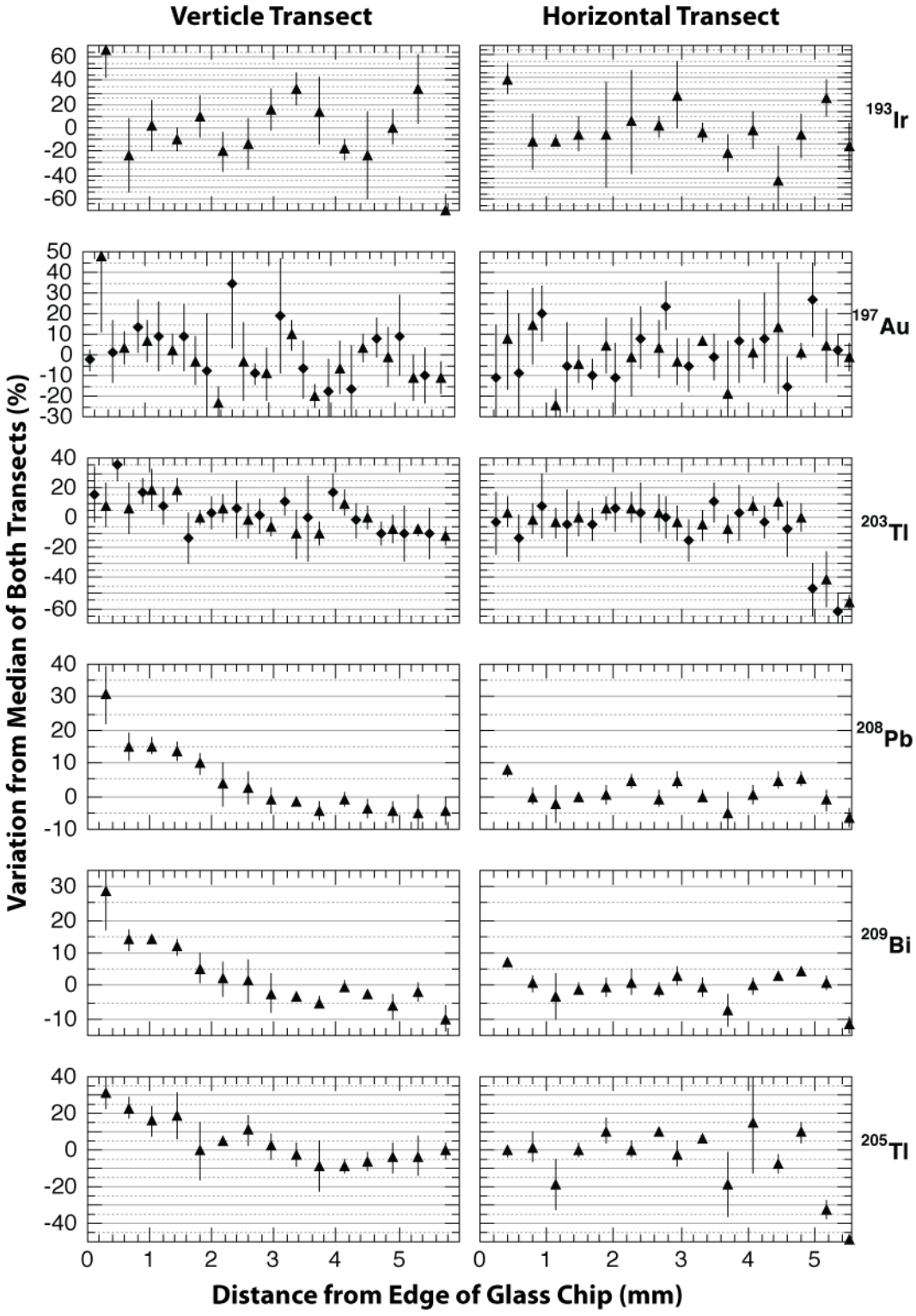
Verticle Transect
Horizontal Transect
193Ir
197Au
203Tl
208Pb
209Bi
205Tl
Variation from Median of Both Transects (%)
Distance from Edge of Glass Chip (mm)

D. Secondary standard accuracy of GSE-1G and NIST-610 calibrations

Tables D1 and D2 present additional results for accuracy of both GSE-1G calibrations and NIST-610 calibrations using 80 um spots on a number of synthetic and natural glass standards (accuracies are calculated from the average of 3 analyses compared to preferred values from the GeoReM database). Unlike the standards analyzed in this paper, these tests include a range of glass compositions from basaltic (BCR-2G, BHVO-2G) to intermediate (T1-G, StHS-680-G) and rhyolitic (ANTHO-G) as well as the subordinate synthetic standards (GSD-1G and NIST-612).

Interpretation of the natural glasses is complicated due to overriding uncertainties caused by counting statistics. Overall, GSE-1G calibrations had similar accuracies for both mafic and felsic standards. GSE-1G calibration also appears to produce equivalent and perhaps superior accuracy compared to NIST-610 for all compositions, as discussed in this paper. For some major elements (Fe, Ti) it is important to note that despite high concentrations, there is anomalously reduced accuracy for the more felsic compositions. This pattern is not readily evident in most trace elements but could have important implications when determining their concentrations in mineral phases (e.g., quartz, plagioclase) where the matrix might more closely approximate a felsic composition.

Table D1. Additional accuracy results with GSE-1G calibration.

	BHVO-2G			BCR-2G			GSD-1G			NIST-612		
	GeoREM	Median LA	Accuracy	GeoREM	Median LA	Accuracy	GeoREM	Median LA	Accuracy	GeoREM	Median LA	Accuracy
7Li	4.4	5.5	25.3	9	10.4	15.1	43	45.1	4.8	42	38.1	-9.4
11B	0	4.0		6	4.7	-21.5	50	51.6	3.2	35	27.6	-21.2
43Ca	81475	81475	0	50457	50457	0	51458	51458	0	85049	85049	0
45Sc	33	30.7	-7.1	33	34.2	3.6	52	54.4	4.7	41	44.0	7.4
47Ti	16300	16340	0.2	14100	13810	-2.1	7434	7876	6.0	44	40.9	-7.0
51V	308	368	19.4	425	453	6.6	44	44.5	1.1	39	41.0	5.1
52Cr	293	329	12.2	17	20.6	20.9	42	48.5	15.6	36	43.1	19.8
57Fe	87835	94695	8	96386	101690	6	103381	101300	-2.0	51	46.2	-9.4
59Co	44	50.2	14.0	38	39.5	3.9	40	39.5	-1.3	35	34.0	-2.8
65Cu	127	149	17.7	21	20.2	-3.9	42	42.2	0.4	37	37.2	0.6
66Zn	102	133	30.5	125	164	31.1	54	53.4	-1.0	38	36.5	-3.8
75As	0	1.0		0	1.2		27	26.7	-1.2	37	24.7	-33.2
76Se	0	4.1		0	3.5		2	3.4	72.2	0	2.3	
85Rb	9.2	10.0	8.5	47	48.3	2.8	37.3	36.5	-2.3	31.4	29.6	-5.7
88Sr	396	390	-1.5	342	327	-4.4	69.4	69.1	-0.4	78.4	76.2	-2.9
89Y	26	20.5	-21.1	35	29.0	-17.0	42	40.0	-4.8	38	38.0	0.0
90Zr	170	143	-15.8	184	164	-10.8	42	42.1	0.3	38	38.0	-0.1
98Mo	3.8	4.7	23.5	270	284	5.2	39	38.7	-0.8	38	37.4	-1.5
107Ag	0	0.55		0.5	0.62	24.7	23	23.3	1.1	22	21.0	-4.3
112Cd	0.1	0.11	8.1	0.2	0.22	8.1	18	20.0	11.3	28.3	20.1	-28.9
115In	0.1	0.12	16.0	0.11	0.10	-11.8	38	35.7	-5.9	43	32.3	-24.8
118Sn	2.6	1.7	-35.5	2.6	1.9	-28.8	29	27.5	-5.0	38	28.8	-24.3
121Sb	0.3	0.18	-41.6	0.35	0.44	26.2	43	43.1	0.3	38	38.4	1.1
125Te	0.3			0.35			43	45.4	5.6	38	48.3	27.1
137Ba	131	129	-1.8	683	655	-4.1	67	68.6	2.4	39.7	35.8	-9.9
140Ce	37.6	38.3	1.8	53.3	52.5	-1.6	41.4	40.2	-2.9	38.7	37.6	-2.8
182W	0.23	0.24	5.9	0.5	0.58	15.4	43	40.2	-6.5	40	38.8	-3.0
185Re	0.00047			0.0062			0	7.8		6.6	9.8	48.2
193Ir	0.00047			0.0062	0.11	1604	0	35.1		6.6		
197Au	0	0.35		0	0.02		4	3.3	-16.5	5.1	3.2	-37.6
208Pb	1.7	2.1	21.5	11	11.5	4.4	50	47.4	-5.1	38.57	36.4	-5.6
209Bi	0.01	0.018	81.4	0.05	0.05	0.7	35	31.1	-11.2	30	28.8	-3.9
232Th	1.22	1.12	-8.0	5.9	5.4	-8.5	41	38.0	-7.3	37.79	34.6	-8.4

Table D1. (continued)

	T1-G			StHS-680-G			ANTHO-G		
	GeoREM	Median LA	Accuracy	GeoREM	Median LA	Accuracy	GeoREM	Median LA	Accuracy
7Li	19.9	25.1	26.3	20.7	26.0	25.6	28.6	34.0	18.8
11B	4.1	2.7	-33.3	11.8	12.5	6.1	5.7	4.8	-15.3
43Ca	50743	50743	0	37736	37736	0	12150	12150	0
45Sc	26.9	26.4	-1.7	11.5	12.2	6.3	7	9.1	30.6
47Ti	4526	4745	4.8	4214	4529	7.5	1529	1774	16.0
51V	190	234	23.0	90.3	102	13.2	3.91	7.0	78.8
52Cr	20.9	24.8	18.8	16.9	18.9	11.8	6.1	9.2	50.8
57Fe	50058	56215	12	33968	38869	14	25418	30658	21
59Co	18.9	21.7	15.0	13.2	15.8	19.8	2.13	3.4	57.8
65Cu	18.8	25.1	33.5	41.5	48.3	16.3	18.6	22.0	18.3
66Zn	74	83.6	12.9	67	77.5	15.7	141	124	-12.4
75As	0.96	0.80	-16.2	2.73	2.7	-2.6	1.4	1.2	-17.3
76Se	0.05	1.5	2839.8	0.04	2.9	7194.3	0.1	1.1	985.7
85Rb	79.7	96.6	21.2	30.7	33.3	8.3	65.3	72.0	10.2
88Sr	284	279	-1.6	482	464	-3.8	94.1	84.0	-10.7
89Y	23.9	20.2	-15.4	11.4	9.7	-15.0	94.5	88.2	-6.7
90Zr	144	129	-10.7	118	109	-8.0	512	521	1.7
98Mo	4.2	7.9	87.7	2	1.9	-3.7	4.8	10.0	108.4
107Ag	0.1	0.08	-15.2	0.02			0.3	0.15	-49.2
112Cd	0.2	0.10	-50.0	0.1	0.19	86.2	0.5	0.20	-59.3
115In	0.3	0.26	-14.1	0.5	0.41	-18.5	0.17	0.15	-10.1
118Sn	2	1.7	-16.4	1.1	1.0	-7.6	5.41	2.6	-52.6
121Sb	0.25	0.35	39.9	0.2	0.32	62.3	0.32	0.31	-1.7
125Te	0.25	0.43	72.2	0.2	0.38	89.5	0.32	1.1	245.9
137Ba	388	383	-1.3	298	293	-1.6	547	498	-9.0
140Ce	127	128	0.8	26.1	26.0	-0.3	121	120	-0.5
182W	0.69	0.73	6.0	0.47	0.38	-20.0	9.3	8.8	-5.1
185Re	0.0018			0.0009	0.04	4877.0	0.0005		
193Ir	0.0018	0.12	6836	0.0009	0.14	15421	0.0005	0.09	18455
197Au	0.1	0.02	-80.0	0.048	0.03	-39.8	0.03	0.05	53.8
208Pb	11.6	10.7	-8.1	10.3	12.6	22.4	5.67	4.5	-20.6
209Bi	0.1	0.05	-50.4	0.11	0.09	-16.2	0.05	0.04	-22.9
232Th	31.3	25.6	-18.2	2.28	2.0	-12.9	7.4	6.3	-15.2

Table D2. Additional accuracy results with NIST-610 calibration.

	BHVO-2G			BCR-2G			GSD-1G			NIST-612		
	GeoREM	Median LA	Accuracy	GeoREM	Median LA	Accuracy	GeoREM	Median LA	Accuracy	GeoREM	Median LA	Accuracy
7Li	4.4	4.3	-3.2	9	8.5	-5.8	43	43.0	0.0	42	41.1	-2.2
11B	0	5.0		6	5.9	-1.2	50	64.9	29.8	35	34.7	-0.8
43Ca	81475	81475	0	50457	50457	0	51458	51458	0	85049	85049	0
45Sc	33	27.1	-18.0	33	30.2	-8.5	52	48.1	-7.6	41	38.9	-5.2
47Ti	16300	15505	-4.9	14100	13105	-7.1	7434	7474	0.5	44	38.8	-11.8
51V	308	324	5.2	425	399	-6.1	44	39.2	-11.0	39	36.1	-7.4
52Cr	293	287	-2.2	17	17.9	5.5	42	42.3	0.8	36	37.6	4.5
57Fe	87835	33115	-62	96386	38926	-60	103381	96669	-6.5	51	50.3	-1.3
59Co	44	36.7	-16.6	38	30.3	-20.3	40	37.6	-6.0	35	33.9	-3.2
65Cu	127	140	10.6	21	19.0	-9.7	42	39.6	-5.7	37	35.0	-5.5
66Zn	102	136	33.4	125	167	34.0	54	54.6	1.1	38	37.3	-1.7
75As	0	1.3		0	1.6		27	35.0	29.6	37	32.4	-12.3
76Se	0	13.6		0	12.3		2	18.6	831	0	13.1	
85Rb	9.2	10.2	11.2	47	49.5	5.3	37.3	37.4	0.1	31.4	30.3	-3.4
88Sr	396	384	-2.9	342	322	-5.8	69.4	68.1	-1.8	78.4	75.1	-4.2
89Y	26	26.6	2.2	35	36.1	3.0	42	36.8	-12.3	38	33.0	-13.1
90Zr	170	129	-24.4	184	147	-19.9	42	37.8	-9.9	38	34.1	-10.3
98Mo	3.8	4.3	13.6	270	261	-3.2	39	35.6	-8.7	38	34.4	-9.3
107Ag	0	0.5		0.5	0.58	16.9	23	21.8	-5.2	22	19.7	-10.3
112Cd	0.1	0.14	38.6	0.2	0.28	38.6	18	25.7	42.7	28.3	25.8	-8.8
115In	0.1	0.13	26.4	0.11	0.11	-3.9	38	38.9	2.5	43	35.2	-18.1
118Sn	2.6	1.9	-27.7	2.6	2.1	-20.2	29	30.9	6.5	38	32.2	-15.2
121Sb	0.3	0.1	-67.9	0.35	0.26	-25.6	43	33.8	-21.4	38	31.4	-17.4
125Te	0.3			0.35			43	34.9	-18.8	38	37.2	-2.2
137Ba	131	124	-5.1	683	633	-7.4	67	66.3	-1.1	39.7	34.5	-13.0
140Ce	37.6	35.0	-6.8	53.3	48.0	-9.9	41.4	36.8	-11.2	38.7	34.4	-11.0
182W	0.23	0.23	0.5	0.5	0.55	9.5	43	38.1	-11.3	40	36.8	-8.0
185Re	0.00047			0.0062			0	4.5		6.6	5.5	-16.9
193Ir	0.00047			0.0062	33.41	538768	0	11113.2		6.6		
197Au	0	0.4		0	0.02		4	3.9	-3.0	5.1	4.0	-21.9
208Pb	1.7	2.0	17.4	11	11.1	0.9	50	45.8	-8.4	38.57	35.2	-8.9
209Bi	0.01	0.018	80.8	0.05	0.05	0.3	35	31.0	-11.6	30	28.7	-4.3
232Th	1.22	1.10	-9.9	5.9	5.3	-10.5	41	37.2	-9.3	37.79	33.9	-10.3

Table D2. (continued)

	T1-G			StHS-680-G			ANTHO-G		
	GeoREM	Median LA	Accuracy	GeoREM	Median LA	Accuracy	GeoREM	Median LA	Accuracy
7Li	19.9	35.7	79.3	20.7	23.3	12.5	28.6	42.0	47.0
11B	4.1	3.4	-16.1	11.8	15.8	33.5	5.7	6.1	6.6
43Ca	50743	50743	0	37736	37736	0	12150	12150	0
45Sc	26.9	23.4	-13.2	11.5	10.8	-6.1	7	8.1	15.3
47Ti	4526	4503	-0.5	4214	4298	2.0	1529	1683	10.1
51V	190	206	8.4	90.3	90	-0.3	3.91	6.2	57.5
52Cr	20.9	21.7	3.6	16.9	16.5	-2.5	6.1	8.0	31.5
57Fe	50058			33968	20553	-39	25418	219494	764
59Co	18.9	30.1	59.5	13.2	13.4	1.8	2.13	4.0	86.5
65Cu	18.8	23.6	25.4	41.5	45.4	9.3	18.6	20.7	11.2
66Zn	74	85.4	15.4	67	79.2	18.3	141	126	-10.5
75As	0.96	1.06	10.0	2.73	3.5	27.8	1.4	1.5	8.5
76Se	0.05	16.6	33010	0.04	12.3	30528	0.1	8.3	8210
85Rb	79.7	99.0	24.2	30.7	34.1	11.0	65.3	73.7	12.9
88Sr	284	276	-3.0	482	457	-5.1	94.1	82.8	-12.0
89Y	23.9	14.1	-40.9	11.4	10.2	-10.9	94.5	67.0	-29.1
90Zr	144	115	-19.9	118	97	-17.4	512	468	-8.7
98Mo	4.2	7.3	72.7	2	1.8	-11.4	4.8	9.2	91.7
107Ag	0.1	0.08	-20.5	0.02			0.3	0.14	-52.4
112Cd	0.2	0.13	-35.9	0.1	0.24	138.6	0.5	0.26	-47.9
115In	0.3	0.28	-6.4	0.5	0.44	-11.2	0.17	0.17	-2.1
118Sn	2	1.9	-6.3	1.1	1.1	3.6	5.41	2.9	-46.8
121Sb	0.25	0.45	78.2	0.2	0.21	6.5	0.32	0.31	-1.8
125Te	0.25	0.33	32.5	0.2	0.29	45.8	0.32	0.85	166.2
137Ba	388	370	-4.6	298	283	-5.0	547	481	-12.1
140Ce	127	117	-7.7	26.1	23.8	-8.7	121	110	-8.9
182W	0.69	0.69	0.6	0.47	0.36	-24.2	9.3	8.4	-10.0
185Re	0.0018			0.0009	0.03	2940.6	0.0005		
193Ir	0.0018	39.47	2192863	0.0009	44.17	4907200	0.0005	29.33	5866600
197Au	0.1	0.03	-73.3	0.048	0.03	-27.7	0.03	0.06	99.4
208Pb	11.6	10.3	-11.3	10.3	12.2	18.2	5.67	4.3	-23.3
209Bi	0.1	0.05	-50.5	0.11	0.09	-16.4	0.05	0.04	-23.2
232Th	31.3	25.1	-19.9	2.28	1.9	-14.7	7.4	6.1	-17.0

E. EMPA calibration settings and detection limits

Table E1. Settings and long-term detection limits for EMPA analysis.

	Al	Ca	Cl	Cr	F	Fe	K	Mg	Mn	Na	Ni	P	S	Si	Ti
Glass															
Spectrometer	1	5	3, 5	4	2	4	5	2	4	2	4	3	3, 5	1	5
Crystal	TAP	PET	LPET, PET	LIF	LTAP	LIF	PET	LTAP	LIF	LTAP	LIF	LPET	LPET, PET	TAP	PET
Peak Time (s)	20-60	30	60	40	60	30	30	60	30	20	60	60	60	20	20
Background Time (s)	10-30	15	30	20	30	15	15	30	15	10	30	30	30	10	10
Calibration Material	LABR	BASL	TUGT	CROM	FLAP	FO83 BASL	KSPR	BASL	PYMN	KANO KAUG	NiSi	FLAP	CHAL	BASL	BASL
Median Det. Lim. (ppm)	185	198	69	412	513	542	228	107	516	239	483	101	71	365	282
2 sd	11	346	143	467	365	279	38	518	64	118	196	9	23	13	469
Olivine															
Spectrometer	1	3		3		4	5	2	4	2	4			1	3
Crystal	TAP	LPET		LPET		LIF	PET	LTAP	LIF	LTAP	LIF			TAP	LPET
Peak Time (s)	10	30		30		30	10-60	20	20	20	30			10	30
Background Time (s)	5	15		15		15	5-30	10	10	10	15			5	15
Calibration Material	LABR	LABR		CROM		FO83	KSPR	FO83	PYMN	KANO	NiSi			FO83	BASL
Median Det. Lim. (ppm)	237	115		258		548	448	359	549	225	681			343	139
2 sd	17	4		5		48	200	21	113	26	78			15	4

F. Uncorrected melt inclusion compositions

Table F1. Measured (uncorrected) melt inclusion compositions.

Sample	01-01-1	01-01-2	01-05	01-13	02-10	02-13-1	02-13-2
Major Elements (wt. %)							
SiO_2	51.58	51.58	52.66	51.73	51.73	50.27	51.09
TiO_2	2.68	2.42	3.15	2.69	2.88	2.63	2.59
Al_2O_3	13.98	13.48	14.28	13.32	13.58	13.26	13.27
Cr_2O_3	0.05	0.10	0.07	0.05	0.05	0.09	0.08
FeO*	10.77	10.04	7.97	9.18	9.40	10.95	10.51
MnO	0.14	0.19	0.14	0.15	0.15	0.16	0.14
MgO	6.60	7.83	8.87	8.74	7.88	7.35	7.35
CaO	12.85	12.32	11.02	11.90	12.57	13.60	13.30
Na_2O	2.47	2.42	2.46	2.49	2.30	2.05	2.09
K_2O	0.42	0.39	0.67	0.40	0.55	0.33	0.38
P_2O_5	0.26	0.26	0.34	0.40	0.30	0.53	0.37
S	0.15	0.15	0.03	0.13	0.12	0.14	0.07
Cl	0.02	0.02	0.02	0.01	0.03	0.01	0.02
F	0.02	0.02	0.04	0.02	0.03	0.03	0.02
NiO	0.01	0.03	0.05	0.01	0.03	0.01	0.02
Total	102.00	101.23	101.77	101.23	101.60	101.42	101.30
Fo (host)	87.2	87.2	88.0	88.1	87.3	86.8	86.9
Trace Elements (ppm)							
B		1.7	2.4	2.4	3.1	5.2	10.4
Sc		34.9	27.8	30.4	31.2	34.7	34.6
V		372	305	363	364	410	409
Cr							
Co							
Cu		86	141	57	101	82	115
Zn		128	98	126	116	121	115
Rb		8.2	12.7	7.8	12.3	5.4	9.4
Sr		361	420	362	425	288	920
Y		19.3	24.0	18.3	20.0	21.5	20.3
Zr		134	181	128	150	112	123
Mo		1.01	1.38	0.99	1.12	0.76	1.22
Ag		0.08	0.08		0.05	0.05	0.10
Cd		0.24	0.19	0.06	0.37	0.13	
In		0.12	0.07	0.08	0.04	0.10	0.08
Sn		1.4	1.7	1.6	1.4	1.1	1.3
Sb		0.08	0.02	0.06			0.25
Ba		108	159	109	156	80	172
Ce		32.7	43.6	33.7	43.8	25.6	29.3
W		0.17	0.24	0.23	0.28		0.15
Pb		1.10	1.47	1.20	1.35	0.79	1.67
Tl							
Bi				0.02			
U		0.32	0.46	0.30	0.52	0.25	0.35

Table F1. (continued)

Sample	03-01	03-03	03-04	03-09-1	03-09-2	03-06
Major Elements (wt. %)						
SiO_2	50.75	50.93	50.69	50.40	50.08	50.58
TiO_2	2.63	2.83	2.86	2.58	2.69	2.85
Al_2O_3	13.20	13.42	13.83	13.29	12.99	13.76
Cr_2O_3	0.12	0.06	0.09	0.09	0.08	0.10
FeO*	10.31	9.55	9.45	9.94	10.63	9.53
MnO	0.19	0.16	0.12	0.14	0.15	0.15
MgO	8.09	8.09	7.48	8.68	8.29	6.40
CaO	11.82	13.00	13.21	12.64	12.95	13.83
Na_2O	2.40	2.08	1.98	2.09	1.95	2.04
K_2O	0.50	0.46	0.55	0.39	0.41	0.38
P_2O_5	0.32	0.29	0.34	0.35	0.29	0.32
S	0.16	0.14	0.13	0.03	0.17	0.16
Cl	0.02	0.02	0.02	0.02	0.02	0.02
F	0.02	0.02	0.02	0.03	0.03	0.03
NiO	0.02	0.01	0.03	0.01	0.03	0.01
Total	100.55	101.08	100.80	100.67	100.76	100.14
Fo (host)	87.0	87.5	87.9	87.1	87.0	88.5
Trace Elements (ppm)						
B	3.0	3.1	3.0	2.3	3.2	4.1
Sc	31.7	30.0	32.1	31.4	33.3	34.1
V	373	421	414	384	408	424
Cr						
Co						
Cu	106	79	67	135	117	103
Zn	136	132	173	119	133	189
Rb	9.8	12.1	12.1	7.6	8.7	8.4
Sr	418	396	487	300	387	380
Y	18.8	18.4	20.8	18.1	20.4	22.2
Zr	148	122	168	111	139	146
Mo	1.23	1.11	1.75	0.93	1.07	1.63
Ag		0.04	0.20	0.07	0.04	
Cd	0.20	0.28	0.60		0.11	0.25
In	0.10	0.08	0.08	0.08	0.09	0.11
Sn	1.7	1.6	2.4	1.3	1.3	1.9
Sb		0.09	0.08			
Ba	132	154	162	108	122	111
Ce	39.6	43.3	55.0	30.4	40.1	39.5
W	0.24	0.25	0.32			0.20
Pb	1.27	1.56	1.91	0.97	1.02	1.24
Tl						
Bi			0.03	0.02		
U	0.45	0.48	0.61	0.31	0.40	0.34

Table F1. (continued)

Sample	03-25	03-26	04-06	04-09	04-10-1	04-10-2
Major Elements (wt. %)						
SiO_2	50.52	50.95	51.67	50.55	50.72	51.20
TiO_2	2.46	2.69	2.66	2.78	3.01	2.86
Al_2O_3	12.78	13.70	13.20	13.28	15.18	14.88
Cr_2O_3	0.08	0.08	0.06	0.07	0.12	0.07
FeO*	11.41	11.94	9.57	10.34	9.59	9.14
MnO	0.16	0.17	0.18	0.16	0.10	0.13
MgO	8.62	6.78	8.74	8.38	5.00	5.10
CaO	11.96	13.19	12.20	12.83	14.62	14.07
Na_2O	2.01	2.37	2.32	2.04	2.10	2.42
K_2O	0.47	0.44	0.38	0.51	0.50	0.47
P_2O_5	0.25	0.27	0.24	0.30	0.33	0.29
S	0.11	0.16	0.12	0.11	0.16	0.14
Cl	0.02	0.02	0.02	0.02	0.02	0.01
F	0.02	0.02	0.02	0.02	0.04	0.03
NiO	0.01	0.01	0.03	0.04	0.02	-0.01
Total	100.88	102.80	101.40	101.43	101.53	100.81
Fo (host)	85.8	85.6	87.1	87.2	87.8	87.7
Trace Elements (ppm)						
B	2.3		2.5	4.3		
Sc	30.3		31.0	31.8		
V	373		339	438		
Cr						
Co						
Cu	167		112	136		
Zn	145		121	150		
Rb	9.9		6.8	11.5		
Sr	352		340	395		
Y	17.8		20.2	17.8		
Zr	114		124	130		
Mo	0.98		0.85	1.30		
Ag	0.05		0.05	0.05		
Cd	0.12		0.23	0.17		
In	0.10		0.08	0.11		
Sn	1.5		1.4	1.7		
Sb			0.05			
Ba	128		100	151		
Ce	35.3		29.5	45.9		
W	0.22		0.18			
Pb	1.11		0.98	1.33		
Tl						
Bi			0.01			
U	0.37		0.26	0.41		

Table F1. (continued)

Sample	04-17	04-22	04-25	04-23	01-06b-1	01-06b-2
Major Elements (wt. %)						
SiO_2	51.69	50.55	51.79	51.92	49.87	51.05
TiO_2	2.60	2.89	3.05	2.63	2.76	2.79
Al_2O_3	13.66	13.38	14.35	13.31	13.57	13.89
Cr_2O_3	0.09	0.12	0.03	0.10	0.05	0.09
FeO*	10.14	11.47	10.68	9.55	8.74	9.09
MnO	0.16	0.18	0.15	0.11	0.13	0.16
MgO	5.93	6.76	5.71	8.88	8.41	8.15
CaO	13.68	13.06	11.96	12.13	12.42	12.82
Na_2O	2.11	2.05	2.24	2.30	2.26	1.56
K_2O	0.43	0.50	0.58	0.40	0.94	0.68
P_2O_5	0.49	0.35	0.31	0.26	1.03	0.49
S	0.14	0.15	0.02	0.11	0.13	0.13
Cl	0.02	0.02	0.02	0.01	0.04	0.03
F	0.02	0.02	0.03	0.03	0.06	0.04
NiO	0.01	0.01	0.01	0.02	0.03	0.01
Total	101.18	101.48	100.93	101.77	100.44	100.98
Fo (host)	88.3	87.2	85.8	87.5	87.9	87.6
Trace Elements (ppm)						
B			2.1	2.6	3.1	2.7
Sc			31.3	30.2	34.9	33.8
V			374	354	317	320
Cr					473	472
Co					40.7	42.0
Cu			118	108	26	27
Zn			128	125	93	95
Rb			11.6	7.5	15.7	11.0
Sr			433	336	709.2	595.5
Y			23.2	18.8	22.4	23.7
Zr			162	118	200	197
Mo			1.03	0.82	1.68	1.42
Ag			0.09	0.05		
Cd			0.08	0.28	0.27	0.52
In			0.10	0.10		
Sn			1.7	1.6	1.9	2.0
Sb			0.06	0.06		
Ba			168	101	220	163
Ce			43.4	30.9	52.6	44.5
W			0.22	0.24	0.36	0.29
Pb			1.26	1.12	2.86	1.46
Tl					0.06	0.02
Bi						
U			0.44	0.29		

Table F1. (continued)

Sample	01-06b-3	02-01b-1	02-01b-2	02-05b	02-15b	02-13b
Major Elements (wt. %)						
SiO_2	51.44	52.58	52.19	48.74	50.74	49.67
TiO_2	3.17	2.55	2.60	2.42	2.65	2.79
Al_2O_3	13.96	13.60	13.72	12.99	13.53	13.28
Cr_2O_3	0.06	0.05	0.09	0.06	0.07	0.11
FeO*	8.03	9.81	9.66	10.04	10.01	9.79
MnO	0.16	0.16	0.14	0.13	0.18	0.17
MgO	7.26	8.64	8.26	8.17	7.82	8.47
CaO	12.15	12.14	11.79	11.79	12.53	13.04
Na_2O	2.65	0.67	0.75	2.13	2.17	2.11
K_2O	0.71	0.40	0.43	0.41	0.38	0.38
P_2O_5	0.47	0.26	0.29	0.29	0.28	0.37
S	0.12	0.13	0.15	0.14	0.14	0.07
Cl	0.03	0.01	0.01	0.02	0.01	0.01
F	0.04	0.03	0.01	0.03	0.03	0.03
NiO	0.04	0.04	0.04	0.01	0.04	0.03
Total	100.30	101.08	100.13	97.38	100.58	100.32
Fo (host)	88.1	87.4	87.5	86.4	86.3	87.3
Trace Elements (ppm)						
B	3.8	2.1	1.6	1.5		2.4
Sc	34.8	32.7	31.0	30.0	38.3	34.8
V	278	351	349	327	286	335
Cr	453	600	577	485	453	408
Co	32.1	54.5	49.8	47.8	37.7	44.4
Cu	28	152	140	154	100	94
Zn	95	120	117	123	95	91
Rb	10.8	6.5	8.0	7.5	5.7	4.7
Sr	749.4	318.9	312.0	346.8	345.2	496.4
Y	25.4	19.9	19.1	18.7	24.6	21.6
Zr	288	117	119	129	153	140
Mo	1.45	0.67	0.90	1.35	0.61	0.62
Ag						
Cd	0.24	0.30	0.16	0.17	0.00	0.49
In						
Sn	2.7	1.5	1.3	1.3	1.0	1.6
Sb						
Ba	210	95	114	112	92	297
Ce	60.1	29.4	29.5	33.1	26.9	32.7
W	0.50	0.11	0.19	0.13	0.09	
Pb	4.72	1.01	1.10	1.05	0.71	0.72
Tl	0.01		0.01	0.00		0.04
Bi						
U						

Table F1. (continued)

Sample	03-01b	03-04b	03-08b	03-24b	03-25b	04-24b
Major Elements (wt. %)						
SiO_2	50.79	49.96	51.88	49.48	50.28	50.31
TiO_2	2.75	2.98	2.60	2.62	2.52	2.64
Al_2O_3	13.40	13.48	13.49	12.37	12.95	13.03
Cr_2O_3	0.09	0.07	0.07	0.07	0.05	0.07
FeO*	9.85	9.45	10.97	11.43	10.70	10.06
MnO	0.15	0.17	0.16	0.17	0.16	0.18
MgO	8.29	7.45	7.61	8.78	8.65	8.59
CaO	11.87	12.81	12.71	12.25	12.07	12.10
Na_2O	2.39	1.82	0.66	2.01	2.10	2.15
K_2O	0.52	0.57	0.38	0.47	0.48	0.39
P_2O_5	0.31	0.31	0.25	0.35	0.23	0.27
S	0.15	0.13	0.15	0.16	0.10	0.13
Cl	0.02	0.02	0.02	0.02	0.01	0.01
F	0.03	0.05	0.03	0.01	0.04	0.04
NiO	0.04	-0.21	0.03	0.05	0.02	0.02
Total	100.65	99.05	101.01	100.21	100.36	99.99
Fo (host)	87.4	85.0	86.4	85.1	85.7	88.6
Trace Elements (ppm)						
B					4.2	1.6
Sc	31.4	35.2	40.2	37.5	31.3	34.7
V	373	381	412	432	418	334
Cr	778	564	500	649	573	623
Co	53.7	56.3	50.3	64.7	61.2	50.7
Cu	115	107	75	171	181	128
Zn	131	118	120	151	145	121
Rb	7.3	11.5	7.0	9.3	11.3	6.5
Sr	404.7	420.4	319.8	404.3	364.3	327.0
Y	20.1	21.6	21.7	18.2	18.4	22.4
Zr	147	148	131	146	117	143
Mo	0.46	2.02	2.09		2.92	0.75
Ag						
Cd			0.46	0.76	0.37	0.11
In						
Sn	2.4	1.9	2.0	1.5	2.4	1.7
Sb						
Ba	141	163	105	124	138	95
Ce	37.7	46.2	29.1	38.0	36.5	30.0
W	0.50	0.26	0.19	0.18		0.07
Pb	1.27	1.38	4.10	1.39	1.39	1.70
Tl					0.06	0.02
Bi						
U						